National Technical University of Athens
School of Mechanical Engineering
Fluids Section
Laboratory of Thermal Turbomachines
Parallel CFD & Optimization Unit

Data-Driven Eddy Viscosity Adaptation via the Continuous Adjoint Method. Applications in Aerodynamic Shape Optimization

Diploma Thesis

Angelos Antonios Petrocheilos

Supervisors:
Kyriakos C. Giannakoglou, Professor NTUA
Varvara G. Asouti, Adjunct Lecturer NTUA

Athens, 2026

Acknowledgments

First and foremost, I would like to express my gratitude to my supervisor, Professor Kyriakos C. Giannakoglou, for his invaluable guidance, the time he devoted to me, and his unwavering support throughout this thesis. I am especially grateful for the opportunity to be part of the PCOpt Unit, for his trust, and the scientific insight and passion for research that he shared with me.

I extend my sincere thanks to my second supervisor, Adjunct Lecturer Dr. Varvara Asouti, for her insightful ideas and continuous support during every stage of this work.

I would also like to thank Dr. Vangelis Papoutsis-Kiachagias for his assistance during the programming stages of this thesis, as well as all other members of the PCOpt Unit–Amin, Christos, Francesco, Javad, Giannis–and especially my office colleagues, Fabio Carfora and Victor Román, all of whom are exceptional individuals and scientists. Furthermore, I want to thank my friends Andreas Ioannides and Kalliopi Batsi, with whom I shared many memorable experiences and challenges through our academic path.

My appreciation also goes to the teaching and administrative staff of the Fluids Sector of the School of Mechanical Engineering at NTUA. The knowledge they imparted and the guidance they provided, sparked my passion for all branches of fluid dynamics, ranging from aerodynamics to energy systems and turbomachinery.

Lastly, I feel the need to thank my mother, Maria, for her endless patience throughout all stages of my life, as well as my loving girlfriend, Anastasia, for her precious support, the constant motivation she provided to help me reach my goals, and her presence in my life. *This thesis is dedicated to the memory of my father and grandfather.*

National Technical University of Athens
School of Mechanical Engineering
Fluids Section
Laboratory of Thermal Turbomachines
Parallel CFD & Optimization Unit

Data-Driven Eddy Viscosity Adaptation via the Continuous Adjoint Method. Applications in Aerodynamic Shape Optimization

Diploma Thesis

Angelos Antonios Petrocheilos

Supervisors:
Kyriakos C. Giannakoglou, Professor NTUA
Varvara G. Asouti, Adjunct Lecturer NTUA

Athens, 2026

Abstract

This diploma thesis investigates a data-driven turbulence modeling method, the Eddy Viscosity Adaptation (EVA), to achieve enhanced flowfield representation when solving the Reynolds-Averaged Navier-Stokes (RANS) equations compared to conventional turbulence models, such as the Spalart-Allmaras (SA), and subsequently be utilized for shape optimization (ShpO) purposes. Unlike traditional models, EVA does not require additional differential equations to calculate the eddy viscosity (ν_t) field. Instead, it directly updates the ν_t value within each cell in the computational mesh, by solving a field inversion problem, utilizing the continuous adjoint method.

First, the mathematical formulation of the EVA method for both low-Reynolds (wall-resolved) and high-Reynolds (wall-function) treatments is presented. The EVA-process aims at minimizing two distinct loss functions: the discrepancy between the RANS-computed velocity field, and that obtained from a High-Fidelity (Hi-Fi) solver–such as Direct Numerical Simulation (DNS) or Detached Eddy Simulation (DES)–as well as the difference in aerodynamic force coefficient predictions. EVA is subsequently implemented within the open-source computational fluid dynamics software `OpenFOAM`.

The efficacy of the method in reproducing Hi-Fi results, while solving the RANS equations, is demonstrated using different velocity-based loss functions for the flow over periodic hills, a standard benchmark for turbulence modeling. Results showcase up to a 95% reduction in the loss function value and the accurate capture of flow separation and reattachment points across five different geometry variations. Furthermore, the aerodynamic coefficient targeting approach, is evaluated on a NACA 0012 airfoil. While conventional turbulence models typically underpredict the angle of attack at which stall occurs, EVA manages to successfully align with the experimental drag and lift coefficients.

Finally, the EVA framework, utilizing a velocity-based loss function, is extended to 3D flows around various car models. In all test cases, EVA outperforms conventional models in predicting the velocity field (reducing the loss function by up to 46%), vortex topology, and drag force. Subsequently, Symbolic Regression (SR) is applied to reconstruct the corrected EVA-ν_t field as a closed-form algebraic expression dependent on local flow and geometrical variables. The resulting surrogate turbulence model is then deployed for ShpO to minimize the drag coefficent of the car, once again employing a continuous adjoint method. Four distinct ShpO frameworks are compared: classical RANS/SA; a frozen turbulence approach, where the ν_t field remains constant and equal to the EVA solution, even during geometry modifications; and two frameworks utilizing the surrogate SR model, with and without its differentiation within the adjoint equations. Results demonstrate that incorporating the fully differentiated SR model yields a superior reduction of the objective function compared to the baseline RANS/SA approach.

Keywords: Eddy Viscosity Adaptation, Field Inversion, Continuous Adjoint, Aerodynamic Shape Optimization.

Εθνικό Μετσόβιο Πολυτεχνείο
Σχολή Μηχανολόγων Μηχανικών
Τομέας Ρευστών
Εργαστήριο Θερμικών Στροβιλομηχανών
Μονάδα Παράλληλης Υπολογιστικής Ρευστοδυναμικής & Βελτιστοποίησης

Προσαρμογή Τυρβώδους Συνεκτικότητας βασισμένη σε Δεδομένα, μέσω της Συνεχούς Συζυγούς Μεθόδου. Εφαρμογές στην Αεροδυναμική Βελτιστοποίηση Μορφής

Διπλωματική Εργασία

Άγγελος Αντώνιος Πετρόχειλος

Επιβλέποντες:
Κυριάκος Χ. Γιαννάκογλου, Καθηγητής ΕΜΠ
Βαρβάρα Γ. Ασούτη, Εντεταλμένη Διδάσκουσα ΕΜΠ

Αθήνα, 2026

Περίληψη

Η παρούσα διπλωματική εργασία διερευνά μια μέθοδο μοντελοποίησης τύρβης βασισμένης σε δεδομένα, την Προσαρμογή Τυρβώδους Συνεκτικότητας (ΠΤΣ), με στόχο την ακριβέστερη αναπαράσταση των ροϊκών πεδίων κατά την επίλυση των εξισώσεων μέσης ροής των ρευστών (RANS), συγκριτικά με συμβατικά μοντέλα τύρβης (όπως το Spalart-Allmaras (SA)) καθώς και την αξιοποίηση της για εφαρμογές βελτιστοποίησης μορφής. Σε αντίθεση με τα παραδοσιακά μοντέλα τύρβης, η ΠΤΣ δεν απαιτεί την επίλυση επιπρόσθετων διαφορικών εξισώσεων για τον υπολογισμό του πεδίου τυρβώδους συνεκτικότητας ν_t. Αντίθετα ανανεώνει απευθείας την τιμή ν_t σε κάθε κελί του υπολογιστικού πλέγματος, λύνοντας ένα πρόβλημα αντιστροφής πεδίου (Field Inversion), με χρήση της συνεχούς συζυγούς μεθόδου.

Αρχικά, παρουσιάζεται η μαθηματική διατύπωση της μεθόδου ΠΤΣ για χρήση ή μη συναρτήσεων τοίχου, κοντά στα στερεά τοιχώματα. Η ΠΤΣ στοχεύει στην ελαχιστοποίηση δύο διαφορετικών συναρτήσεων κόστους: της απόκλισης μεταξύ του πεδίου ταχύτητας που υπολογίζεται κατά την επίλυση των RANS και εκείνου που προκύπτει από μία μέθοδο υψηλής πιστότητας, όπως η άμεση επίλυση των εξισώσεων Navier-Stokes (Direct Numerical Simulation - DNS) ή η προσομοίωση αποκολλημένων δινών (Detached Eddy Simulation - DES), καθώς και της διαφοράς στις προβλέψεις της τιμής αεροδυναμικών συντελεστών. Οι διάφορες παραλλαγές τις ΠΤΣ, προγραμματίζονται στο ανοιχτό λογισμικό υπολογιστικής ρευστοδυναμικής `OpenFOAM`.

Η αποτελεσματικότητα της μεθόδου στην αναπαραγωγή αποτελεσμάτων υψηλής πιστότητας από τις RANS, καταδεικνύεται με χρήση διαφορετικών συναρτήσεων κόστους, βασισμένων στην απόκλιση των πεδίων ταχυτήτων, για τη ροή πάνω από περιοδικούς λόφους, μια πρότυπη εφαρμογή για προβλήματα μοντελοποίησης τύρβης. Τα αποτελέσματα δείχνουν μείωση της τιμής της συνάρτησης κόστους έως και 95%, καθώς και ακριβέστερη πρόβλεψη των σημείων αποκόλλησης και επαναπροσκόλλησης της ροής για πέντε διαφορετικές γεωμετρικές παραλλαγές. Επιπλέον, η ΠΤΣ για στόχευση αεροδυναμικών συντελεστών, αξιολογείται για την αεροτομή NACA 0012. Ενώ τα συμβατικά μοντέλα τύρβης τείνουν να υποεκτιμούν τη γωνία προσβολής στην οποία εμφανίζεται απώλεια στήριξης, η μέθοδος επιτυγχάνει ικανοποιητική συμφωνία με τις πειραματικές τιμές των συντελεστών άνωσης και οπισθέλκουσας.

Τέλος, η ΠΤΣ με χρήση συνάρτησης κόστους βασισμένης στο πεδίο ταχύτητας, επεκτείνεται σε τρισδιάστατες ροές γύρω από διάφορα μοντέλα αυτοκινήτων. Σε όλες τις περιπτώσεις που εξετάζονται, υπερτερεί των συμβατικών μοντέλων ως προς την πρόβλεψη της μορφής του πεδίου ταχύτητας (επιτυγχάνοντας μείωση της συνάρτησης κόστους έως και 46%), της τοπολογία των στροβίλων και της δύναμης οπισθέλκουσας. Στη συνέχεια, εφαρμόζεται Συμβολική Παλινδρόμηση (ΣΠ, Symbolic Regretion) για την ανακατασκευή του διορθωμένου ΠΤΣ-ν_t πεδίου, υπό τη μορφή αλγεβρικής σχέσης που χρησιμοποιεί τοπικές μεταβλητές της ροής και της γεωμετρίας. Το υποκατάστατο μοντέλο τύρβης που προκύπτει, χρησιμοποιείται ακολούθως, σε εφαρμογή βελτιστοποίησης σχήματος, με στόχο την ελαχιστοποίηση του συντελεστή οπισθέλκουσας ενός αυτοκινήτου, αξιοποιώντας εκ νέου τη συνεχή συζυγή μέθοδο. Συγκρίνονται τέσσερες διαφορετικές μεθοδολογίες βελτιστοποίησης: η κλασική RANS/SA· μία προσέγγιση «παγωμένης τύρβης», όπου το πεδίο ν_t παραμένει σταθερό και ίσο με τη λύση της ΠΤΣ ακόμη και μετά την γεωμετρική μορφοποίηση· καθώς και δύο προσεγγίσεις που βασίζονται στο υποκατάστατο μοντέλο της ΣΠ, με και χωρίς τη συμπερίληψη των παραγώγων του στις συζυγείς εξισώσεις. Τα αποτελέσματα αναδεικνύουν ότι η χρήση του πλήρως διαφορισμένου μοντέλου ΣΠ, οδηγεί σε μεγαλύτερη μείωση της αντικειμενικής συνάρτησης συγκριτικά με τη συμβατική προσέγγιση RANS/SA.

Λέξεις-κλειδιά: Προσαρμογή Τυρβώδους Συνεκτικότητας, Αντιστροφή Πεδίου, Συνεχής Συζυγής Μέθοδος, Αεροδυναμική Βελτιστοποίηση Μορφής.

Abbreviations

ABC	Adjoint Boundary Conditions
AoA	Angle of Attack
CFD	Computational Fluid Dynamics
cfEV	closed form Eddy Viscosity
CPs	Control Points
CPU	Central Processing Unit
DES	Detached Eddy Simulation
DNS	Direct Numerical Solution
EVA	Eddy Viscocity Adaptation
FAE	Field Adjoint Equations
FI	Field Inversion
FI/ML	Field Inversion & Machine Learning framework
Hi-Fi	High Fidelity
HPC	High Performance Computing
LES	Larger Eddy Simulation
Low-Fi	Low Fidelity
ML	Machine Learning
MMA	Method of Moving Asympotes
NURBS	Non-Uniform Rational B-Splines
NTUA	National Technical University of Athens
PCOpt	Parallel CFD & Optimization Unit
RANS	Reynolds Averaged Navier Stokes
rEV	raw Eddy Viscosity
SAE	Society of Automotive Engineers
SA	Spalart-Allmaras
SD	Sensitivity Derivative

ShpO Shape Optimization
SR Symbolic Regression
woWwoM Without Wheels & Without Mirrors
w.r.t. with respect to

ΠΤΣ Προσαρμογή Τυρβώδους Συνεκτικότητας
ΣΠ Συμβολική Παλινδρόμιση
ΥΡΔ Υπολογιστική Ρευστοδυναμική

Contents

Chapter 1
Introduction

Over the past four decades, remarkable progress in computational power, numerical methods, and high-performance computing (HPC) has transformed computational fluid dynamics (CFD) into an essential tool for analyzing complex fluid-flow phenomena. Today, CFD is applied across a broad spectrum of engineering fields, including the automotive and aerospace industries, the energy sector (e.g., flows through turbomachines and around wind turbines), biomedical engineering (such as blood flow through arteries and heart valves), and environmental engineering (e.g., pollutant dispersion in atmosphere, weather modeling) to name a few.

A key milestone in the development of CFD was the implementation of Reynolds Averaged Navier–Stokes (RANS) flow solvers in the 1990s, which significantly improved simulation accuracy by better capturing the underlying flow physics compared to the widely used potential-flow methods of the era, presented in Fig. 1.1a. According to this approach, only the mean flow field is resolved, while the effects of turbulence, characterized by chaotic velocity fluctuations across a wide spectrum of spatial and temporal scales [1], enter the governing equations through the Reynolds stress tensor, which requires closure [2]. The most widespread assumption in RANS modeling is based on the Boussinesq hypothesis, which relates the Reynolds stresses to the mean strain rate through a linear relationship via the so-called turbulent eddy viscosity ν_t. This is not a property of the fluid but rather a function of the local flow state; its value must be determined through supplemental closure relationships [3]. Various modeling techniques have been developed for this purpose, ranging from algebraic formulations such as the Prandtl mixing-length model [4], which solves an algebraic equation for ν_t, to more complex approaches such as the Spalart–Allmaras (SA) model [5], which solves a transport equation, or even k–ϵ [6] and k–ω SST [7] models, both of solve two extra partial differential equations (PDEs).

Today, RANS equations remain the most widely used approach for the design, analysis, and optimization of fluid flows, primarily due to their low computational cost compared to High-Fidelity (Hi-Fi) methods (Fig. 1.1b), such as Large Eddy Simulation (LES) or Direct Numerical Simulation (DNS). However, as highlighted in the "CFD Vision 2030 Study", a large portion of the aerospace CFD community believes that RANS turbulence modeling, although still essential for current industrial applications, has reached a performance plateau [8]. Many of the turbulence closure models widely used today were developed several decades ago, and their underlying assumptions predate many of the advances in modern CFD and HPC. Consequently, further improvements in predictive accuracy using traditional modeling approaches alone have become increasingly challenging [9].

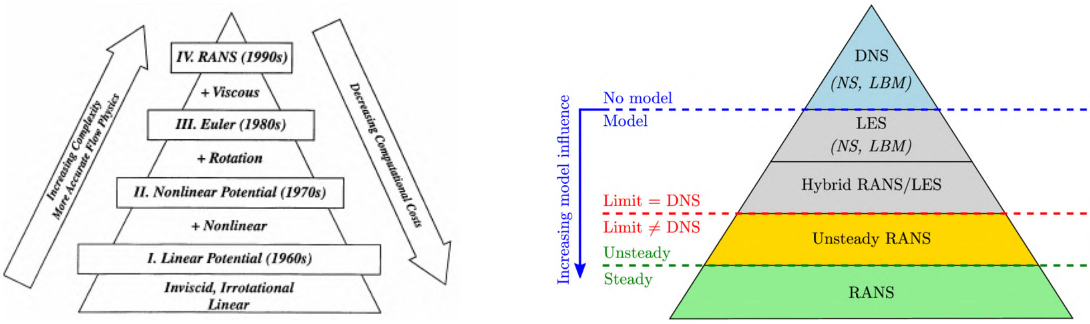

(a) *Historical evolution; from [10]* **(b)** *Present-day used models; from [11]*

Figure 1.1: *Hierarchy of fluid flow models in CFD*

The main objective of this thesis is to overcome the limitations of conventional RANS turbulence models, by developing data-driven approaches for turbulence closure. Sec. 1.1 provides a review of the relevant literature on Field Inversion (FI), as this is used for data-driven turbulence modeling. Sec. 1.2 presents an overview of adjoint-based optimization methods in CFD, as developed by the *PCOpt/NTUA* group. Finally, Sec. 1.3 outlines the structure of the thesis.

1.1 Field Inversion

To overcome the limitations of conventional turbulence models in RANS simulations, extensive research over the past decade has focused on the integration of data within physics-based modeling, by extending the Field Inversion and Machine Learning (FI/ML) approach introduced by Duraisamy et al. (2015) [12].

Historically, physical modeling has always incorporated data-driven elements to a degree; a theory or set of theories are formulated, and unknown model coefficients and functions are empirically determined by correlating the response of the model with available data [13]. In a similar manner, the FI procedure adopts an inverse modeling strategy in which the gap between Hi-Fi reference data (e.g., LES, DNS, or experimental measurements) and comparatively Low-Fidelity (Low-Fi) model predictions (e.g., RANS simulations) is systematically minimized through the introduction of a spatially varying correction field. Following the inference of such correction fields across a range of representative flow configurations, ML techniques can optionally be employed to reconstruct the inferred function in terms of variables that are available during predictive simulations with the Low-Fi model [13].

Specifically for turbulence modeling, the objective of FI is to identify an ideal set of corrections β for terms apearing into the RANS turbulence model under study [9] in order to make it better fit to selected Hi-Fi data (e.g., wall pressure, skin-friction, or velocity measurements), while simultaneously preserving the backbone of the baseline model. In particular, excessive deviations from the baseline formulation (corresponding to $\beta = 1$) are undesirable, as they may compromise the consistency of the model and lead to numerical instability or unphysical results. Consider a flow configuration, discretized on a CFD mesh with N_c cells. Given N_d Hi-Fi data points, each associated with the value $G_{j,\mathrm{Hi-Fi}}$ ($j = 1, \ldots, N_d$), the inverse problem for computing the optimal correction field $\beta \equiv \beta(x_n)$, $n = 1, \ldots, N_m$ (where x_n denotes the geometric position of cell n, in a cell-centric finite volume scheme, and $N_m \leq N_c$) is formulated as:

$$\min_{\beta} \sum_{j=1}^{N_d} \left[G_{j,\text{hi-fi}} - G_j(\beta)\right]^2 + \lambda \sum_{n=1}^{N_m} \left[\beta(x_n) - 1\right]^2 \tag{1.1}$$

Here, $G_j(\beta)$ denotes the quantity predicted by the RANS solver under the modified turbulence model [14], and λ is a regularization parameter controlling the trade-off between data fidelity and deviation from the baseline model [15].

A variety of correction parameterizations β have been proposed in the literature, depending on the turbulence model being augmented. For instance, an intermittency field γ was introduced within the k–ω SST model in the original FI study [12]. Other approaches include modifications to the destruction term in k-ω based models [16], the introduction of FI multipliers in the destruction terms of k-ϵ [17], and in the production term of the SA model [18, 19, 20]. Additional approaches include direct corrections to the turbulent eddy viscosity field itself [21, 22, 23], as well as the addition of a non-linear part of Reynolds stress (by adding an extra stess tensor to improve the Boussinesq assumption) [24, 25]. Recently unsteady FI has also been tried out by adding a Brinkman term with a Gaussian impermeability field to the momentum equation (in unsteady-RANS) to change the unsteady vortex evolution [26], demonstrating improved performance compared to steady FI in airfoil stall prediction [27]. It should finally be noted, that the FI framework can be applied to flow models beyond RANS. For example, in a recent study [28], the discrepancy between the vorticity fields of a 2D Leith LES model (here serving as Low-Fi solver) and Hi-Fi DNS data was minimized.

In general, FI has been applied to a wide range of fluid dynamics problems in which classical turbulence models fail to accurately predict the flow field. These applications include flow around airfoils near stall [29, 18], massively separated flows over bumps [30, 31], turbomachinery cascades [19, 32] and spectral proper orthogonal decomposition based problems [33, 23].

Regarding the field or (integral) quantity whose discrepancy is minimized, the velocity field is most commonly employed (either in terms of the axial velocity component or the velocity magnitude), evaluated over the entire computational domain [22] or at selected mesh locations [15]. Alternative formulations have also been proposed based on other flow observables, including the wall Mach number [19], wall friction coefficient [34], wall shear stress [13], and correlations of stochastic forcing terms [33], among others.

The resulting inverse problem is extremely high-dimensional, thus requiring an efficient adjoint-based optimization framework [12]. In this context, the discrete adjoint formulation has been the most widely adopted approach, largely due to the availability of automatic differentiation techniques [12, 21, 19, 16] and symbolic algebra tools [17]. Alternatively, Alessi in his PhD thesis [35], developed a discrete adjoint formulation fully integrated into the CFD solver, whereas Tsolakos [36] adopted a continuous adjoint framework.

Finally, the inferred corrections from FI are subsequently generalized across a range of flow configurations using ML algorithms and incorporated into modified turbulence closure models. Several learning approaches have been explored in the literature, including Artificial Neural Networks (ANNs) [18, 29, 19], Gaussian Processes [12, 13], and Symbolic Regression (SR) [20, 16, 25]. By embedding these learned corrections within RANS formulation, the FI/ML framework enhances predictive capability while preserving the computational efficiency required for practical engineering applications. A key advantage of this approach is that the ML training process is decoupled from the CFD solver, thereby improving overall efficiency by several orders of magnitude [17]. A flowchart of the FI/ML methodology is provided in Fig. 1.2.

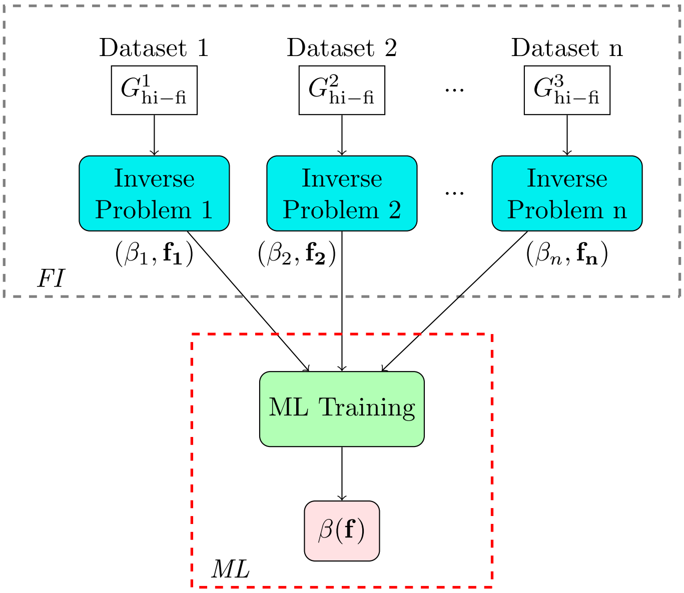

Figure 1.2: *Schematic of the FI/ML framework for data-driven turbulence modeling; n is the number of datasets, $G^i_{\text{hi-fi}}$ is the Hi-Fi data for case i; β_i is the solution of the inverse problem $\min_\beta \left\| G^i_{\text{hi-fi}} - G^i_{\text{rans}}(\beta) \right\|$, the vector $\mathbf{f}_i$ denotes local flow-field quantities (e.g., velocity, strain rate, and vorticity), and $\beta(\mathbf{f})$ represents the ML-based surrogate model.*

However, a decade after the introduction of the FI/ML framework, several critical challenges remain. In particular, overfitting and poor generalization to unseen flow configurations are frequently observed [37]. ML models trained on limited datasets often produce inaccurate predictions when applied to new cases, sometimes performing worse than baseline RANS simulations. This issue is especially pronounced for industrial 3D flows (e.g., around cars), as training datasets are commonly derived from simplified benchmark configurations (e.g., periodic hills, bumps, or airfoils), for which the generation of Hi-Fi data such as LES is computationally feasible.

The present work continues the research of [36], advancing the continuous adjoint method for FI through the implementation of the so-called Eddy Viscosity Adaptation (EVA) approach; a methodology in which β is no more a correction field but stands for the eddy viscosity ν_t field itself, effectively bypassing the requirement for a traditional RANS turbulence model. This study, specifically extends the application of FI to 3D automotive flows, utilizing Detached-Eddy Simulations (DES) [38] as Hi-Fi surrogates to overcome the inherent scarcity of LES, DNS or experimental reference data. Furthermore, new loss functions for quantifying the discrepancy between Low- and Hi-Fi data is investigated.

1.2 Adjoint Optimization in CFD

The adjoint method has emerged as a cornerstone of gradient-based optimization, particularly for industrial applications with a large number of parameters, e.g., shape optimization (ShpO) problems.

Conventional optimization techniques typically become computationally prohibitive as the number of design variables increases, since the required number of flow evaluations scales linearly with the dimensionality of the design space. For example, the finite difference method computes the gradient of an objective function $J(\mathbf{b}, \mathbf{f}(\mathbf{b}))$, where $\mathbf{b} \in \mathbb{R}^N$ represents the vector of N design variables and $\mathbf{f}$ represents the state variables, by perturbing each parameter individually. In a standard forward-difference scheme, the derivative with respect to (w.r.t.) the n-th design variable b_n is approximated as:

$$\frac{\partial J}{\partial b_n} = \frac{J(b_1, \ldots, b_n + \epsilon, \ldots, b_N) - J(b_1, \ldots, b_n, \ldots, b_N)}{\epsilon} + \mathcal{O}(\epsilon) \tag{1.2}$$

where $\epsilon > 0$ is a small perturbation. Because the state vector $\mathbf{f}$ implicitly depends on the modified design variable, evaluating the numerator requires a new, fully converged solution of the underlying state equations for each parameter. Consequently, constructing the full gradient vector requires $N + 1$ CFD evaluations. If a more accurate central-difference scheme is utilized to eliminate first-order truncation errors, the burden increases to $2N$ CFD evaluations:

$$\frac{\partial J}{\partial b_n} = \frac{J(b_1, \ldots, b_n + \epsilon, \ldots, b_N) - J(b_1, \ldots, b_n - \epsilon, \ldots, b_N)}{2\epsilon} + \mathcal{O}(\epsilon^2) \tag{1.3}$$

For modern industrial optimization problems where $N > \mathcal{O}(10^2)$, this approach becomes computationally unfeasible. In contrast, the adjoint method reduces the gradient computation to an $\mathcal{O}(1)$ task that is virtually independent of N [39].

Specifically, the adjoint approach employs Lagrange multipliers to formulate an augmented objective (Lagrangian) function L, defined as the sum of the objective function J and the field integrals of the flow equations multiplied by the corresponding adjoint (or Lagrange multiplier) fields [40]. The adjoint fields are introduced as additional degrees of freedom in order to eliminate the derivatives of the flow variables w.r.t. the design variables b_n from the sensitivity derivative (SD) expressions, i.e., the gradients of the objective function w.r.t. the design variables $\delta L/\delta b_n$. Essentially, $L \equiv J$, $\delta L/\delta b_n = \delta J/\delta b_n$. This elimination is achieved through the satisfaction of the field adjoint equations (FAE) and the corresponding adjoint boundary conditions (ABC). Consequently, once the primal and adjoint problems are solved, the SDs w.r.t. all design variables ($\delta J/\delta b_n$), can be evaluated through the remaining terms of the augmented functional at a computational cost that is practically independent of the number of design parameters [41]. It is widely used today in CFD applications for ShpO, where the objective is to modify the solid boundaries, most commonly, through the use of Non-Uniform Rational B-Splines (NURBS) boxes for geometry parameterization [42, 43], as well as for topology optimization problems, in which the impermeability at each cell of the computational domain is treated as a design variable, representing either fluid or solid material [44].

In the *PCOpt/NTUA* Unit, adjoint methods, mostly continuous but occasionally also discrete, have been developed and employed for more than two decades. Notably, the continuous adjoint method has been integrated into the open-source framework `OpenFOAM` through the `adjointOptimisationFoam` utility [45]. The framework supports both shape and topology optimization problems, a variety of objective functions (e.g., aerodynamic forces on bodies, pressure losses, flow uniformity) [46], different SD computation methods [47, 48], and several design-variable update strategies. Particularly, the SA and k-ω turbulence models have also been differentiated within the adjoint formulation [49, 50], yielding significantly more accurate results compared to the frozen-turbulence assumption [51]. In addition, unsteady adjoint solvers for the unsteady-RANS and DES/SA turbulence model have recently been developed [52].

1.3 Thesis Outline

This thesis aims to employ the continuous adjoint method to solve the FI problem presented in Eq. 1.1, with $\beta = \nu_t$, thereby effectively replacing the turbulence model. Specifically, the EVA method, first introduced in the recent diploma thesis [36], is further developed and investigated, with particular emphasis on 3D cases, where the FI framework has been underexplored in the literature.

The main focus of this work is placed on the FI step. Hi-Fi data of varying quality (experimental, DNS, and DES) are employed as targets in the EVA procedure, while standard (one or two equations) RANS turbulence models (k-ϵ and SA), are used for intialization and comparison purposes with the EVA-based solution. The overall EVA optimization process yields a corrected, **raw eddy viscosity field (rEV)**.

Furthermore, a preliminary ML approach employing SR, based on the work carried out in another diploma thesis running in parallel in the *PCOpt/NTUA* [53], is applied to the EVA-corrected RANS fields in order to identify an analytical expression for ν_t, referred to as the **closed-form eddy viscosity (cfEV)**.

Finally, the derived surrogate turbulence models (rEV and cfEV) are applied to ShpO in a 3D case, once again using the continuous adjoint method (in a different role, though). This is done either under the frozen turbulence assumption or by fully differentiating the newly obtained algebraic relation for ν_t during the derivation the adjoint equations.

The EVA/SR approach enables the exploitation of Hi-Fi datasets in ShpO routines, without requiring the solution of unsteady adjoint equations (e.g, for DES), which typically present significant challenges related to the storage of time-accurate flow fields during backward-in-time integration and numerical convergence [29, 54]. A flowchart of the overall procedure is shown in Fig. 1.3.

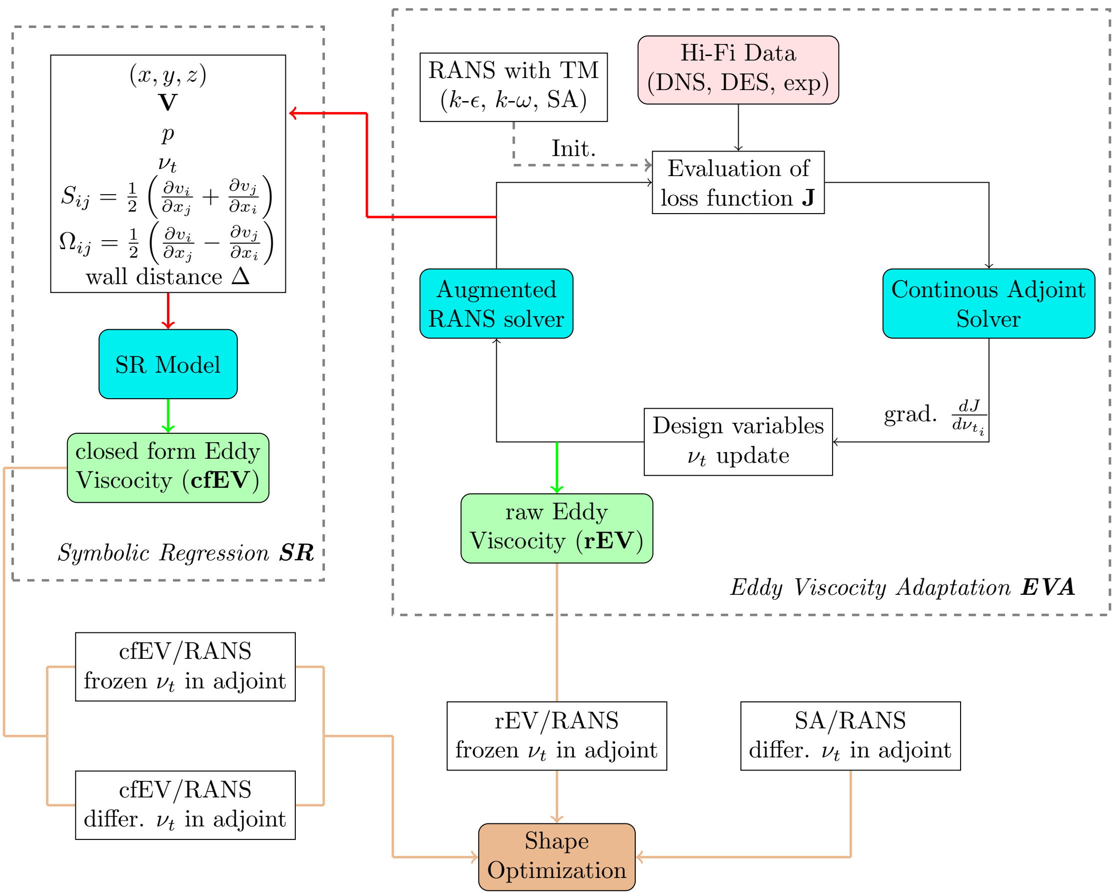

Figure 1.3: *Schematic of the EVA/SR framework for data-driven turbulence modeling used throughout this thesis, preparing the ground for using it in ShpO.*

This Thesis consists of 7 chapters, which are summarized below:

- Chapter 1 is the Introduction.
- Chapter 2 describes the mathematical formulation of the EVA method, starting from the incompressible RANS equations and developing the continuous adjoint method to derive the field adjoint equations, boundary conditions, and the corresponding expressions for the SD. Specific emphasis is placed on the differentiation of wall functions. Different loss functions are considered, including the weighted discrepancy between the velocity fields obtained from the RANS solver and Hi-Fi data, evaluated either over the entire domain or in selected regions, as well as the predicted error in the body's aerodynamic force coefficients (e.g., drag C_D, lift C_L).
- Chapter 3 applies EVA for the 2D periodic hills benchmark [55], a standard case for turbulence model verification. Five variations of steepness ratios are examined using Hi-Fi reference data from DNS. The study evaluates several velocity-based loss functions and compares the results against standard k-ϵ and SA turbulence models.
- Chapter 4 presents the results of EVA application on two coarse meshes, for the flow around the NACA 0012 airfoil near stall. Here, the loss function is defined in terms of aerodynamic performance metrics rather than velocity-field discrepancies; EVA seeks to minimize the differences between the drag and lift coefficients, C_D and C_L, predicted by the Low-Fi RANS solver and the corresponding experimental values.
- Chapter 5 extends the application of the EVA method to 3D external aerodynamics cases involving ground vehicles, with DES serving as the Hi-Fi solver. In particular, the Ahmed body [56], the SAE reference car [57], and the DrivAer Fastback and Estateback variants [58] are investigated.
- Chapter 6 presents a 3D ShpO example; minimizing the C_D of an Ahmed body with a 35° slant angle. The optimization utilizes either the rEV from the EVA method or the cfEV obtained by SR for the corrected RANS field. The results are compared against the classic RANS/SA model.
- Chapter 7 summarizes the conclusions of this work and outlines directions for future research.

Part of this work has also been included in a conference paper [59].

Chapter 2

The Continuous Adjoint Method for Eddy Viscosity Adaptation

In this chapter the mathmeatical formulation of the continuous adjoint method for the EVA for incompressible flow problems is presented.

The starting point of the adjoint formulation is the introduction of the augmented (Lagrangian) function L, defined as:

$$L = J + \int_\Omega u_i R_i^v \, d\Omega + \int_\Omega q R^p \, d\Omega \tag{2.1}$$

where J denotes the loss function to be minimized (i.e., the discrepancy between the RANS solver prediction and the Hi-Fi data), R_i^v the momentum equations, R^p the continuity equation, u_i the adjoint velocity variables, q the adjoint pressure, and Ω the computational domain.

The augmented function is differentiated w.r.t. the correction field for the FI problem; for EVA it coincides with the eddy viscosity field ($\beta = \nu_t$), yielding:

$$\begin{aligned} \frac{\delta L}{\delta \nu_{tp}} &= \frac{\delta J}{\delta \nu_{tp}} + \frac{\delta}{\delta \nu_{tp}} \int_\Omega u_i R_i^v \, d\Omega + \frac{\delta}{\delta \nu_{tp}} \int_\Omega q R^p \, d\Omega \\ &= \underbrace{\frac{\delta J}{\delta \nu_{tp}}}_{T_1} + \underbrace{\int_\Omega u_i \frac{\delta R_i^v}{\delta \nu_{tp}} \, d\Omega}_{T_2} + \underbrace{\int_\Omega q \frac{\delta R^p}{\delta \nu_{tp}} \, d\Omega}_{T_3} \end{aligned} \tag{2.2}$$

where $\nu_{t,p}$ denotes the cell-centered eddy viscosity for cell $p \in [1, N]$. In this formulation, the total number of cells, N, equals the number of design variables.

2.1 Primal Equations

The flow equations are the steady-state RANS equations for incompressible fluids without heat transfer, written as [60]:

$$R^p = -\frac{\partial v_j}{\partial x_j} = 0 \tag{2.3a}$$

$$R_i^v = v_j \frac{\partial v_i}{\partial x_j} - \frac{\partial \tau_{ij}}{\partial x_j} + \frac{\partial p}{\partial x_i} = 0, \quad i = 1, 2(, 3) \tag{2.3b}$$

where p is the static pressure divided by the constant density, v_i are the velocity components, $\tau_{ij} = (\nu + \nu_t)\left(\frac{\partial v_i}{\partial x_j} + \frac{\partial v_j}{\partial x_i}\right)$ is the stress tensor; ν and ν_t the kinematic (bulk) and turbulent (eddy) viscosity, respectively. Throughout this thesis, the Einstein convention is used, according to which repeated indices imply summation, unless otherwise stated.

The boundary conditions associated with $\mathbf{v} = (v_1, v_2, v_3)$, p for Eq. (2.3), are summarized below for the following types of boundaries: inlet (S_I), outlet (S_O), solid walls (S_W) and symmetry (S_S):

$$\begin{aligned}
&S_I : \mathbf{v} = \mathbf{v}_\infty, \ \frac{\partial p}{\partial n} = 0 \\
&S_O : \frac{\partial v_i}{\partial n} = 0, \ p = 0 \\
&S_W : \mathbf{v} = \mathbf{0}, \ \frac{\partial p}{\partial n} = 0 \\
&S_S : v_{\langle n \rangle} = 0 \ , \ \frac{\partial v^l_{\langle t \rangle}}{\partial n} = 0 \ , \ \text{ for } l = I, II \ , \ \frac{\partial p}{\partial n} = 0 \ ,
\end{aligned} \tag{2.4}$$

where $\mathbf{v}_\infty$ denotes the inlet flow velocity. For the symmetry boundary conditions, the formulation is expressed in the local orthogonal Frenet coordinate system defined by the vectors $\mathbf{n}$, $\mathbf{t}^I$, and $\mathbf{t}^{II}$, as illustrated in Fig. 2.1. Quantities $v_{\langle n \rangle} = v_i n_i$ and $v^l_{\langle t \rangle} = v_i t^l_i$, with $l = I, II$, denote the velocity components in the $\mathbf{n}$ and $\mathbf{t}^l$ directions, respectively.

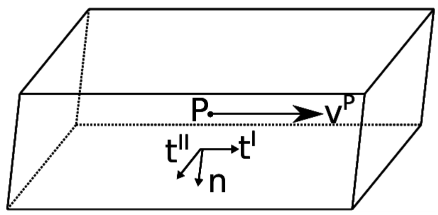

Figure 2.1: *Typical finite-volume cell adjacent to the wall.* $\mathbf{n}$ *denotes the outward unit normal vector,* $\mathbf{t}^I$ *is aligned with the velocity vector at the first cell center* P, *and* $\mathbf{t}^{II} = \mathbf{n} \times \mathbf{t}^I$*; taken from [49].*

2.2 Useful Mathematical Relationships

The subsequent mathematical derivation is based on the total (material) derivative of an arbitrary quantity $\Phi = \Phi(\boldsymbol{b}, \boldsymbol{f}(\boldsymbol{b}))$ w.r.t. a set of design variables b_n, $n \in [1, N]$, denoted by $\delta\Phi/\delta b_n$, which accounts for the total change in Φ due to variations in b_n. This reads:

$$\frac{\delta \Phi}{\delta b_n} = \frac{\partial \Phi}{\partial b_n} + \frac{\partial \Phi}{\partial x_k}\frac{\delta x_k}{\delta b_n} \tag{2.5}$$

The first term on the right-hand-side (partial derivative) represents variations in Φ caused by changes in the flow variables, excluding spatial deformations (continuous sense) or grid displacements (discrete sense), which are accounted for, by the second term [49]. In the EVA framework $b_n = \nu_{tp}$; since the geometry does not change, Eq. (2.5) simplifies to:

$$\frac{\delta \Phi}{\delta b_n} = \frac{\partial \Phi}{\partial b_n} \tag{2.6}$$

Spatial and partial derivatives w.r.t. the design variables commute, according to Schwarz's theorem:

$$\frac{\partial}{\partial b_n}\left(\frac{\partial \Phi}{\partial x_j}\right) = \frac{\partial}{\partial x_j}\left(\frac{\partial \Phi}{\partial b_n}\right). \tag{2.7}$$

This relation is used in the following sections to isolate the terms $\partial v_i/\partial b_n$ and $\partial p/\partial b_n$. By doing so, the direct calculation of these terms is avoided through the derivation of the FAE, and their associated ABC.

Additionally, spatial and total derivatives w.r.t. b_n are linked through [52]:

$$\frac{\delta}{\delta b_n}\left(\frac{\partial \Phi}{\partial x_j}\right) = \frac{\partial}{\partial x_j}\left(\frac{\partial \Phi}{\partial b_n}\right) - \frac{\partial \Phi}{\partial x_k}\frac{\partial}{\partial x_j}\left(\frac{\delta x_k}{\delta b_n}\right) \tag{2.8}$$

Since $\delta x_k/\delta \nu_t = 0$, according to Eq. (2.7) the following simplified expression is obtained:

$$\frac{\delta}{\delta \nu_{tp}}\left(\frac{\partial \Phi}{\partial x_j}\right) = \frac{\partial}{\partial x_j}\left(\frac{\partial \Phi}{\partial \nu_{tp}}\right) \tag{2.9}$$

Finally, another relation that will be applied is the Green-Gauss theorem. Using Eq. (2.9):

$$\int_\Omega a \frac{\delta}{\delta x_k}\left(\frac{\partial \Phi}{\partial b_n}\right) d\Omega = \int_S a \frac{\partial \Phi}{\partial b_n} n_j \, dS - \int_\Omega \frac{\partial a}{\partial x_j}\frac{\partial \Phi}{\partial b_n} d\Omega \tag{2.10}$$

2.3 Differentiation of the Loss Functions

In this section, the first term (T_1) in Eq. (2.2) is developed according to the loss function to be minimized.

2.3.1 Discrepancy between RANS & Hi-Fi Velocity Fields

The velocity field ($\mathbf{v}_{\text{hi-fi}}$) computed by the Hi-Fi flow model is the target to be reproduced by the solution of the RANS equations. This is achieved by determining a ν_t field that minimizes the following loss function:

$$J_v = \frac{1}{2}\int_{\Omega_E} w_p \left(v_i - v_{i,\text{hi-fi}}\right)^2 d\Omega_E \tag{2.11}$$

where Ω_E represents either the entire computational domain Ω or a part of it, w_p denotes the weighting factors (defined per cell p), and index i implies summation over the spatial components (x, y, z).

The calculation of Eq. (2.2) requires the differentiation of the loss function w.r.t. $\nu_{t,p}$; using the chain-rule:

$$\frac{\delta J}{\delta \nu_{tp}} = \frac{\partial J}{\partial v_i}\frac{\delta v_i}{\delta \nu_{tp}} + \frac{\partial J}{\partial p}\frac{\delta p}{\delta \nu_{tp}} + \frac{\partial J}{\partial \tau_{ij}}\frac{\delta \tau_{ij}}{\delta \nu_{tp}} \tag{2.12}$$

The last term in Eq. (2.12) is included to take possible dependencies of J on differential expressions into consideration, since in the continuous regime, these cannot be analyzed through $\partial J/\partial v_k$ or $\partial J/\partial p$ [46]. For the loss function in Eq. (2.11), substituting also Eq. (2.9), yields:

$$\frac{\delta J_v}{\delta \nu_{tp}} = \frac{\partial J_v}{\partial v_i}\frac{\partial v_i}{\partial \nu_{tp}} + \frac{\partial J_v}{\partial p}\frac{\partial p}{\partial \nu_{tp}} = \int_{\Omega_E} \frac{\partial j_v}{\partial v_i}\frac{\partial v_i}{\partial \nu_{tp}} d\Omega + \int_{\Omega_E} \frac{\partial j_v}{\partial p}\frac{\partial p}{\partial \nu_{tp}} d\Omega \tag{2.13}$$

where $j_v = \frac{1}{2}\, w_p \, (v_i - v_{i,\text{hi-fi}})^2$. Substituting it into Eq. 2.13:

$$\begin{aligned}\frac{\delta J_v}{\delta \nu_{t,p}} &= \int_{\Omega_E} w_p \, (v_i - v_{i,\text{hi-fi}}) \, \frac{\partial v_i}{\partial \nu_{tp}} d\Omega_E + \int_{\Omega_E} 0 \, \frac{\partial p}{\partial \nu_{tp}} d\Omega_E \\ &= \underline{\int_{\Omega} w_p \, (v_i - v_{i,\text{hi-fi}}) \, \mathbb{I}_{\Omega_E} \frac{\partial v_i}{\partial \nu_{tp}} d\Omega} \quad , \text{ where } \mathbb{I}_{\Omega_E} = \begin{cases} 1 \ , \ \mathbf{x} \in \Omega_E \\ 0 \ , \ \mathbf{x} \notin \Omega_E \end{cases}\end{aligned} \tag{2.14}$$

2.3.2 Discrepancy between RANS & Hi-Fi Aerodynamic Force Coefficients

In external aerodynamic applications, the EVA can be formulated with the objective of matching the drag or lift coefficient obtained from Hi-Fi data ($C_{D,\text{hi-fi}}$, $C_{L,\text{hi-fi}}$). The corresponding loss function for C_D is defined as:

$$J_f = \frac{1}{2}\,(C_D - C_{D,\text{hi-fi}})^2 \tag{2.15}$$

with the drag coefficient given as:

$$C_D = \frac{F_D}{\frac{1}{2}\,\|\mathbf{v}_\infty\|^2 c} \tag{2.16}$$

where F_D denotes the aerodynamic drag force, $\|\mathbf{v}_\infty\|$ is the freestream velocity magnitude, and c is a reference length.

In a general coordinate system, the aerodynamic force component exerted on a solid body along a specified direction vector $\mathbf{r}$ is computed via the surface integral:

$$F_r = \int_{S_W} \left(-\tau_{ij} + p\,\delta_{ij}\right) n_j\, r_i\, dS \tag{2.17}$$

with δ_{ij} denoting the Kronecker delta, equal to 1 for $i = j$ and 0 otherwise. Accordingly, the total drag force F_D acting on the body is isolated by aligning the projection vector $\mathbf{r} = \mathbf{r}^{(D)}$ parallel to the freestream velocity vector.

The loss function is differentiated w.r.t. ν_{tp} accordingly to Eq. (2.12), yielding:

$$\begin{aligned}\frac{\delta J_f}{\partial \nu_{t,p}} &= \frac{\partial J_f}{\partial v_i}\frac{\partial v_i}{\partial \nu_{tp}} + \frac{\partial J_f}{\partial p}\frac{\partial p}{\partial \nu_{tp}} + \frac{\partial J_f}{\partial \tau_{ij}}\frac{\partial \tau_{ij}}{\partial \nu_{tp}} \\ &= \int_{S_w} \underbrace{\frac{\partial j_f}{\partial v_i}}_{I}\frac{\partial v_i}{\partial \nu_{tp}} dS + \int_{S_w} \underbrace{\frac{\partial j_f}{\partial p}}_{II}\frac{\partial p}{\partial \nu_{tp}} dS + \int_{S_w} \underbrace{\frac{\partial j_f}{\partial \tau_{ij}}}_{III}\frac{\partial \tau_{ij}}{\partial \nu_{tp}} dS\end{aligned} \tag{2.18}$$

where based on Eq. (2.17) and Eq. (2.16), $j_f = \dfrac{1}{2}\left(\dfrac{\left(-\tau_{ij} + p\,\delta_{ij}\right)}{\frac{1}{2}\,\|\mathbf{v}_\infty\|^2 c}\, n_j\; r_i^{(D)} - C_{D\text{hi-fi}}\right)^2$.

Calculation of term I in Eq. (2.18)

$$\begin{aligned}\frac{\partial j_f}{\partial v_i} &= \left(C_D - C_{D\text{hi-fi}}\right)\frac{\partial C_D}{\partial v_i} = \underbrace{\frac{C_D - C_{D\text{hi-fi}}}{\frac{1}{2}\|\mathbf{v}_\infty\|^2 c}}_{\kappa} \int_{S_W} \frac{\partial}{\partial v_i}\left[\left(-\tau_{ij} + p\,\delta_{ij}\right) n_j\, r_i^{(D)}\right] dS \\ &= -\kappa \int_{S_W} n_j r_i^{(D)} \frac{\partial}{\partial v_i}\left[\left(\nu + \nu_t\right)\left(\frac{\partial v_i}{\partial x_j} + \frac{\partial v_j}{\partial x_i}\right)\right] dS \\ &= -\kappa \int_{S_W} n_j r_i^{(D)} \left(\nu + \nu_t\right)\left[\frac{\partial}{\partial x_j}\left(\frac{\partial v_i}{\partial v_i}\right) + \frac{\partial}{\partial x_i}\left(\frac{\partial v_j}{\partial v_i}\right)\right] dS = 0\end{aligned} \tag{2.19}$$

Calculation of term II in Eq. (2.18)

$$\begin{aligned}\frac{\partial j_f}{\partial p} &= \left(C_D - C_{D\text{hi-fi}}\right)\frac{\partial C_D}{\partial p} = \kappa \int_{S_W} \frac{\partial}{\partial p}\left[\left(-\tau_{ij} + p\,\delta_{ij}\right) n_j\, r_i^{(D)}\right] dS \\ &= \kappa \int_{S_W} \delta_{ij}\, n_j\, r_i^{(D)} dS\end{aligned} \tag{2.20}$$

Calculation of term III in Eq. (2.18)

$$\begin{aligned}\frac{\partial j_f}{\partial \tau_{ij}} &= \left(C_D - C_{D\text{hi-fi}}\right)\frac{\partial C_D}{\partial \tau_{ij}} = \kappa \int_{S_W} \frac{\partial}{\partial \tau_{ij}}\left[\left(-\tau_{ij} + p\,\delta_{ij}\right) n_j\, r_i^{(D)}\right] dS \\ &= -\kappa \int_{S_W} n_j r_i^{(D)} dS\end{aligned} \tag{2.21}$$

Substituting the results from Eqs. (2.19), (2.20), and (2.21) into Eq. (2.18):

$$\frac{\delta J_f}{\partial \nu_{t,p}} = \underline{\kappa \int_{S_W} \delta_{ij}\, n_j\, r_i^{(D)} \frac{\partial p}{\partial \nu_{tp}} dS - \kappa \int_{S_W} n_j\, r_i^{(D)} \frac{\partial \tau_{ij}}{\partial \nu_{tp}} dS} \tag{2.22}$$

2.4 Complete Differentiation of the Augmented Function

To compute the SD, the second and third term in Eq. (2.2) must also be evaluated, by differentiating the continuity and momentum RANS equations w.r.t. the design variables.

Calculation of term $\mathbf{T_2}$ in Eq. (2.2)

$$\int_\Omega u_i \frac{\delta R_i^v}{\delta \nu_{tp}} d\Omega = \underbrace{\int_\Omega u_i \frac{\delta}{\delta \nu_{tp}} \left(v_j \frac{\partial v_i}{\partial x_j} \right) d\Omega}_{I} + \underbrace{\int_\Omega -u_i \frac{\delta}{\delta \nu_{tp}} \left[\frac{\partial}{\partial x_j} \left((\nu + \nu_t) \left(\frac{\partial v_i}{\partial x_j} + \frac{\partial v_j}{\partial x_i} \right) \right) \right] d\Omega}_{II}$$
$$+ \underbrace{\int_\Omega u_i \frac{\delta}{\delta \nu_{tp}} \left(\frac{\partial p}{\partial x_i} \right) d\Omega}_{III} \tag{2.23}$$

with each term requiring further analysis.

Calculation of term I in Eq. (2.23)

$$\begin{aligned} I &= \int_\Omega u_i \left(\frac{\delta v_j}{\delta \nu_{tp}} \frac{\partial v_i}{\partial x_j} + v_j \frac{\delta}{\delta \nu_{tp}} \left(\frac{\partial v_i}{\partial x_j} \right) \right) d\Omega = \int_\Omega u_i \frac{\partial v_j}{\partial \nu_{tp}} \frac{\partial v_i}{\partial x_j} d\Omega + \int_\Omega u_i v_j \frac{\partial}{\partial x_j} \left(\frac{\partial v_i}{\partial \nu_{tp}} \right) d\Omega \\ &= \int_\Omega \left(u_i \frac{\partial v_i}{\partial x_j} \right) \frac{\partial v_j}{\partial \nu_{tp}} d\Omega + \int_S (u_i v_j n_j) \frac{\partial v_i}{\partial \nu_{tp}} dS - \int_\Omega \frac{\partial (u_i v_j)}{\partial x_j} \frac{\partial v_i}{\partial \nu_{tp}} d\Omega \\ &= \int_\Omega \left(u_j \frac{\partial v_j}{\partial x_i} \right) \frac{\partial v_i}{\partial \nu_{tp}} d\Omega + \int_S (u_i v_j n_j) \frac{\partial v_i}{\partial \nu_{tp}} dS - \int_\Omega \frac{\partial (u_i v_j)}{\partial x_j} \frac{\partial v_i}{\partial \nu_{tp}} d\Omega \end{aligned} \tag{2.24}$$

Calculation of term II in Eq. (2.23)

$$\begin{aligned} II &= -\int_\Omega u_i \frac{\partial}{\partial x_j} \left[\frac{\partial}{\partial \nu_{tp}} \left((\nu + \nu_t) \left(\frac{\partial v_i}{\partial x_j} + \frac{\partial v_j}{\partial x_i} \right) \right) \right] d\Omega \\ &= -\int_S u_i n_j \frac{\partial \tau_{ij}}{\partial \nu_{tp}} dS + \underbrace{\int_\Omega \frac{\partial u_i}{\partial x_j} \left[\frac{\partial}{\partial \nu_{tp}} \left((\nu + \nu_t) \left(\frac{\partial v_i}{\partial x_j} + \frac{\partial v_j}{\partial x_i} \right) \right) \right] d\Omega}_{a_2} \end{aligned} \tag{2.25}$$

with the last term a_2 further analyzed as:

$$
\begin{aligned}
a_2 &= \int_\Omega \frac{\partial u_i}{\partial x_j}\frac{\partial(\nu+\nu_t)}{\partial \nu_{tp}}\left(\frac{\partial v_i}{\partial x_j}+\frac{\partial v_j}{\partial x_i}\right)d\Omega + \int_\Omega \frac{\partial u_i}{\partial x_j}(\nu+\nu_t)\frac{\partial}{\partial \nu_{tp}}\left(\frac{\partial v_i}{\partial x_j}+\frac{\partial v_j}{\partial x_i}\right)d\Omega \\
&= \int_\Omega \frac{\partial u_i}{\partial x_j}\frac{\partial \nu_t}{\partial \nu_{tp}}\left(\frac{\partial v_i}{\partial x_j}+\frac{\partial v_j}{\partial x_i}\right)d\Omega \\
&\quad + \int_\Omega (\nu+\nu_t)\frac{\partial u_i}{\partial x_j}\frac{\partial}{\partial x_j}\left(\frac{\partial v_i}{\partial \nu_{tp}}\right)d\Omega + \int_\Omega (\nu+\nu_t)\frac{\partial u_i}{\partial x_j}\frac{\partial}{\partial x_i}\left(\frac{\partial v_j}{\partial \nu_{tp}}\right)d\Omega \\
&= \int_\Omega \frac{\partial u_i}{\partial x_j}\frac{\partial \nu_t}{\partial \nu_{tp}}\left(\frac{\partial v_i}{\partial x_j}+\frac{\partial v_j}{\partial x_i}\right)d\Omega \\
&\quad + \left[\int_S (\nu+\nu_t)\frac{\partial u_i}{\partial x_j}\frac{\partial v_i}{\partial \nu_{tp}}n_j dS - \int_\Omega \frac{\partial}{\partial x_j}\left((\nu+\nu_t)\frac{\partial u_i}{\partial x_j}\right)\frac{\partial v_i}{\partial \nu_{tp}}d\Omega\right] \\
&\quad + \left[\int_S (\nu+\nu_t)\frac{\partial u_i}{\partial x_j}\frac{\partial v_j}{\partial \nu_{tp}}n_i dS - \int_\Omega \frac{\partial}{\partial x_i}\left((\nu+\nu_t)\frac{\partial u_i}{\partial x_j}\right)\frac{\partial v_j}{\partial \nu_{tp}}d\Omega\right] \\
&= \int_\Omega \frac{\partial u_i}{\partial x_j}\frac{\partial \nu_t}{\partial \nu_{tp}}\left(\frac{\partial v_i}{\partial x_j}+\frac{\partial v_j}{\partial x_i}\right)d\Omega \\
&\quad + \left[\int_S (\nu+\nu_t)\frac{\partial u_i}{\partial x_j}\frac{\partial v_i}{\partial \nu_{tp}}n_j dS - \int_\Omega \frac{\partial}{\partial x_j}\left((\nu+\nu_t)\frac{\partial u_i}{\partial x_j}\right)\frac{\partial v_i}{\partial \nu_{tp}}d\Omega\right] \\
&\quad + \left[\int_S (\nu+\nu_t)\frac{\partial u_j}{\partial x_i}\frac{\partial v_i}{\partial \nu_{tp}}n_j dS - \int_\Omega \frac{\partial}{\partial x_j}\left((\nu+\nu_t)\frac{\partial u_j}{\partial x_i}\right)\frac{\partial v_i}{\partial \nu_{tp}}d\Omega\right] \\
&= \int_\Omega \frac{\partial u_i}{\partial x_j}\frac{\partial \nu_t}{\partial \nu_{tp}}\left(\frac{\partial v_i}{\partial x_j}+\frac{\partial v_j}{\partial x_i}\right)d\Omega + \int_S (\nu+\nu_t)\left(\frac{\partial u_i}{\partial x_j}+\frac{\partial u_j}{\partial x_i}\right)\frac{\partial v_i}{\partial \nu_{tp}}n_j dS \\
&\quad - \int_\Omega \frac{\partial}{\partial x_j}\left((\nu+\nu_t)\left(\frac{\partial u_i}{\partial x_j}+\frac{\partial u_j}{\partial x_i}\right)\right)\frac{\partial v_i}{\partial \nu_{tp}}d\Omega
\end{aligned}
\tag{2.26}
$$

Calculation of term III in Eq. (2.23)

$$
III = \int_\Omega u_i \frac{\partial}{\partial x_i}\left(\frac{\partial p}{\partial \nu_{tp}}\right)d\Omega = \int_S u_i n_i \frac{\partial p}{\partial \nu_{tp}}\,dS - \int_\Omega \frac{\partial u_i}{\partial x_i}\frac{\partial p}{\partial \nu_{tp}}\,d\Omega \tag{2.27}
$$

Calcuation of term $\mathbf{T_3}$ in Eq. (2.2)

$$
\begin{aligned}
\int_\Omega q\frac{\delta R_p}{\delta \nu_{tp}}d\Omega &= -\int_\Omega q\frac{\delta}{\delta \nu_{tp}}\left(\frac{\partial v_j}{\partial x_j}\right)d\Omega = -\int_\Omega q\frac{\partial}{\partial x_j}\left(\frac{\partial v_j}{\partial \nu_{tp}}\right)d\Omega \\
&= -\int_S q\frac{\partial v_j}{\partial \nu_{tp}}n_j dS + \int_\Omega \frac{\partial q}{\partial x_j}\frac{\partial v_j}{\partial \nu_{tp}} \\
&= -\int_S q\frac{\partial v_i}{\partial \nu_{tp}}n_i dS + \int_\Omega \frac{\partial q}{\partial x_i}\frac{\partial v_i}{\partial \nu_{tp}}d\Omega
\end{aligned}
\tag{2.28}
$$

Final Formulation of Eq. (2.2)

Consider a loss function defined as:

$$J = W_1 J_v + W_2 J_f \tag{2.29}$$

where J_v represents the velocity difference objective, Eq. (2.11), J_f denotes the aerodynamic coefficient objective, Eq. (2.15), and W_1, W_2 are the respective weighting factors.

Substituting the expressions for the sensitivities $\delta J_v/\delta\nu_{tp}$, Eq. (2.14) and $\delta J_f/\delta\nu_{tp}$, Eq. (2.22) into the first term (T_1) of the differentiated augmented Lagrangian functional $\delta L/\delta\nu_{tp}$, Eq. (2.2), together with the corresponding updates for its second term (T_2), Eq. (2.24)–(2.27) and third term (T_3), Eq. (2.28), yields the following expression:

$$\begin{aligned}
\frac{\delta L}{\delta\nu_{tp}} =& \int_\Omega \Bigg[\underline{W_1 w_p \left(v_i - v_{i,\text{hi-fi}}\right) \mathbb{I}_{\Omega_E}} + \frac{\partial q}{\partial x_i} + u_j \frac{\partial v_j}{\partial x_i} - \frac{\partial (u_i v_j)}{\partial x_j} \\
&- \frac{\partial}{\partial x_j}\left((\nu + \nu_t) \left(\frac{\partial u_i}{\partial x_j} + \frac{\partial u_j}{\partial x_i} \right) \right) \Bigg] \frac{\partial v_i}{\partial \nu_{tp}} d\Omega \\
&+ \int_\Omega \left[-\frac{\partial u_i}{\partial x_i} \right] \frac{\partial p}{\partial \nu_{tp}} d\Omega \\
&+ \int_\Omega \frac{\partial u_i}{\partial x_j} \frac{\delta \nu_t}{\delta \nu_{tp}} \left(\frac{\partial v_i}{\partial x_j} + \frac{\partial v_j}{\partial x_i} \right) d\Omega \\
&+ \int_S \left[-q n_i + u_i v_j n_j + (\nu + \nu_t) \left(\frac{\partial u_i}{\partial x_j} + \frac{\partial u_j}{\partial x_i} \right) n_j \right] \frac{\partial v_i}{\partial \nu_{tp}} dS \\
&+ \int_S \left[\underline{W_2 \kappa n_i r_i^{(D)} \mathbb{I}_{S_w}} + u_i n_i \right] \frac{\partial p}{\partial \nu_{tp}} dS \\
&+ \int_S \left[\underline{-W_2 \kappa n_j r_i^{(D)} \mathbb{I}_{S_w}} - u_i n_j \right] \frac{\partial \tau_{ij}}{\partial \nu_{tp}} dS
\end{aligned} \tag{2.30}$$

2.5 Field Adjoint Equations

To avoid computing derivatives w.r.t. the flow variables in Eq. (2.30) (which is the fundamental purpose of the adjoint approach), the corresponding multipliers in the volume integrals are set to zero. This leads to the FAE, which can be expressed in the following form:

$$R^q = -\frac{\partial u_i}{\partial x_i} = 0 \tag{2.31a}$$

$$R_i^u = W_1 w_p \left(v_i - v_{i,\text{hi-fi}}\right) \mathbb{I}_{\Omega_E} + \frac{\partial q}{\partial x_i} + u_j \frac{\partial v_j}{\partial x_i} - \frac{\partial (u_i v_j)}{\partial x_j}$$

$$-\frac{\partial}{\partial x_j}\left[(\nu+\nu_t)\left(\frac{\partial u_i}{\partial x_j}+\frac{\partial u_j}{\partial x_i}\right)\right]=0 \tag{2.31b}$$

where the first term in the adjoint momentum equation arises from the differentiation of the velocity-difference loss function and is only active in the cells where this contribution is defined (i.e., within Ω_E).

2.6 Adjoint Boundary Conditions

The remaining terms in the SD calculation (Eq. (2.30)), after neglecting the FAE terms, are:

$$\begin{aligned}
\frac{\delta L}{\delta \nu_{tp}} = & \underbrace{\int_\Omega \frac{\partial u_i}{\partial x_j}\frac{\delta \nu_t}{\delta \nu_{tp}}\left(\frac{\partial v_i}{\partial x_j}+\frac{\partial v_j}{\partial x_i}\right)d\Omega}_{T_1} \\
& + \underbrace{\int_S \left[-q n_i + u_i v_j n_j + (\nu+\nu_t)\left(\frac{\partial u_i}{\partial x_j}+\frac{\partial u_j}{\partial x_i}\right)n_j\right]\frac{\partial v_i}{\partial \nu_{tp}}dS}_{T_2} \\
& + \underbrace{\int_S \left[\underline{W_2 \kappa n_i r_i^{(D)}\mathbb{I}_{S_w}} + u_i n_i\right]\frac{\partial p}{\partial \nu_{tp}}dS}_{T_3} \\
& + \underbrace{\int_S \left[\underline{-W_2 \kappa n_j r_i^{(D)}\mathbb{I}_{S_w}} - u_i n_j\right]\frac{\partial \tau_{ij}}{\partial \nu_{tp}}dS}_{T_4}
\end{aligned} \tag{2.32}$$

Similarly to the volume integrals, in order to avoid computing the surface contributions involving $\partial p/\partial \nu_{tp}$, $\partial v_i/\partial \nu_{tp}$, and $\partial \tau_{ij}/\partial \nu_{tp}$, appropriate ABC must be derived.

Inlet Boundaries (S_I)

At the inlet patches (S_I), as presented in Eq. (2.4) , Dirichlet conditions are imposed on the velocity components and a Neumann zero-gradient condition on the pressure. Since the inlet velocity does not depend on ν_t, it follows that $\partial v_i/\partial \nu_{tp} = 0$; consequently, term T_2 in Eq. (2.32) vanishes identically.

For the elimination of terms T_3 and T_4 in the same equation, the analysis is performed in the local orthogonal Frenet coordinate (illustrated in Fig. 2.1). Within this framework, the adjoint velocity vector is decomposed into one normal and two tangential components as follows:

$$\mathbf{u} = u_{\langle n\rangle}\mathbf{n} + u^I_{\langle t\rangle}\mathbf{t}^I + u^{II}_{\langle t\rangle}\mathbf{t}^{II} \tag{2.33}$$

where quantities $u_{\langle n\rangle} = u_i n_i$ and $u_{\langle t^l\rangle} = u_i t^l_i,\ l = I, II$ are the adjoint velocity components in the $\mathbf{n}$ and $\mathbf{t}^l$, $l = I, II$ directions, respectively.

Because the inlet is not part of the wall boundary ($S_I \cap S_W = \emptyset$), the third term (T_3) in Eq. 2.32 vanishes since $u_{\langle n\rangle} = u_i n_i = 0$. Similarly, the fourth term (T_4) vanishes due to the condition $u_i n_j = 0$, which implies that the tangential velocity components satisfy $u^l_{\langle t\rangle} = u_i t^l_i = 0$ for $l = \mathrm{I}, \mathrm{II}$. according to the decomposition in Eq. (2.33), this results in $\mathbf{u} = \mathbf{0}$ on the inlet boundary.

Finally, since no boundary condition for q results from the elimination of any of the boundary integrals in Eq. (2.32), a zero Neumann condition is employed: $\dfrac{\partial q}{\partial x_j} n_j = 0$.

Outlet Boundaries (S_O)

At the outlet patches (S_O), a zero-gradient condition is imposed on the velocity components and a Dirichlet condition is prescribed for the pressure p. Consequently, $\partial p / \partial \nu_{tp} = 0$, causing the third term (T_3) in Eq. (2.32) to vanish.

Furthermore, given the large distance between the outlet boundary and the control region, the velocity profile along S_O can be assumed to be uniform [49]. This yields:

$$\left.\frac{\partial v_i}{\partial x_j}\right|_{S_O} = \left.\frac{\partial v_j}{\partial x_i}\right|_{S_O} = 0 \implies \tau_{ij} = 0\,, \tag{2.34}$$

which implies that $\partial \tau_{ij} / \partial \nu_{tp} = 0$, thereby eliminating the fourth term (T_4) in Eq. (2.32).

Finally, to eliminate the first surface integral term (T_2) in Eq. (2.32), the remaining integrand expression is set to zero:

$$-q n_i + u_i v_j n_j + (\nu + \nu_t)\left(\frac{\partial u_i}{\partial x_j} + \frac{\partial u_j}{\partial x_i}\right) n_j = 0\,, \quad i = 1, 2, 3\,. \tag{2.35}$$

In 3D flows, Eq. (2.35) comprises four unknowns: the three components of the adjoint velocity field and the adjoint pressure. To close this system, one of these variables must be extrapolated from the interior of the computational domain; in this framework, the normal adjoint velocity component $u_{(n)}$ is extrapolated. Multiplying Eq. (2.35) by the outward unit normal vector n_i yields the boundary condition for the adjoint pressure:

$$q = u_{\langle n\rangle} v_{\langle n\rangle} + 2(\nu + \nu_t)\frac{\partial u_{\langle n\rangle}}{\partial n}\,. \tag{2.36}$$

Similarly, projecting Eq. (2.35) onto the local unit tangent vectors t^l_i (where $l = \mathrm{I}, \mathrm{II}$) isolates the tangential components of the adjoint velocity:

$$v_{\langle n\rangle} u^l_{\langle t\rangle} + (\nu + \nu_t)\left(\frac{\partial u^l_{\langle t\rangle}}{\partial n} + \frac{\partial u_{\langle n\rangle}}{\partial t^l}\right) = 0 \tag{2.37}$$

which are implemented as Robin-type boundary conditions.

Solid Walls (S_W)

Along S_W, the primal boundary conditions are of the same type to those imposed at the inlet boundaries. Consequently, $\mathbf{v} = \mathbf{0}$ yields $\partial v_i/\partial \nu_{tp} = 0$ and, therefore, term T_2 in Eq. (2.32) vanishes.

For the solid walls over which the aerodynamic coefficient C_D is evaluated, the following conditions are imposed in order to eliminate term T_3 in Eq. (2.32):

$$W_2 \kappa n_i r_i^{(D)} + u_i n_i = 0 \tag{2.38}$$

yielding the adjoint boundary condition $u_{\langle n \rangle} = -W_2 \kappa n_i r_i^{(D)}$.

The last term in Eq. (2.32) (term T_4) can be written, using the local Frenet system, as:

$$\begin{aligned}
T_4 &= \int_{S_W} \left[-W_2 \kappa n_j r_i^{(D)} \right] \frac{\partial \tau_{ij}}{\partial \nu_{tP}} \, dS - \int_{S_W} u_{\langle n \rangle} n_i n_j \frac{\partial \tau_{ij}}{\partial \nu_{tp}} \, dS - \int_{S_W} u_{\langle t \rangle}^{I} t_i^{I} n_j \frac{\partial \tau_{ij}}{\partial \nu_{tp}} \, dS \\
&\quad - \int_{S_W} u_{\langle t \rangle}^{II} t_i^{II} n_j \frac{\partial \tau_{ij}}{\partial \nu_{tp}} \, dS \\
&= \int_{S_W} \left[-W_2 \kappa n_j r_i^{(D)} \right] \frac{\partial \tau_{ij}}{\partial \nu_{tP}} \, dS - \int_{S_W} \left(-W_2 \kappa n_i r_i^{(D)} \right) n_i n_j \frac{\partial \tau_{ij}}{\partial \nu_{tp}} \, dS \\
&\quad - \int_{S_W} u_{\langle t \rangle}^{I} t_i^{I} n_j \frac{\partial \tau_{ij}}{\partial \nu_{tp}} \, dS - \int_{S_W} u_{\langle t \rangle}^{II} t_i^{II} n_j \frac{\partial \tau_{ij}}{\partial \nu_{tp}} \, dS \\
&= - \int_{S_W} u_{\langle t \rangle}^{I} t_i^{I} n_j \frac{\partial \tau_{ij}}{\partial \nu_{tp}} \, dS - \int_{S_W} u_{\langle t \rangle}^{II} t_i^{II} n_j \frac{\partial \tau_{ij}}{\partial \nu_{tp}} \, dS
\end{aligned} \tag{2.39}$$

To avoid computing $\partial \tau_{ij}/\partial \nu_{tp}$, the adjoint boundary conditions $u_{\langle t \rangle}^{I} = u_{\langle t \rangle}^{II} = 0$ are applied.

It should be noted that for solid walls that do not contribute to the evaluation of C_D (e.g., the floor of a wind tunnel in a 3D vehicle simulation), the above relations reduce to homogeneous conditions $\mathbf{u} = \mathbf{0}$ (since $u_{\langle n \rangle} = 0$). Finally, independently of the preceding eliminations, a Neumann boundary condition is imposed on the adjoint pressure q.

Symmetry Planes (S_S)

Over the symmetry planes, if present, as defined in Eq. (2.4), the normal velocity component and the normal gradients of the tangential velocity components equal to zero, while a zero-gradient condition is imposed on p. Since J is never defined on the symmetry planes of the domain, all quantities depending on it are omitted from the integrals in Eq. (2.32) (namely the underlined terms).

T_3 of Eq. (2.32) is eliminated by applying a zero normal adjoint velocity $u_{\langle n \rangle} = 0$.

The integrand of T_4 in Eq. (2.32):

$$\begin{aligned}
&- u_i n_j \frac{\partial}{\partial \nu_{tp}} \left[(\nu + \nu_t) \left(\frac{\partial v_i}{\partial x_j} + \frac{\partial v_j}{\partial x_i} \right) \right] \\
&\qquad = (-u_{\langle n \rangle} n_i n_j - u^l_{\langle t \rangle} t^l_i n_j) \frac{\partial}{\partial \nu_{tp}} \left[(\nu + \nu_t) \left(\frac{\partial v_i}{\partial x_j} + \frac{\partial v_j}{\partial x_i} \right) \right] \\
&\qquad = -u^l_{\langle t \rangle} t^l_i n_j \frac{\partial}{\partial \nu_{tp}} \left[(\nu + \nu_t) \left(\frac{\partial v_i}{\partial x_j} + \frac{\partial v_j}{\partial x_i} \right) \right] \\
&\qquad = -u^l_{\langle t \rangle} \frac{\partial}{\partial \nu_{tp}} \left[(\nu + \nu_t) \left(\frac{\partial v_i}{\partial x_j} + \frac{\partial v_j}{\partial x_i} \right) n_j t^l_i \right] \\
&\qquad = -u^l_{\langle t \rangle} \frac{\partial}{\partial \nu_{tp}} \left[(\nu + \nu_t) \left(\frac{\partial v^l_{\langle t \rangle}}{\partial n} + \frac{\partial v_{\langle n \rangle}}{\partial t^l} \right) \right] = 0 \qquad (2.40)
\end{aligned}$$

vanishes also automatically since $\partial v^l_{\langle t \rangle} / \partial n = 0$ is directly imposed as a boundary condition and $\partial v_{\langle n \rangle} / \partial t^l$ is zero since $v_{\langle n \rangle} = 0$ for the entire plane.

Finally, term T_2 in Eq. 2.32 reduces to:

$$\begin{aligned}
&\left[-q n_i + u_i v_{\langle n \rangle} + (\nu + \nu_t) \left(\frac{\partial u_i}{\partial x_j} + \frac{\partial u_j}{\partial x_i} \right) n_j \right] \frac{\partial v_i}{\partial \nu_{tp}} \\
&\qquad = \left[-q n_i + (\nu + \nu_t) \left(\frac{\partial u_i}{\partial x_j} + \frac{\partial u_j}{\partial x_i} \right) n_j \right] \frac{\partial v^l_{\langle t \rangle}}{\partial \nu_{tp}} t^l_i \\
&\qquad = (\nu + \nu_t) \left(\frac{\partial u_i}{\partial x_j} + \frac{\partial u_j}{\partial x_i} \right) n_j t^l_i \frac{\partial v^l_{\langle t \rangle}}{\partial \nu_{tp}} \\
&\qquad = (\nu + \nu_t) \left(\frac{\partial u_{\langle n \rangle}}{\partial t^l} + \frac{\partial u^l_{\langle t \rangle}}{\partial n} \right) \frac{\partial v^l_{\langle t \rangle}}{\partial \nu_{tp}} \\
&\qquad = (\nu + \nu_t) \frac{\partial u^l_{\langle t \rangle}}{\partial n} \frac{\partial v^l_{\langle t \rangle}}{\partial \nu_{tp}} = 0 \qquad (2.41)
\end{aligned}$$

To eliminate this term, the normal derivative of the tangential adjoint velocity components should be set $\partial u^l_{\langle t \rangle} / \partial n = 0$, thereby completing the adjoint velocity boundary conditions, which are consistent with those of the primal problem.

Similar to S_I and S_W, no boundary condition for q arises from the elimination of any of the boundary integrals in Eq. (2.32); therefore, a zero Neumann condition is imposed.

2.7 Sensitivity Derivatives Expression

By applying the ABC in Eq. (2.32), all surface integrals vanish and only term T_1 remains. The final expression for the SD takes the form:

$$\frac{\delta L}{\delta \nu_{tp}} = \frac{\delta J}{\delta \nu_{tp}} = \int_\Omega \frac{\partial u_i}{\partial x_j} \frac{\partial \nu_t}{\partial \nu_{tp}} \left(\frac{\partial v_i}{\partial x_j} + \frac{\partial v_j}{\partial x_i} \right) d\Omega \tag{2.42}$$

In a discrete setting, the sensitivity of the turbulent viscosity field ν_t evaluated at a position $\mathbf{x}_r$ w.r.t. the control variable ν_{tp} (defined at $\mathbf{x}_p$) is expressed via:

$$\frac{\partial \nu_t(\mathbf{x}_r)}{\partial \nu_{tp}} = \delta_{pr}, \quad \text{where} \quad \delta_{pr} = \begin{cases} 1 & \text{if} \quad p = r, \\ 0 & \text{otherwise.} \end{cases}$$

Thus, the sensitivity is nonzero only when the evaluation point coincides with the control point.

2.8 Adjoint Wall Functions

The previous sections referred to the solution of the continuous adjoint EVA problem for the case in which the primal RANS equations are solved without the use of wall functions, commonly referred to as the low-Reynolds-number (low-Re) model. Such an approach requires a highly refined mesh near solid boundaries in order to accurately resolve the viscous sublayer of a turbulent boundary layer. However, for complex 3D cases (e.g., flow around a car), this requirement becomes computationally prohibitive. Consequently, wall functions must be employed and their effect on the ABC in S_W should be assessed.

Wall functions in RANS

Within the `OpenFOAM` framework used for the implementation of the method, a unified wall-function formulation is available, capable of modeling both the viscous sublayer and the logarithmic region of the turbulent boundary layer. The employed relation is the Spalding wall-function [3]:

$$f_{WF} = y^+ - v^+ - e^{-\kappa B} \left[e^{\kappa v^+} - 1 - \kappa v^+ - \frac{(\kappa v^+)^2}{2} - \frac{(\kappa v^+)^3}{6} \right] = 0, \tag{2.43}$$

where $\kappa = 0.41$ is the von Kármán constant and $B = 5.5$. The dimensionless wall distance and velocity at the first cell center adjacent to the wall, denoted by P, are defined as $y_P^+ = \dfrac{\Delta^P v_\tau}{\nu}$, $v_P^+ = \dfrac{|\mathbf{v}^P|}{v_\tau}$ where Δ^P is the normal distance between the first near-wall cell center P and the corresponding boundary wall face f (see Fig. 2.2.

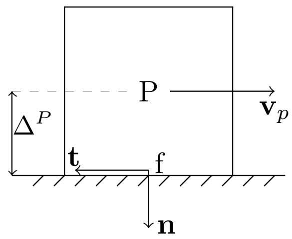

Figure 2.2: *First near wall cell.*

The friction velocity v_τ is computed from the wall shear stress according to:

$$v_\tau^2 = -\left[(\nu + \nu_t)\left(\frac{\partial v_i}{\partial x_j} + \frac{\partial v_j}{\partial x_i}\right)\right]^f n_j t_i^I \tag{2.44}$$

where n_j is the unit vector normal to the wall and t_i^I is the unit vector tangent to the wall and aligned with the velocity at P, which is assumed to be locally parallel to the wall surface.

The viscous flux at the wall boundary face f is calculated by

$$\begin{aligned} -\left[(\nu + \nu_t)\left(\frac{\partial v_i}{\partial x_j} + \frac{\partial v_j}{\partial x_i}\right)\right]^f n_j &\approx -\left[(\nu + \nu_t)\frac{\partial v_i}{\partial x_j}\right]^f n_j \\ &= -\left(\nu + \nu_t^f\right)\frac{v_i^f - v_i^P}{\Delta^P} \end{aligned} \tag{2.45}$$

where $v_i^f = 0$ due to the no-slip boundary condition and $\nu_t^f = 0$ since the turbulent viscosity vanishes over the wall boundary, owing to the damping of turbulent fluctuations in the viscous sublayer near solid walls [61]. However, such a formulation should not be considered reliable on coarse meshes, since differentiation in the wall-normal direction must be avoided. To overcome this inherent inconsistency in the gradient evaluation, in `OpenFOAM` an artificial value of $\nu_t^f \neq 0$ is introduced [62]. This auxiliary eddy viscosity is determined such that the wall shear stress obtained from Eq. (2.43) (i.e., the wall-function relationship) matches that computed from Eq. (2.45).

Consequently, the procedure consists of solving the nonlinear wall-function equation Eq. (2.43) $f_{WF}(v_\tau, |\mathbf{v}^P|, \Delta^P) = 0$, for the friction velocity v_τ using a Newton–Raphson iterative method. Once v_τ has been determined, Eq. (2.45) adjusts ν_t^f accordingly:

$$\nu_t^f \approx -\Delta^P \frac{v_\tau^2}{(v_i^f - v_i^P)t_i^I} - \nu = \Delta^P \frac{v_\tau^2}{v_i^P t_i^I} - \nu \tag{2.46}$$

Differentiation of the wall functions

The use of wall functions must also be taken into consideration in the formulation of the adjoint equations. From this point onward, the notation $\Delta \equiv \Delta^P$, $v^P = |\mathbf{v}^P|$ will be adopted. Since $f_{WF} = 0$, its variation also vanishes, i.e., $\delta f_{WF} = 0$, or equivalently:

$$\begin{aligned}
\delta f_{WF} &= \delta \left\{ \frac{\Delta v_\tau}{\nu} - v^+ - e^{-\kappa B} \left(e^{\kappa v^+} - 1 - \kappa v^+ - \frac{(\kappa v^+)^2}{2} - \frac{(\kappa v^+)^3}{6} \right) \right\} \\
&= \frac{v_\tau}{\nu}\delta\Delta + \frac{\Delta}{\nu}\delta v_\tau - \delta v^+ - e^{-\kappa B} \left(\kappa e^{\kappa v^+}\delta v^+ - \kappa\delta v^+ - \kappa^2 v^+ \delta v^+ - \frac{1}{2}\kappa^3 v^{+2}\delta v^+ \right) \\
&= \frac{v_\tau}{\nu}\delta\Delta + \frac{\Delta}{\nu}\delta v_\tau - \delta v^+ - \underbrace{\kappa e^{-\kappa B} \left(e^{\kappa v^+} - 1 - \kappa v^+ - \frac{1}{2}\kappa^2 v^{+2} \right)}_{A} \delta v^+ \\
&= \frac{v_\tau}{\nu}\delta\Delta + \frac{\Delta}{\nu}\delta v_\tau - (1+A)\delta v^+ = 0
\end{aligned} \tag{2.47}$$

The variation of v^+ is also calculated as:

$$\delta v^+ = \delta\left(\frac{v^P}{v_\tau}\right) = \frac{\delta v^P}{v_\tau} - \frac{v^P}{v_\tau^2}\delta v_\tau \tag{2.48}$$

Substituting Eq. (2.48) into Eq. (2.47) yields:

$$\begin{aligned}
\delta f_{WF} &= \frac{v_\tau}{\nu}\delta\Delta + \frac{\Delta}{\nu}\delta v_\tau - (1+A)\frac{\delta v^P}{v_\tau} + (1+A)\frac{v^P}{v_\tau^2}\delta v_\tau \\
&= \frac{v_\tau}{\nu}\delta\Delta + \left[\frac{\Delta}{\nu} + (1+A)\frac{v^P}{v_\tau^2}\right]\delta v_\tau - (1+A)\frac{\delta v^P}{v_\tau} = 0
\end{aligned} \tag{2.49}$$

and by rearranging the expression to solve for δv_τ:

$$\begin{aligned}
\delta v_\tau &= \frac{\dfrac{1+A}{v_\tau}}{\dfrac{\Delta}{\nu} + (1+A)\dfrac{v^P}{v_\tau^2}}\delta v^P - \frac{\dfrac{v_\tau}{\nu}}{\dfrac{\Delta}{\nu} + (1+A)\dfrac{v^P}{v_\tau^2}}\delta\Delta \\
&= \underbrace{\frac{1+A}{y^+ + (1+A)v^+}}_{-\mathbb{C}_v^{WF}}\delta v^P - \underbrace{\frac{1}{\nu}\frac{v_\tau^2}{y^+ + (1+A)v^+}}_{\mathbb{C}_\Delta^{WF}}\delta\Delta \\
&= -\mathbb{C}_v^{WF}\delta v^P - \mathbb{C}_\Delta^{WF}\delta\Delta
\end{aligned} \tag{2.50}$$

Influence of wall functions in T_4 of Eq. (2.32)

For the EVA problem, since $v_\tau^2 = \tau_{ij} n_j t_i^I$, the impact of the wall function in the adjoint formulation relates to the last term T_4 in Eq. (2.32). As stated in Sec. 2.6, for S_W, in order to eliminate term T_3 of Eq. (2.32), the boundary condition $u_{\langle n\rangle} = -W_2\kappa n_i r_i^{(D)}$ is imposed, leading to the remaining terms of T_4 as presented in Eq. (2.39):

$$\begin{aligned} T_4 &= -\int_{S_W} u^I_{\langle t\rangle} t^I_i n_j \frac{\partial \tau_{ij}}{\partial \nu_{tP}}\, dS - \int_{S_W} u^{II}_{\langle t\rangle} t^{II}_i n_j \frac{\partial \tau_{ij}}{\partial \nu_{tP}}\, dS \\ &= \int_{S_W} u^I_{\langle t\rangle} \frac{\partial v_\tau^2}{\partial \nu_{tP}}\, dS - \int_{S_W} u^{II}_{\langle t\rangle} \frac{\partial}{\partial \nu_{tP}} \left[(\nu+\nu_t)\left(\frac{\partial v_{\langle n\rangle}}{\partial t^{II}} + \frac{\partial v^{II}_{\langle t\rangle}}{\partial n}\right)\right] dS \end{aligned} \tag{2.51}$$

The second term on the right hand side is negleted by imposing $v^{II}_{\langle t\rangle} = 0$, thus leaving only the first one:

$$T_4 = \int_{S_W} u^I_{\langle t\rangle} \frac{\partial v_\tau^2}{\partial \nu_{tP}}\, dS = \int_{S_W} 2 v_\tau u^I_{\langle t\rangle} \frac{\partial v_\tau}{\partial \nu_{tP}}\, dS \tag{2.52}$$

Furthermore, since Δ does not vary w.r.t. ν_t, differentiating Eq. (2.50) results in:

$$\frac{\delta v_\tau}{\delta \nu_{tP}} = -\mathbb{C}_v^{WF} \frac{\partial v_P}{\nu_{tP}} \tag{2.53}$$

where v_P can be further developed as:

$$v^P = \sqrt{v_i^P v_i^P} \Rightarrow \frac{\partial v^P}{\partial \nu_{tP}} = \frac{2 v_i^P}{2\sqrt{v_j^P v_j^P}} \cdot \frac{\partial v_i^P}{\partial \nu_{tP}} = \frac{v_i^P}{v^P} \frac{\partial v_i^P}{\partial \nu_{tP}} \tag{2.54}$$

After inserting Eq. (2.52) into Eq. (2.53) and substituting the expression into Eq. (2.52), term T_4 in Eq. 2.32 becomes:

$$T_4 = \int_{S_W} \underbrace{-2 v_\tau u^I_{\langle t\rangle} \mathbb{C}_v^{WF} \frac{1}{v^P}}_{s_{wf}} \frac{\partial v_i^P}{\partial \nu_{tP}}\, dS \tag{2.55}$$

and s_{wf} is introduced as a source term in the adjoint momentum equations (Eq. (2.31b)) during the discretization of the first cell layer adjacent to the wall.

Influence of wall functions in T_2 of Eq. (2.32)

Using the wall functions formulation, T_2 of Eq. (2.32) cannot be neglected a priori, as, in contrast to Sec. 2.6, the wall velocity is nonzero and tangential to the wall boundary: $\mathbf{v} = v^I_{\langle t\rangle}\mathbf{t^I} \Rightarrow v_i = v^I_{\langle t\rangle} t^I_i$, leading to:

$$T_2 = \int_S \left[-q n_i + u_i v_{\langle n\rangle} + (\nu+\nu_t)\left(\frac{\partial u_i}{\partial x_j} + \frac{\partial u_j}{\partial x_i}\right) n_j\right] t^I_i \frac{v^I_{\langle t\rangle}}{\partial \nu_{tp}} dS$$

$$= \int_S \left[- q n_i t_i^I + u_i \left(-W_2 \kappa n_i r_i^{(D)} \right) t_i^I + \underbrace{(\nu + \nu_t) \left(\frac{\partial u_i}{\partial x_j} + \frac{\partial u_j}{\partial x_i} \right) n_j t_i^I}_{u_\tau^2} \right] \frac{v_{\langle t \rangle}^I}{\partial \nu_{tp}} dS \tag{2.56}$$

Since $n_i t_i^I = 0$ (i.e., $\mathbf{n} \cdot \mathbf{t^I} = \mathbf{0}$) the remaining term reads:

$$T_2 = \int_S u_\tau^2 \frac{v_{\langle t \rangle}^I}{\partial \nu_{tp}} dS \tag{2.57}$$

and for this to be eliminated $u_\tau = 0$ should be imposed.

2.9 Simulations in OpenFOAM

The simulations presented in the following chapters are performed using `OpenFOAM` (Open Field Operation and Manipulation), an open-source software framework written entirely in `C++`, widely used in CFD. Among its main advantages are its parallel computing capabilities and its integrated mesh-generation utilities, such as `blockMesh` and `snappyHexMesh`, both of which are employed in the present work.

The governing flow equations are discretized using the Finite Volume Method, where the solution variables are stored at the centroids of the computational cells. Steady-state RANS simulations are solved using the SIMPLE algorithm [63], whereas the DES (which will be used for H-Fi data generation in the 3D cases) are performed using the PIMPLE algorithm, a hybrid SIMPLE–PISO method [64].

For the EVA simulations, equations (2.3) and (2.31) are discretized and solved on unstructured, collocated, cell-centered finite-volume meshes. Convective terms are approximated using second-order upwind schemes, while diffusive fluxes are discretized using central differencing with non-orthogonality corrections. Spatial gradients are evaluated using the Gauss divergence theorem together with linear interpolation of field quantities from cell centers to cell faces.

For the purposes of this thesis, the in-house `EVA Library`, originally developed by [36], has been further extended. In particular, the loss functions defined in Eqs. (2.11) and (2.15) were incorporated, together with their corresponding contributions to the FAE and ABC. Furthermore, the wall treatment of the adjoint equations was refined to account consistently for both low-Reynolds and wall-function-based RANS formulations. Finally, additional surrogate algebraic turbulence models (the outputs of SR routines, provided by [53]), were implemented along with their differentiation within the adjoint equations for ShpO.

All simulations were performed on the Velos CPU cluster of the *PCOpt* Unit at NTUA, using 48–64 Intel Xeon E5-2630 v4 processors operating at 2.2 GHz.

Chapter 3

Velocity-based EVA for 2D Periodic Hills

The first case presented in this thesis concerns the flow over 2D periodic hills [55], a classical benchmark problem for turbulence model verification [65], used here to assess the effectiveness of the proposed EVA methodology. In the following sections, the problem formulation is presented and different velocity-related EVA loss functions are investigated in order to identify the most suitable formulation for accurately capturing the Hi-Fi data through the solution of the RANS equations without the use of a turbulence model.

3.1 Case Definition

The 2D periodic hills case is essentially a channel flow between two flat plates of streamwise length L_x, where polynomial-shaped obstacles of height H are mounted on the bottom one, as shown in Fig. 3.1. The resulting flow configuration generates a large recirculation region in the wake of the hills, which is particularly challenging to predict accurately.

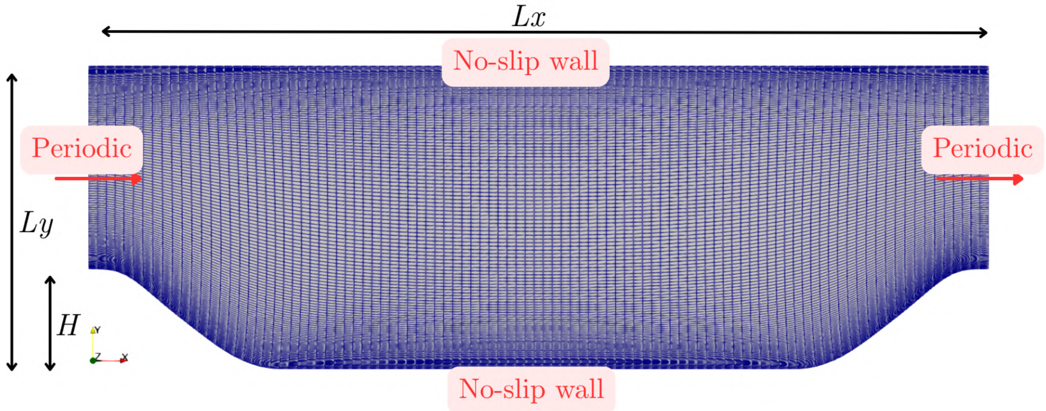

Figure 3.1: *Computational domain for the baseline periodic hills geometry (steepness factor $a = 1.0$).*

The geometry of a hill, is represented using piecewise third-order polynomial functions [66]:

$$\hat{y} = \begin{cases} \min(1; 1 + 2.42 \cdot 10^{-4}\hat{x}^2 - 7.588 \cdot 10^{-5}\hat{x}^3), & \hat{x} \in [0, 0.3214] \\ 0.8955 + 3.484 \cdot 10^{-2}\hat{x} - 3.629 \cdot 10^{-3}\hat{x}^2 + 6.749 \cdot 10^{-5}\hat{x}^3, & \hat{x} \in (0.3214, 0.5] \\ 0.9213 + 2.931 \cdot 10^{-2}\hat{x} - 3.234 \cdot 10^{-3}\hat{x}^2 + 5.809 \cdot 10^{-5}\hat{x}^3, & \hat{x} \in (0.5, 0.7143] \\ 1.445 - 4.927 \cdot 10^{-2}\hat{x} + 6.95 \cdot 10^{-4}\hat{x}^2 - 7.394 \cdot 10^{-6}\hat{x}^3, & \hat{x} \in (0.7143, 1.071] \\ 0.6401 + 3.123 \cdot 10^{-2}\hat{x} - 1.988 \cdot 10^{-3}\hat{x}^2 + 2.242 \cdot 10^{-5}\hat{x}^3, & \hat{x} \in (1.071, 1.429] \\ \max(0; 2.0139 - 7.18 \cdot 10^{-2}\hat{x} + 5.875 \cdot 10^{-4}\hat{x}^2 + 9.553 \cdot 10^{-7}\hat{x}^3), & \hat{x} \in (1.429, 1.929] \end{cases}$$

where $\hat{x} = x/H$ and $\hat{y} = y/H$ are normalized horizontal and vertical coordinates, respectively, and $x \in [0, 1.929H]$.

The channel height is defined as $L_y = 3.035H$, while the horizontal length can be parameterized as $L_x = (3.858a + 5.142)H$. In this way, by increasing a while keeping H constant, L_x increases, whereas the horizontal part of the lower wall $(5.142H)$ remains unchanged, resulting consequently in a decrease in the hill steepness.

The reference case which is presented in Fig. 3.1 corresponds to $a = 1$, resulting in a crest-to-crest distance of $L_x = 9H$. Periodic boundary conditions are applied in the streamwise direction, and non-slip boundary conditions are applied at the walls, while the flow is driven by a constant body force implemented as a uniform forcing term in the x-momentum equation to ensure constant bulk Reynolds number and bulk velocity at the crest [67, 68], defined as:

$$Re = \frac{v_b H}{\nu}, \qquad v_b = \frac{1}{2.035H} \int_H^{3.035H} v_x(y)\big|_{x=0}\, dy \tag{3.1}$$

In the following sections, simulations are performed for $Re = 5600$, with $H = 1$ and $\nu = 5 \cdot 10^{-6}$ m^2/s, resulting in a bulk velocity of $v_b = 0.028$ m/s (which is maintained constant through the application of the appropriate body force). Furthermore, five different geometries are generated by varying the so-called steepness-ratio parameter a, as shown in Fig. 3.2.

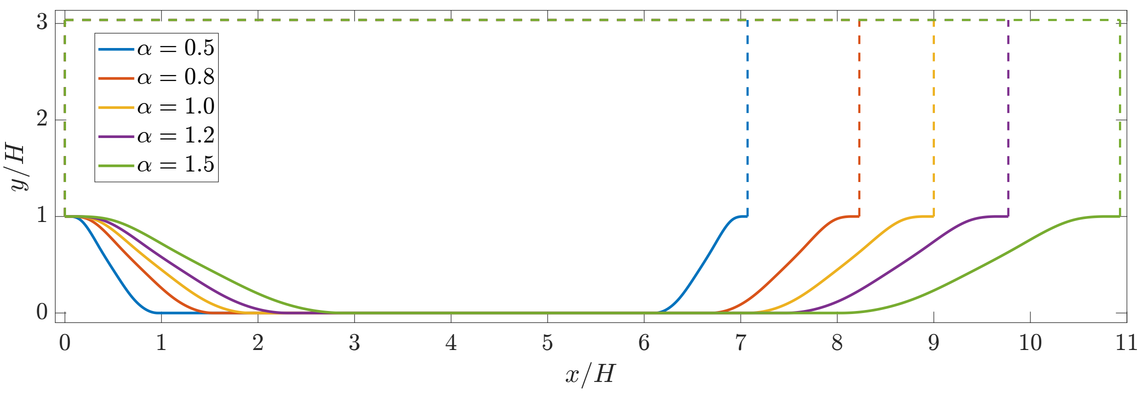

Figure 3.2: *Parametrized periodic hills for varying channel widths.*

In this work, the reference flow fields (Hi-Fi data for the EVA process) have been obtained from a 3D DNS database reported in [66] and interpolated onto coarser 2D meshes, comprising approximately $14.7k$ cells (the $a = 1.0$ configuration is illustrated in Fig. 3.1). All meshes are characterized by a maximum dimensionless wall distance of $y^+ < 0.9$ at both the upper and lower walls, thereby obviating the need for wall functions.

3.2 EVA for the Baseline Geometry Using Different Loss Functions

The first step in the application of the EVA framework, as illustrated in Fig. 1.3, is to obtain a baseline flowfield solution $(\mathbf{v}, p, \nu_t)$ by solving the RANS equations with a conventional turbulence model (e.g., k–ϵ, SA). This baseline solution subsequently serves as the initialization for the EVA process. Proper initialization is critical; without a physically realistic distribution of the eddy viscosity ν_t, the primal problem fails to converge, because during a RANS/rEV run, ν_t within each cell remains constant and is updated only after the adjoint problem is solved.

In this study, the k–ϵ and SA turbulence models are employed for initialization purposes, their boundary conditions are detailed in Tab. 3.1. The corresponding converged streamwise velocity contours, together with the associated flow streamlines, are presented in Fig. 3.3. The reference Hi-Fi time-averaged DNS solution exhibits a prominent reverse-flow region downstream of the hill, as shown in Fig. 3.3a. In contrast, the RANS/k–ϵ simulation underpredicts the size of the separation bubble (Fig. 3.3b), while the RANS/SA one clearly overpredicts it (Fig. 3.3c). Contours of the magnitude of the velocity difference between the Low- and Hi-Fi solutions are presented in Fig. 3.4.

Table 3.1: *Boundary conditions for the periodic hills simulations.*

Variable	Inlet	Outlet	Walls
$\mathbf{v}$	periodic	periodic	no-slip
p	periodic	periodic	zero Neumann
ν_t	periodic	periodic	zero Dirichlet
$\tilde{\nu}$ (for SA)	periodic	periodic	zero Dirichlet
k (for k–ϵ)	periodic	periodic	zero Dirichlet
ϵ (for k–ϵ)	periodic	periodic	zero Dirichlet
$\mathbf{u}$	periodic	periodic	(0,0)
q	periodic	periodic	zero Neumann

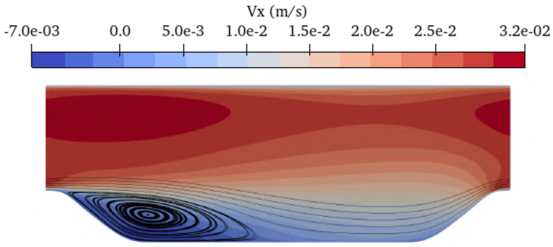

(a) *DNS (Hi-Fi)*

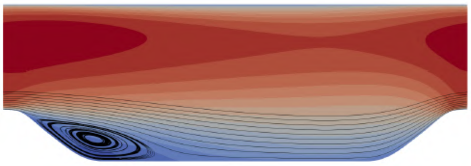

(b) *RANS/k-ϵ*

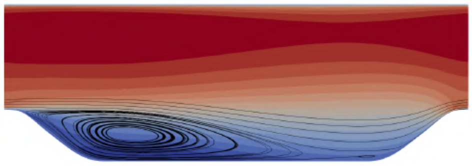

(c) *RANS/SA*

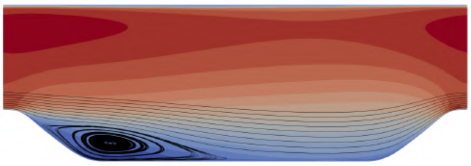

(d) *RANS/rEV, J_1 from* (3.2) *(init. SA)*

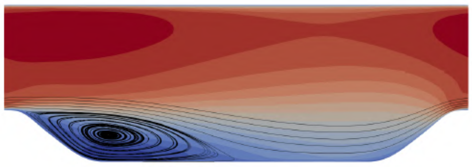

(e) *RANS/rEV, J_2 from* (3.3) *(init. k-ϵ)*

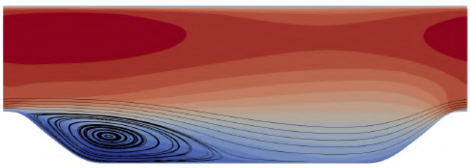

(f) *RANS/rEV, J_2 from* (3.3) *(init. SA)*

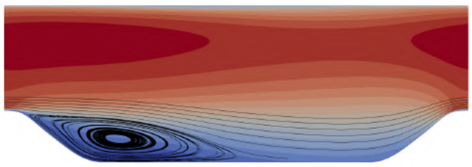

(g) *RANS/rEV, J_3 from* (3.4) *(init. SA)*

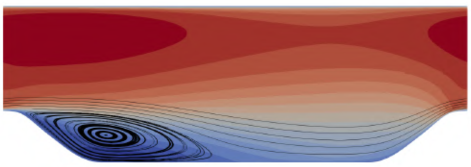

(h) *RANS/rEV, J_4 from* (3.5) *(init. k-ϵ)*

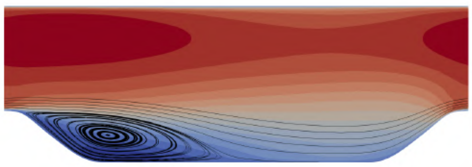

(i) *RANS/rEV, J_4 from* (3.5) *(init. SA)*

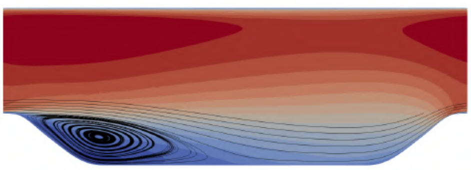

(j) *RANS/rEV, J_5 from* (3.6) *(init. k-ϵ)*

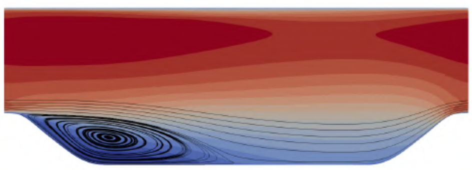

(k) *RANS/rEV, J_5 from* (3.6) *(init. SA)*

Figure 3.3: *Periodic hills $a = 1.0$. Streamwise velocity contours and streamlines for different turbulence models and loss functions J.*

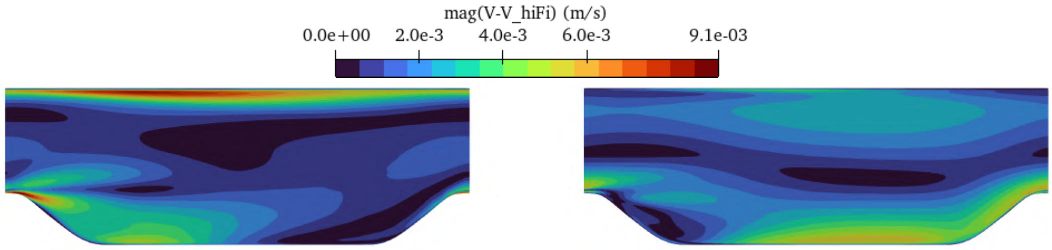

(a) *RANS/k-ϵ and DNS* **(b)** *RANS/SA and DNS*

Figure 3.4: *Periodic hills $a = 1.0$. Contours of $\left|v_i - v_{i,hi\text{-}fi}\right|$ for different RANS turbulence models.*

The EVA process is carried out utilizing the following velocity-based loss functions, analogous to Eq. (2.11):

1. One restricted to specific regions of the computational domain:

$$J_1 = \frac{1}{2}\int_{\Omega_1} \left(v_i - v_{i,\text{hi-fi}}\right)^2 d\Omega \tag{3.2}$$

where Ω_1 comprises 60 selected mesh cells; half of them are those with the largest v_i discrepancy between the RANS/SA and DNS results, as shown in Fig. 3.4b, while the remaining cells are selected randomly from the whole domain. The complete set of cells defining Ω_1 is illustrated in Fig. 3.7a.

Using the converged RANS/SA solution for initialization, the residual histories of the primal and adjoint problems during the first EVA cycle are shown in Fig. 3.5. In total, 200 EVA cycles were performed, with the design variables updated via the Method of Moving Asymptotes (MMA) [69, 70]. The resulting streamwise velocity field over the entire computational domain is presented in Fig. 3.3d. Compared to the baseline RANS/SA prediction, the EVA RANS/rEV solution is noticeably closer to the DNS reference, particularly in the separated-flow region downstream of the hill. In this case, the loss function J_1 is reduced by 66.4%.

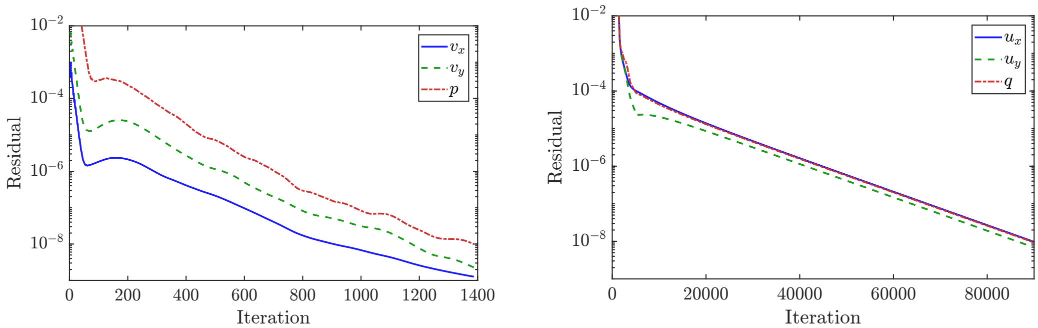

Figure 3.5: *Periodic hills $a = 1.0$. Convergence history for the primal (left) and adjoint (right) EVA problem for the first optimization cycle; loss function is given by Eq. (3.2).*

2. Another loss function considered is defined as:

$$J_2 = \frac{1}{2} \int_{\Omega} \left(v_i - v_{i,\text{hi-fi}}\right)^2 \, d\Omega \tag{3.3}$$

   and in contrast to Eq. (3.2), the functional is evaluated over the entire computational domain Ω, rather than in selected cells (basically $w_p = 1$ over the whole domain).

   Using either the RANS/k–ϵ or the RANS/SA solution as a starting point for a total of 200 EVA cycles (the corresponding convergence histories are illustrated in Fig. 3.6), the results are the following: the RANS/k–ϵ initialization yiels a 95.0% reduction in the loss function J_2, while the RANS/SA achieves a 94.5% one. It should be noted, however, that the RANS/k–ϵ model exhibits a larger initial deviation from the DNS reference solution, as shown in Fig. 3.4. The resulting EVA fields, depicted in Fig. 3.3e and Fig. 3.3f, are extremely close to the Hi-Fi data for both the velocity contours and the streamlines within the recirculation region. This demonstrates that EVA can deliver exceptional results independently of the initialization used.

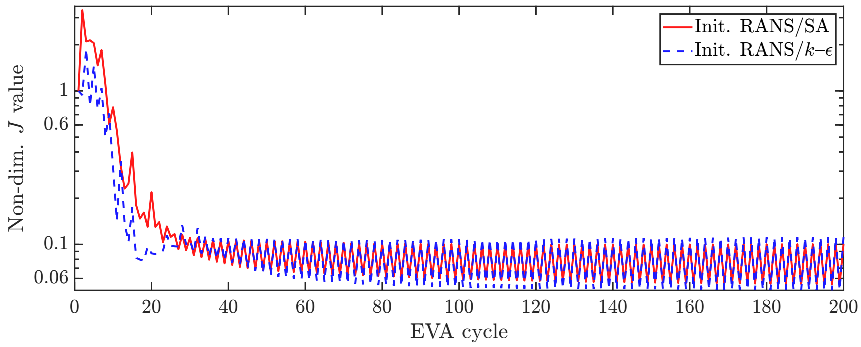

Figure 3.6: *Periodic hills $a = 1.0$. Convergence of the EVA method for different initializations; loss function is given by Eq.* (3.3).

   Particularly noteworthy are the contours of the correction field $\beta = \nu_t$, presented in Fig. 3.8. The initial ν_t fields, obtained from the classical turbulence models (Figs. 3.8a and 3.8b) differ substantially, as expected, since they employ different transport equations for the computation of ν_t. However, the corresponding EVA-derived fields (Figs. 3.8c and 3.8d) exhibit remarkably similar patterns, particularly in the near-wall regions where turbulence production is more intense. Although differences remain visible in the channel core, away from the walls, their impact on the overall flowfield is negligible, as this region was already accurately captured by the baseline RANS models.

3. A key limitation of the loss function defined in Eq. (3.3) is that the squared velocity difference between the Low- and Hi-Fi solvers is typically very small in the near-wall region, as illustrated in Fig. 3.4. However, accurately resolving the flow within the boundary layer is of critical importance, particularly

in situations where one solver predicts a positive near-wall velocity gradient, $\partial v_x/\partial y$, while the other predicts a negative one. In such cases, the loss function may fail to adequately penalize physically significant discrepancies due to their potentially small absolute magnitude. To address this and properly weight the near-wall discrepancies, the following alternative loss function is proposed:

$$J_3 = \frac{1}{2}\int_\Omega \underbrace{\Delta_p}_{w_p} \cdot (v_i - v_{i,\text{hi-fi}})^2 \, d\Omega \tag{3.4}$$

where Δ_p represents the distance of cell p from the nearest wall boundary. The resulting spatial distribution of the weighting field is shown in Fig. 3.7b. As in the preceding cases, EVA is carried out for 200 cycles using the MMA update method (RANS/SA solution is used as initial condition) leading to a reduction of the J_4 value by 81.7%. As shown in Fig. 3.3g, the resulting velocity field exhibits substantially improved agreement with the DNS solution compared with the baseline RANS/SA prediction. Nevertheless, when compared with the solution obtained using the J_3 loss function (Fig. 3.3f), a slightly larger recirculation region is predicted, indicating a somewhat reduced accuracy in capturing the extent of flow separation. This behavior is consistent with the definition of J_3, which places limited weighting on cells away from the wall, even in regions where velocity differences associated with recirculation can be significant.

4. A loss function, which is examined next, is:

$$J_4 = \frac{1}{2}\int_\Omega \underbrace{\frac{1}{(v_{i,\text{hi-fi}})^2}}_{w_p} \cdot (v_i - v_{i,\text{hi-fi}})^2 \, d\Omega \tag{3.5}$$

Similar to Eq. (3.4), J_4 assigns higher weights near the wall, where $|v_{i,\text{hi-fi}}|$ is naturally small. Furthermore, by normalizing the squared velocity difference by $(v_{i,\text{hi-fi}})^2$, J_4 effectively measures the local squared relative error between the Low- and Hi-Fi velocity fields. The corresponding w_p field is shown in Fig. 3.7c. The EVA process yields a 97.1% reduction in the loss function value for the RANS/k–ϵ initialization, and a 96.7% reduction for the RANS/SA one. The respective velocity contours are shown in Fig. 3.3h and Fig. 3.3i, accurately capturing the extent of the recirculation region.

5. Finally, a combination of Eqs. (3.4) and (3.5) is proposed:

$$J_5 = \frac{1}{2}\int_\Omega \underbrace{\frac{\Delta_p}{(v_{i,\text{hi-fi}})^2}}_{w_p} \cdot (v_i - v_{i,\text{hi-fi}})^2 \, d\Omega \tag{3.6}$$

accounting both the distance from wall boundaries and the velocity magnitude of the Hi-Fi solution in each cell, resulting in the weighting field w_p in Fig. 3.7d. In this case, EVA reduces the J_5 value by 95.0% for the RANS/k–ϵ initialization and by 93.3% for the RANS/SA. The resulting RANS/rEV velocity fields are observed in Figs. 3.3j and 3.3k, and, as in the previous cases, they satisfactorily capture the extent of the recirculation region. The ν_t fields corresponding to the converged EVA solutions are presented in Figs. 3.8e and 3.8f, respectively.

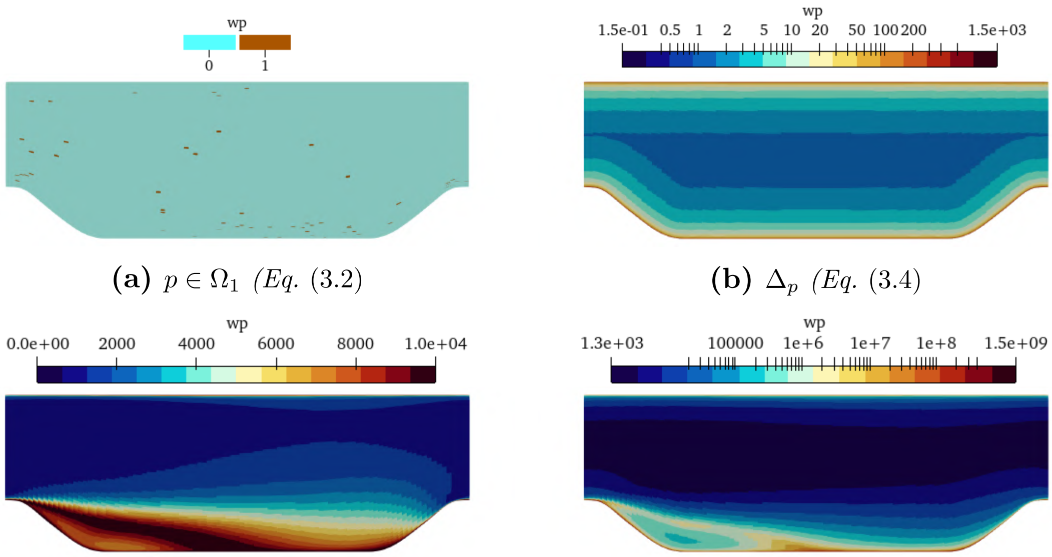

(a) $p \in \Omega_1$ *(Eq.* (3.2)

(b) Δ_p *(Eq.* (3.4)

(c) $(1/v_{i,hi\text{-}fi})^2$ *(Eq.* (3.5)

(d) $\Delta_p/v^2_{i,hi\text{-}fi}$ *(Eq.* (3.6)*)*

Figure 3.7: *Periodic hills* $a = 1.0$. *Contours of different weighting factors* w_p.

In addition to accurately restructuring the velocity field (Fig. 3.3), a successful EVA process must also provide reliable predictions of wall-bounded quantities. This is particularly important for ShpO applications, where the objective is often directly related to surface integral quantities (e.g., drag force reduction, lift enhancement). Consequently, the skin-friction coefficient, C_f, should also be accurately predicted as this is a quantity directly related to the local velocity gradients at the wall:

$$C_f = \frac{\tau_w}{\frac{1}{2}v_b^2} = \frac{(\nu + \cancel{\nu_t})\left(\frac{\partial v_i}{\partial x_j} + \frac{\partial v_j}{\partial x_i}\right) t_i n_j \Big|_{\text{wall}}}{\frac{1}{2}v_b^2} = \frac{2\nu}{v_b^2}\left(\frac{\partial v_i}{\partial x_j} + \frac{\partial v_j}{\partial x_i}\right) t_i n_j \Big|_{\text{wall}} \tag{3.7}$$

where v_b denotes the reference velocity, which in the present case corresponds to the bulk velocity at the hill crest, defined in Eq. (3.1).

The C_f distributions, for all cases considered in this section, where RANS/SA solution serves as the EVA initialization, are presented in Fig. 3.9. It is evident that the initial RANS/SA prediction differs significantly from the DNS reference, particularly regarding the reattachment point, identified by the position

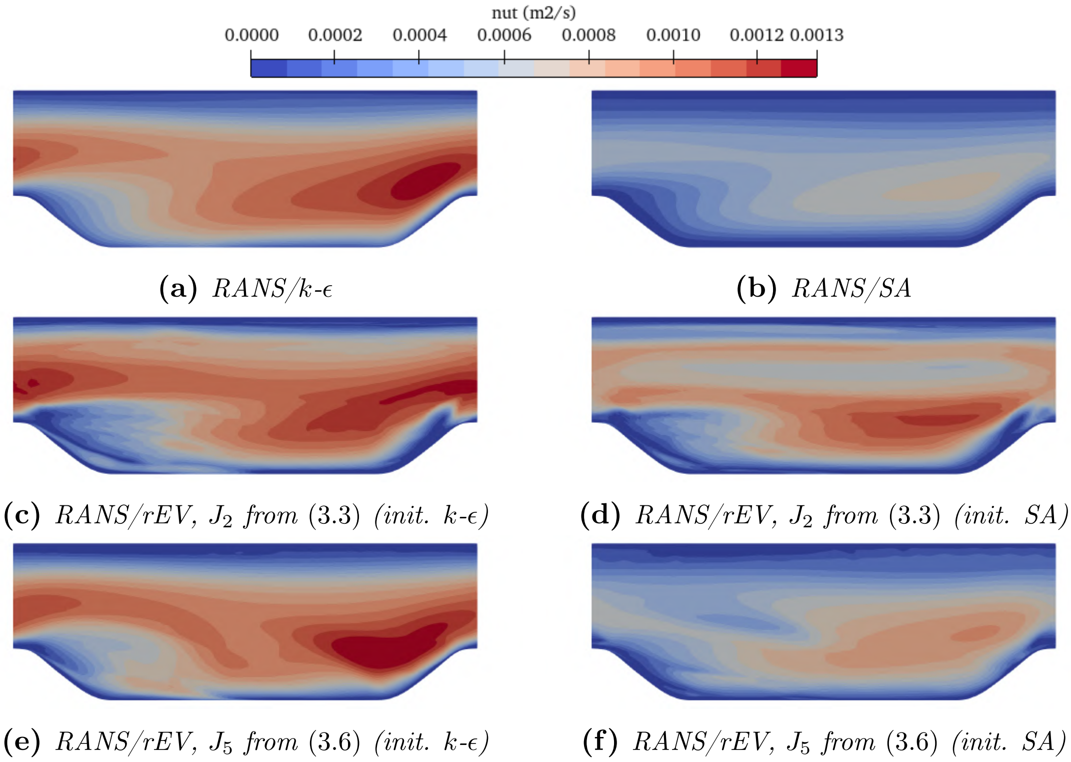

(a) *RANS/k-ϵ*

(b) *RANS/SA*

(c) *RANS/rEV, J_2 from (3.3) (init. k-ϵ)*

(d) *RANS/rEV, J_2 from (3.3) (init. SA)*

(e) *RANS/rEV, J_5 from (3.6) (init. k-ϵ)*

(f) *RANS/rEV, J_5 from (3.6) (init. SA)*

Figure 3.8: *Periodic hills $a = 1.0$. Eddy viscosity contours for different turbulence models.*

at which C_f becomes positive, downstream of the recirculation region. Specifically, the RANS/SA solution substantially overpredicts the reattachment point, yielding $x/H = 7.75$ compared to $x/H = 5.04$ for DNS. Furthermore, although the RANS/SA model correctly predicts the location of the max C_f value as the flow accelerates over the downstream hill, it underpredicts its magnitude.

In comparison, the EVA solution obtained using J_1 shifts the reattachment point closer to the DNS prediction, yielding $x/H = 6.20$. It also improves the prediction of the C_f distribution downstream of reattachment. However, the agreement within the recirculation region ($C_f < 0$) deteriorates. This behavior is expected, since, as shown in Fig. 3.7a, no near-wall cells are included in the evaluation of the loss function. Furthermore, the loss functions J_2 and J_4, for which the weights are either uniform ($w_p = 1$) or dependent on $v_{i,\text{hi-fi}}$, respectively, provide an excellent prediction of the reattachment location, at $x/H = 5.21$ and $x/H = 5.02$. Nevertheless, both cases significantly overpredict the maximum value of C_f and underpredict its negative values within the recirculation region. In contrast, J_3, whose weighting depends solely on the wall distance, captures the overall DNS C_f distribution more accurately, but predicts the reattachment point at $x/H = 5.76$, indicating an overestimation of the recirculation region. Lastly, compared to the other formulations, J_5 yields the most comprehensive agreement with the reference data. It provides a highly satisfactory prediction of the reattachment point ($x/H = 4.75$), only slightly less accurate than J_2 and J_4, while also reproducing the Hi-Fi C_f distribution with good agreement. This improved performance can be attributed to the combined effect of velocity normalization and wall-distance weighting in its definition.

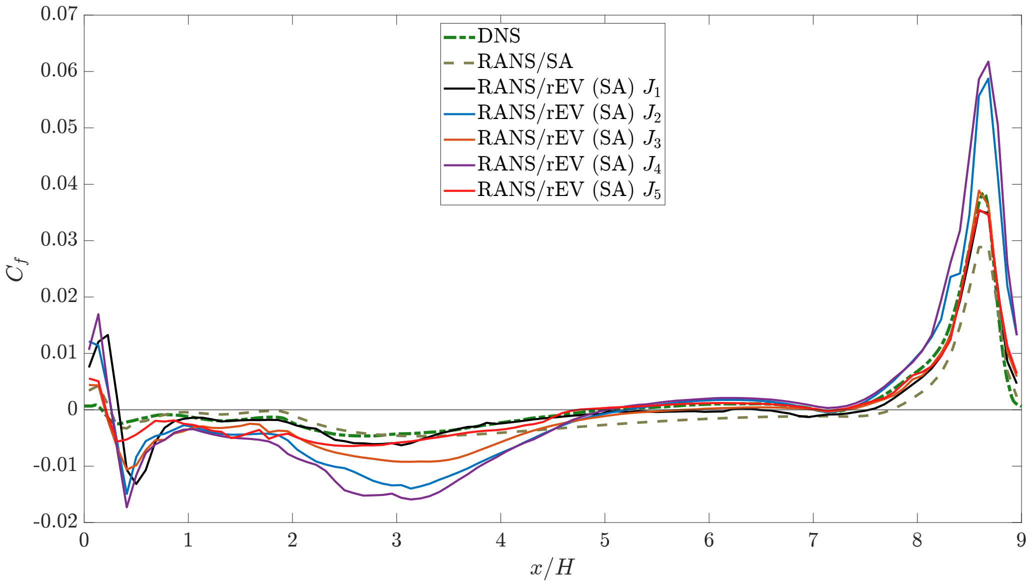

Figure 3.9: *Periodic hills $a = 1.0$. Comparison of skin friction coefficient C_f across the lower wall for different EVA loss functions with RANS/SA used for initialization. The DNS data are provided by [71].*

Finally, for the k–ϵ initialization, the C_f distributions of the EVA simulations are shown in Fig. 3.10. The baseline RANS/k–ϵ solution differs significantly from the DNS reference, underpredicting the reattachment location ($x/H = 3.20$ compared to $x/H = 5.04$ for the Hi-Fi data), overpredicting the initial separation point ($x/H = 0.48$ instead of 0.17), and generally overestimating the magnitude of C_f throughout the domain. The EVA results show a substantial improvement, with J_5 once again providing the best overall shape of the distribution, while J_2 yielding the most accurate prediction of the reattachment point position ($x/H = 5.07$).

All examined cases are summarized in Tab. 3.2. For each case, the loss function J_2 (Eq. (3.3)), representing the squared velocity deviation between the Low and Hi-Fi fields, is also evaluated to measure the global correction achieved across the solution field. The largest reductions in J_2 occur when the optimization is driven by J_2 or J_4 (exceeding 90%), followed by J_5 (approximately 80%), whereas J_3 and J_1 yield the smallest improvements. This trend is also reflected in the accuracy of the reattachment point predictions. In contrast, for the separation point, J_3 and J_5 show the closest agreement with the reference data.

In summary, the choice between J_2 (or J_4) and J_5 depends on the specific application: the former delivers superior velocity contour predictions, while the latter ensures better fidelity in surface-field quantities. Finally, Fig. 3.11 presents the v_x and v_y velocity profiles at selected vertical positions within the domain. The

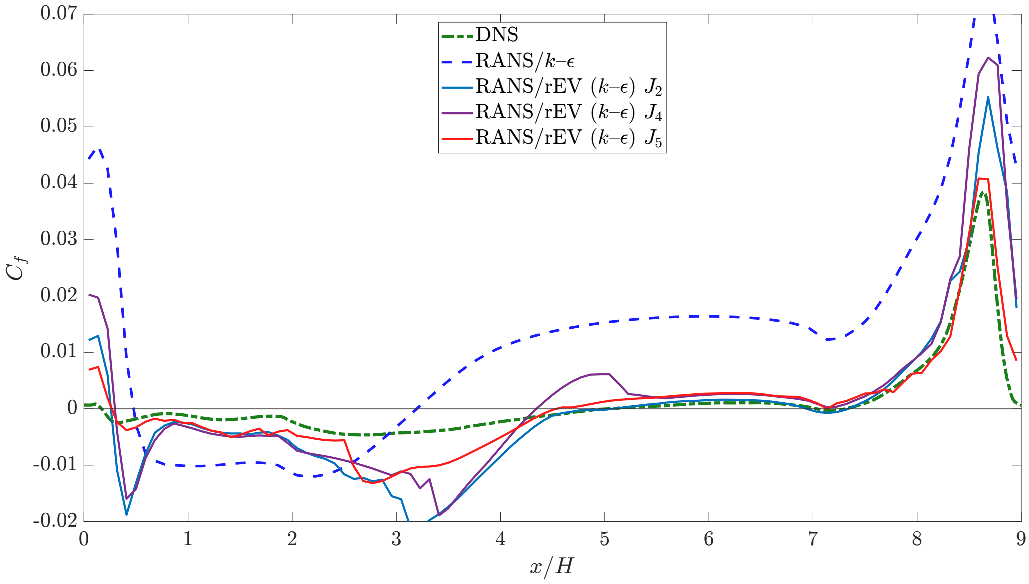

Figure 3.10: *Periodic hills $a = 1.0$. Comparison of skin friction coefficient C_f across the lower wall for different EVA loss functions with RANS/k–ϵ used for initialization. The DNS data are provided by [71].*

Table 3.2: *Periodic hills $a = 1.0$. EVA results using different loss functions J.*

Loss function J_i	**Initialization turbulence model**	J_i **reduction (%)**	J_2 **reduction (%)**	**Separat. / Reattach. point in bottom wall (x/H)**
DNS				**0.17 / 5.04**
RANS/k–ϵ				0.48 / 3.20
RANS/SA				0.25 / 7.75
J_1, Eq. (3.2)	SA	66.4%	32.0%	0.33 / 6.20
J_2, Eq. (3.3)	k–ϵ	95.0%	95.0%	0.26 / 5.07
J_2, Eq. (3.3)	SA	94.5%	94.5%	0.26 / 5.21
J_3, Eq. (3.4)	SA	81.7%	58.1%	0.20 / 5.76
J_4, Eq. (3.5)	k–ϵ	97.1%	95.1%	0.30 / 4.34
J_4, Eq. (3.5)	SA	96.7%	92.6%	0.26 / 5.02
J_5, Eq. (3.6)	k–ϵ	95.0%	83.6%	0.27 /4.54
J_5, Eq. (3.6)	SA	93.3%	72.7%	0.21 / 4.75

EVA simulations, with J_2 being used as the objective, showcase excellent results that closely capture the DNS data. Notably, the method successfully corrects the velocity gradients within the bottom-wall boundary layer compared to classical turbulence models. For example, at $x/H = 5$, it reverses the negative velocity trend predicted by the SA model, while at $x/H = 4$, it corrects the positive v_x observed in the k–ϵ model.

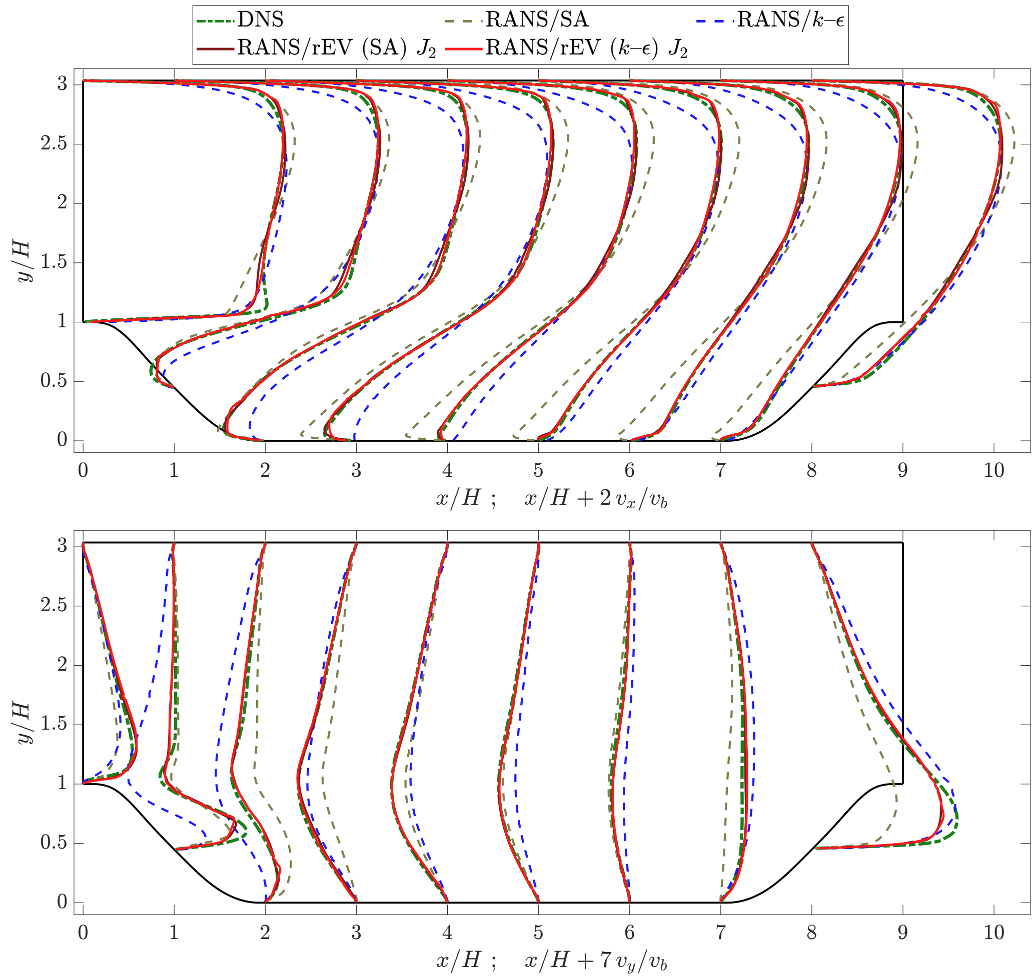

Figure 3.11: *Periodic hills $a = 1.0$. Mean velocity profiles in the streamwise (top) and vertical (bottom) directions for different flowfield solvers.*

3.3 Cumulative EVA Results for All Geometries

Using J_2 (Eq. (3.3)) as the loss function, EVA is applied to all alternative geometries, generated by varying the hill steepness ratio a (see Fig. 3.2). The EVA results, using RANS/k–ϵ solution as initialization, are summarized in Tab. 3.3 and compared with the Low- and Hi-Fi solutions.

For all cases, the RANS/rEV approach provides improved predictions of the separation and reattachment points along the bottom wall compared to the

Table 3.3: *EVA results (using J_2) for different steepest ratio a values.*

Case	Simulation Type	Loss function reduction (%)	Separat. / Reattach. point in bottom wall (x/H)
	DNS		**0.04 / 6.57**
$a = 0.5$	RANS/k–ϵ		0.21 / 3.18
	RANS/rEV (init. k–ϵ)	71.6%	0.16 / 4.28
	DNS		**0.15 / 5.21**
$a = 0.8$	RANS/k–ϵ		0.36 / 3.15
	RANS/rEV (init. k–ϵ)	75.0%	0.25 / 4.30
	DNS		**0.17 / 5.04**
$a = 1.0$	RANS/k–ϵ		0.48 / 3.20
	RANS/rEV (init. k–ϵ)	95.0%	0.26 / 5.07
	DNS		**0.31 / 4.50**
$a = 1.2$	RANS/k–ϵ		0.61 / 3.29
	RANS/rEV (init. k–ϵ)	93.8%	0.39 / 4.35
	DNS		**0.48 / 4.10**
$a = 1.5$	RANS/k–ϵ		0.85 / 3.45
	RANS/rEV (init. k–ϵ)	78.9%	0.42 / 4.21

RANS/k–ϵ model, leading to a more accurate estimation of the recirculation bubble size. Furthermore, the J_2 loss function decreases by more than 70% after 200 EVA cycles in all cases, with the most pronounced reduction observed for intermediate steepness values ($a = 1.0$ and $a = 1.2$). These trends are also evident in the v_x contours (Figs. 3.12, 3.15, 3.18, 3.21) and in the v_x and v_y velocity profiles (Figs. 3.13, 3.16, 3.19, 3.22) for $a = 0.5$, 0.8, 1.2, and 1.5, respectively. In all cases, the RANS/k–ϵ model underpredicts the extent of the recirculation zone, while RANS/SA overpredicts it, except for $a = 0.5$, where it is in close agreement with the DNS results. The EVA solution consistently approaches the DNS reference, while also yielding corrected v_x contour structures. Finally, Figs. 3.14, 3.17, 3.20, and 3.23 show the correction fields $\beta = \nu_t$ obtained from the procedure. In all cases, it is noticeable that ν_t is enhanced in the vicinity of the recirculation zone.

Results for a=0.5

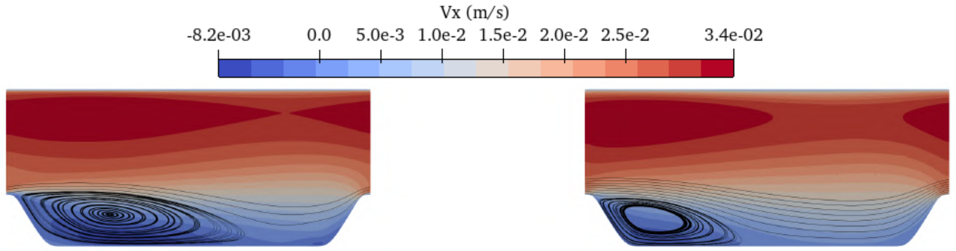

(a) *DNS (Hi-Fi)* **(b)** *RANS/k-ϵ*

(c) *RANS/SA* **(d)** *RANS/rEV, J_2 from* (3.3) *(init. k-ϵ)*

Figure 3.12: *Periodic hills $a = 0.5$. Streamwise velocity contours and streamlines for different flowfield solvers.*

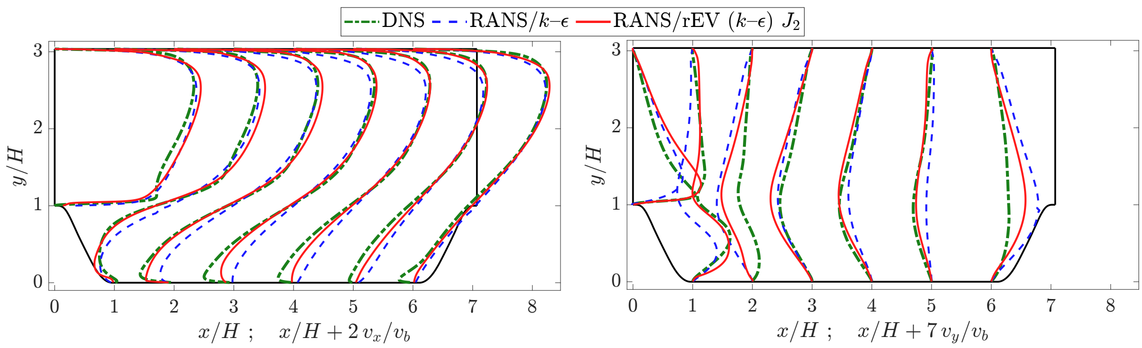

Figure 3.13: *Periodic hills $a = 0.5$. Mean velocity profiles in the streamwise (left) and vertical (right) directions for different flowfield solvers.*

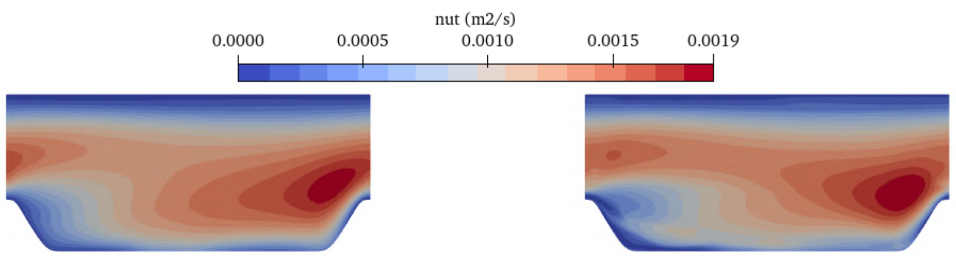

(a) *RANS/k-ϵ* **(b)** *RANS/rEV, J_2 from* (3.3) *(init. k-ϵ)*

Figure 3.14: *Periodic hills $a = 0.5$. Eddy viscosity contours for different turbulence models.*

Results for a=0.8

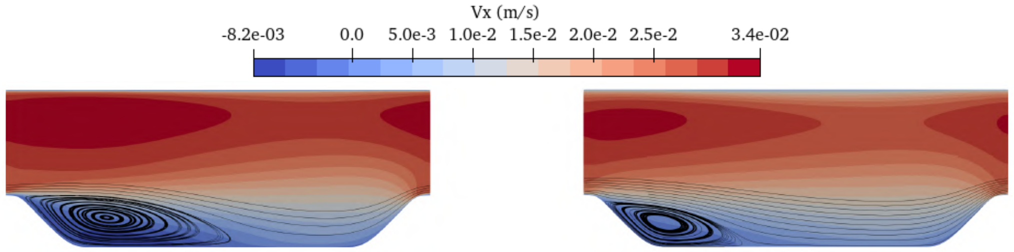

(a) *DNS (Hi-Fi)* (b) *RANS/k-ϵ*

(c) *RANS/SA* (d) *RANS/rEV, J_2 from* (3.3) *(init. k-ϵ)*

Figure 3.15: *Periodic hills $a = 0.8$. Streamwise velocity contours and streamlines for different flowfield solvers.*

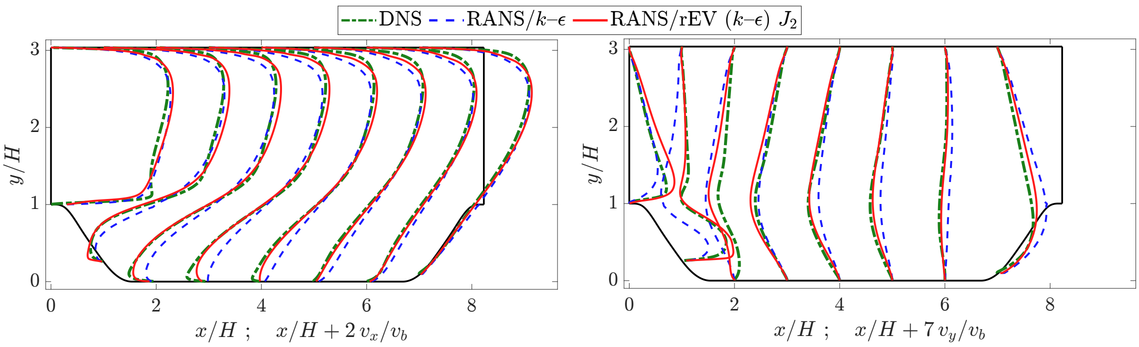

Figure 3.16: *Periodic hills $a = 0.8$. Mean velocity profiles in the streamwise (left) and vertical (right) directions for different flowfield solvers.*

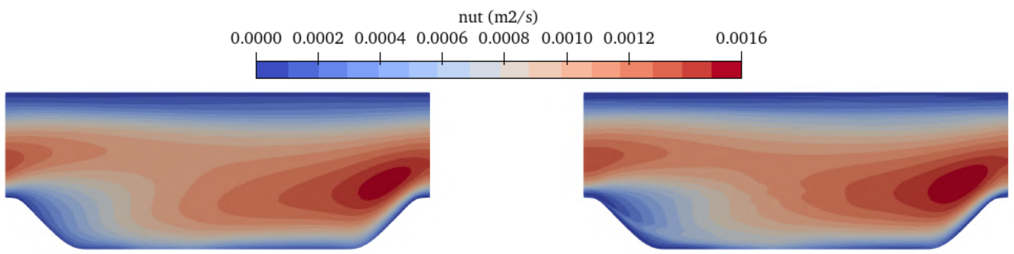

(a) *RANS/k-ϵ* (b) *RANS/rEV, J_2 from* (3.3) *(init. k-ϵ)*

Figure 3.17: *Periodic hills $a = 0.8$. Eddy viscosity contours for different turbulence models.*

Results for a=1.2

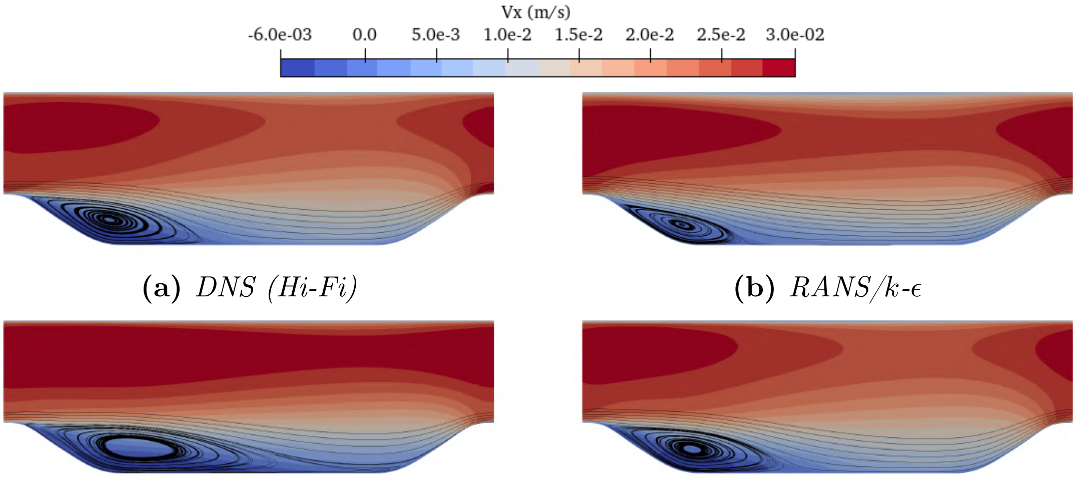

(a) *DNS (Hi-Fi)* **(b)** *RANS/k-ϵ*

(c) *RANS/SA* **(d)** *RANS/rEV, J_2 from* (3.3) *(init. k-ϵ)*

Figure 3.18: *Periodic hills a = 1.2. Streamwise velocity contours and streamlines for different flowfield solvers.*

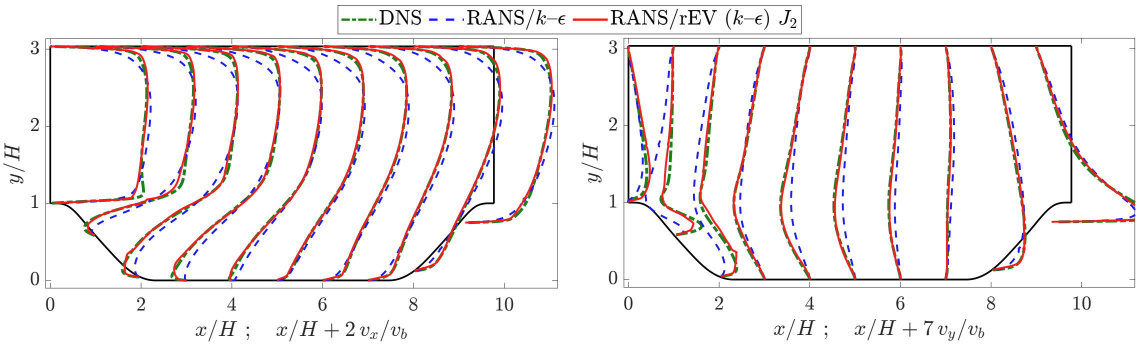

Figure 3.19: *Periodic hills a = 1.2. Mean velocity profiles in the streamwise (left) and vertical (right) directions for different flowfield solvers.*

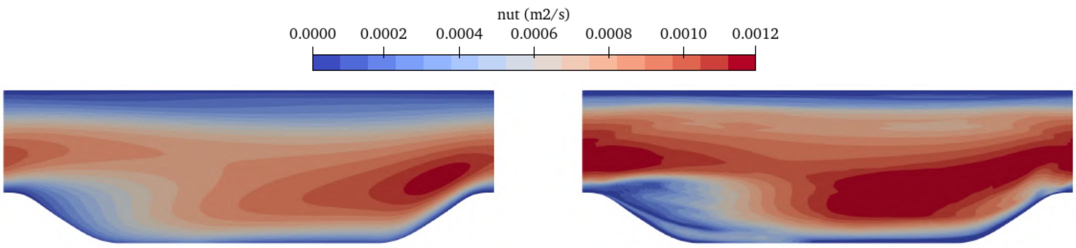

(a) *RANS/k-ϵ* **(b)** *RANS/rEV*

Figure 3.20: *Periodic hills a = 1.2. Eddy viscosity contours for different turbulence models.*

Results for a=1.5

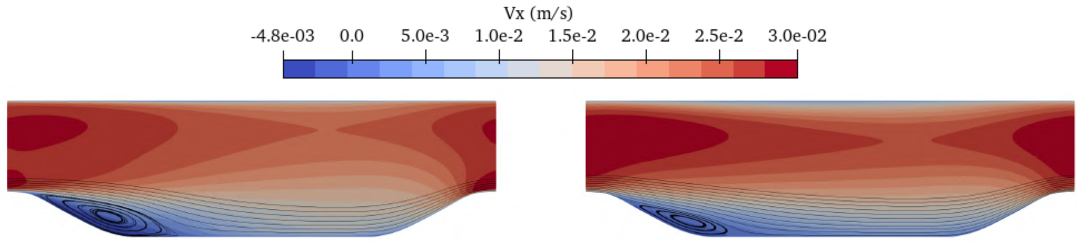

(a) *DNS (Hi-Fi)* **(b)** *RANS/k-ϵ*

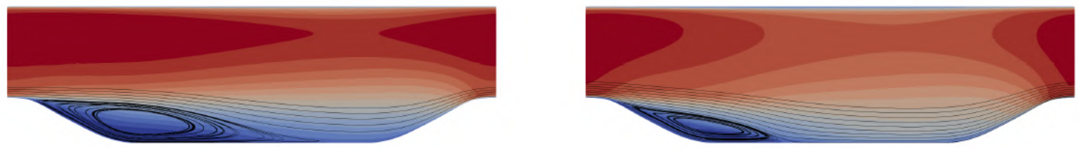

(c) *RANS/SA* **(d)** *RANS/rEV, J_2 from* (3.3) *(init. k-ϵ)*

Figure 3.21: *Periodic hills $a = 1.5$. Streamwise velocity contours and streamlines for different flowfield solvers.*

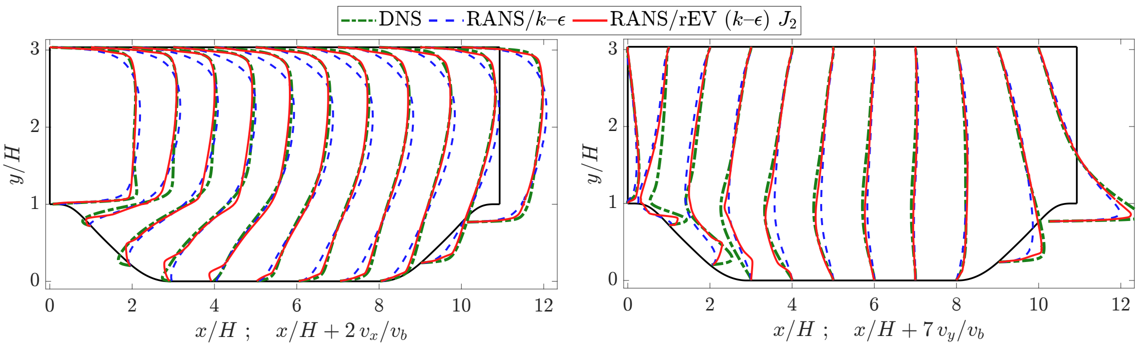

Figure 3.22: *Periodic hills $a = 1.5$. Mean velocity profiles in the streamwise (left) and vertical (right) directions for different flowfield solvers.*

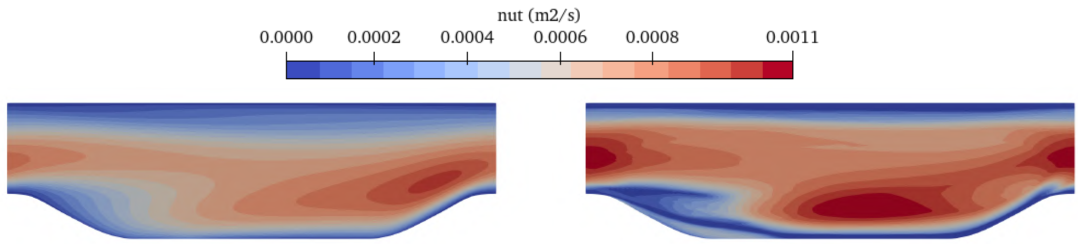

(a) *RANS/k-ϵ* **(b)** *RANS/rEV, J_2 from* (3.3) *(init. k-ϵ)*

Figure 3.23: *Periodic hills $a = 1.5$. Eddy viscosity contours for different turbulence models.*

Chapter 4

Aerodynamic coefficient-based EVA for the NACA 0012 Airfoil

The second case considered, is the flow around the NACA 0012 airfoil near the maximum lift coefficient, $C_L^{\max}$. Conventional turbulence models struggle in this regime due to strong separation and highly unsteady flow features. In this study, the EVA methodology is applied to reduce the discrepancy between the lift and drag coefficients (C_L and C_D) predicted by the baseline SA turbulence model and the corresponding experimental measurements. The loss function is formulated using either the individual aerodynamic coefficients or a weighted combination thereof. Unlike the previous chapter, no velocity-field-based EVA formulation is applied for this case.

4.1 CFD simulations for different mesh resolutions

The simulations are performed on 2D C-type structured grids ((to be handled as unstructured, though in `OpenFOAM`) provided in the Turbulence Modeling Resource database [72], using different mesh resolutions, and will be compared with the experimental data of [73] for a flow at $Re = 6 \times 10^6$ (practically incompressible, $M = 0.15$).

Specifically, two coarse meshes with $113 \times 33 \approx 4\,\mathrm{k}$ cells and $225 \times 65 \approx 15\,\mathrm{k}$ cells, as well as a fine mesh of $897 \times 257 \approx 230\,\mathrm{k}$ cells, will be tested. All three meshes are shown in Fig. 4.1. The maximum wall-normal spacing near the airfoil corresponds to $y^+ < 2.7$, $y^+ < 0.8$, and $y^+ < 0.2$, respectively; therefore all cases are treated as low-Reynolds-number simulations. The chord length is set to $c = 1$, and the kinematic viscosity is $\nu = 10^{-5}\,\mathrm{m^2/s}$, leading to a freestream velocity of $V_\infty = 60\,\mathrm{m/s}$ for the targeted Re number. In the provided meshes, the farfield boundary is located approximately 500 chord lengths away from the airfoil.

For each mesh, 2D incompressible CFD simulations were performed using the SA turbulence model across a range of angles of attack (AoA), namely AoA $= -4°, -2°, 0°, 2°, 4°, 6°, 8°, 10°, 13°, 14°, 15°, 16°, 17°, 18°$. For the higher AoA cases approaching stall, the converged solution from the immediately preceding lower angle was employed as the initial condition, which significantly improved robustness and convergence time.

Figure 4.2 presents the resulting aerodynamic coefficients C_L and C_D for the different mesh resolutions, while selected representative values are reported in Tab. 4.1. In the approximately linear regime (AoA $< 10°$), all three meshes show

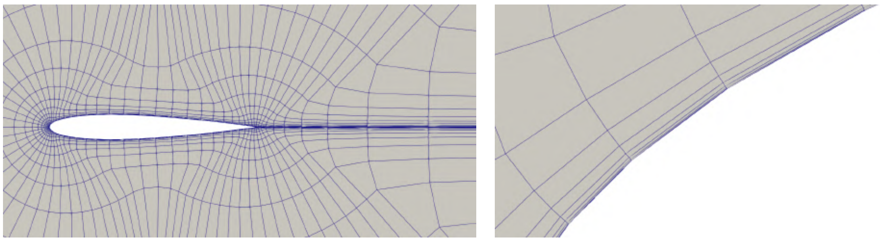

(a) 113×33 *cells*

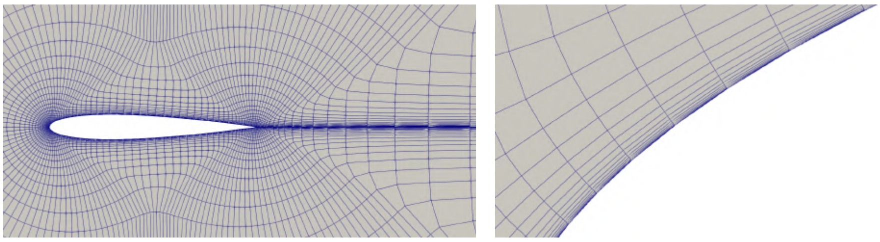

(b) 225×65 *cells*

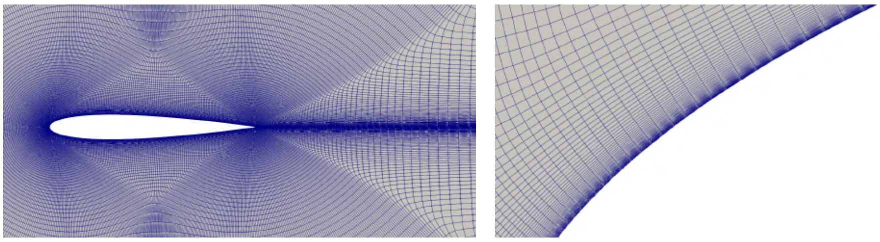

(c) 897×257 *cells*

Figure 4.1: *Comparison of mesh resolutions around the airfoil (left) and detailed view of the leading-edge boundary-layer region (right).*

very good agreement with experimental lift data. The finest grid provides the closest match across both lift and drag, while the coarser discretizations still capture the linear trend in C_L but exhibit a systematically higher drag prediction. For instance, as observed in Tab. 4.1 at 4°, the drag overprediction is on the order of 80% for the 4k-cell mesh and about 18% for the 15k-cell mesh, compared to only ≈7% deviation for the finest grid.

Beyond 10°, mesh sensitivity becomes more pronounced as flow separation effects intensify. The coarsest mesh fails to sustain accurate predictions in this regime, yielding an earlier loss of lift and predicting a maximum lift coefficient of $C_L^{\max} = 1.089$ at 13°. The intermediate mesh extends the predictive capability slightly further, with stall onset delayed to approximately 15°, reaching a $C_L^{\max} = 1.477$. In contrast, the finest mesh maintains good agreement up to approximately 17°, closely following the experimental lift curve and capturing the peak lift behavior. However, in contrast to the experimental data, which exhibits a sharp stall-related lift reduction beyond this point, the numerical solution maintains comparatively elevated lift at 18°.

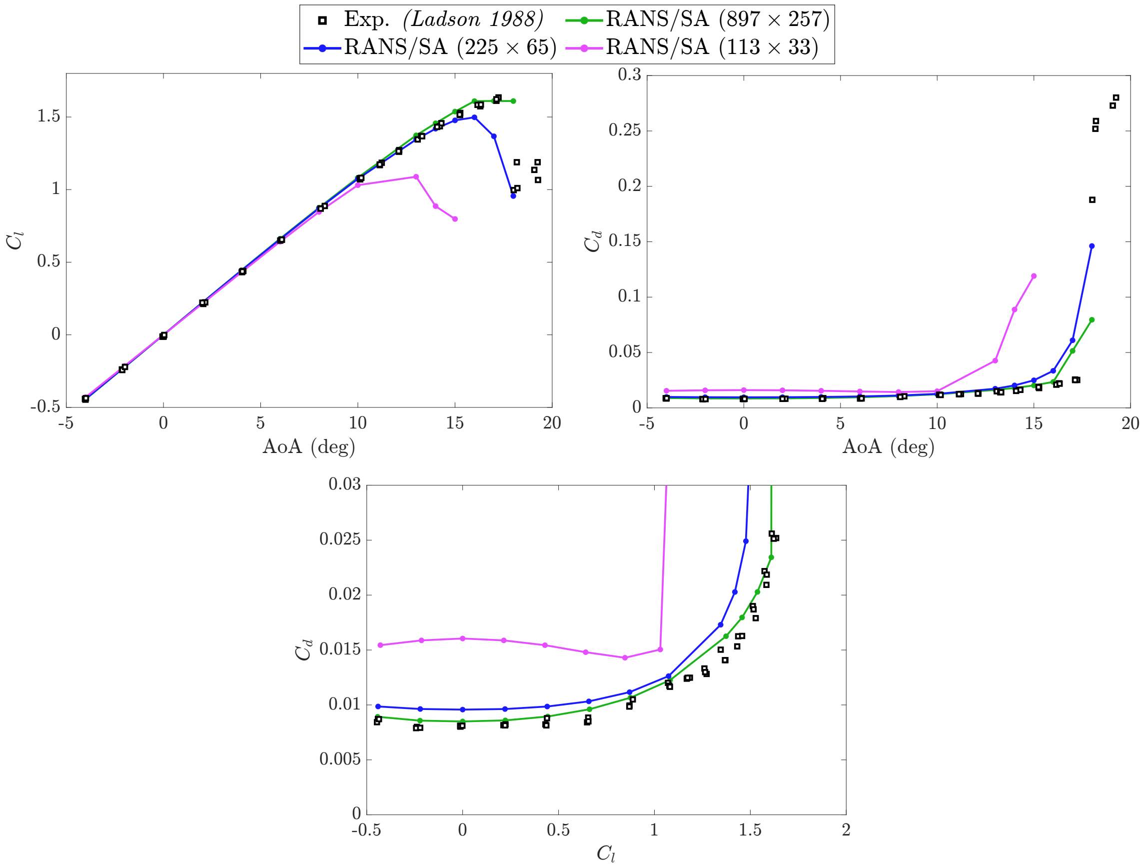

Figure 4.2: *Aerodynamic coefficients for different mesh resolutions: C_L vs AoA (top left), C_D vs AoA (top right), and C_D vs C_L polar (bottom).*

The discrepancies in the aerodynamic forces are further elucidated in Fig. 4.3, which presents the C_f distribution along the suction (upper) surface of the airfoil at AoAs 10°, and 15°. At AoA = 10°, the coarse mesh solution exhibits an onset of localized flow reversal near the trailing edge, indicating premature flow separation relative to the finer configurations. By AoA = 15°, the flow over the coarse grid is fully separated, with the separation point positioned far upstream at approximately $x/c = 0.099$. At this higher incidence, the medium-resolution mesh also begins to deviate noticeably from the fine mesh as the flow field approaches stall conditions; it predicts a separation location of $x/c \approx 0.804$, whereas the fine mesh yields $x/c \approx 0.913$, maintaining much closer agreement with the experimental reference data.

4.2 EVA for the aerodynamic force coefficients near stall

The findings of the previous section demonstrate that the results obtained with the coarse and medium mesh resolutions are unreliable at AoAs approaching stall, despite achieving full numerical convergence. For this reason, EVA will be employed

Table 4.1: *Aerodynamic coefficients and corresponding relative errors w.r.t. to experimental data for different AoA (the experimental reference values are computed by averaging the three closest AoA measurements for each case).*

AoA	**Mesh size**	C_L	**Rel. error in C_L (%)**	C_D	**Rel. error in C_D (%)**
4°	Exp. [73]	0.436	—	0.00839	—
	230k cells	0.443	-1.6	0.00895	6.7
	15k cells	0.441	-1.3	0.00986	17.5
	4k cells	0.429	1.6	0.0154	83.5
10°	Exp. [73]	1.076	—	0.0118	—
	230k cells	1.082	0.6	0.0123	4.2
	15k cells	1.074	0.2	0.0126	6.8
	4k cells	1.030	4.3	0.0154	30.5
13°	Exp. [73]	1.361	—	0.0148	—
	230k cells	1.373	0.9	0.0163	10.1
	15k cells	1.345	1.2	0.0173	16.9
	4k cells	1.089	-20.0	0.0427	188.5
15°	Exp. [73]	1.519	—	0.0185	—
	230k cells	1.537	1.2	0.0203	9.7
	15k cells	1.477	-2.8	0.0249	34.6
	4k cells	0.798	-47.5	0.119	543.2
17°	Exp. [73]	1.623	—	0.0253	—
	230k cells	1.610	-0.8	0.0515	103.6
	15k cells	1.367	-15.8	0.0610	141.1

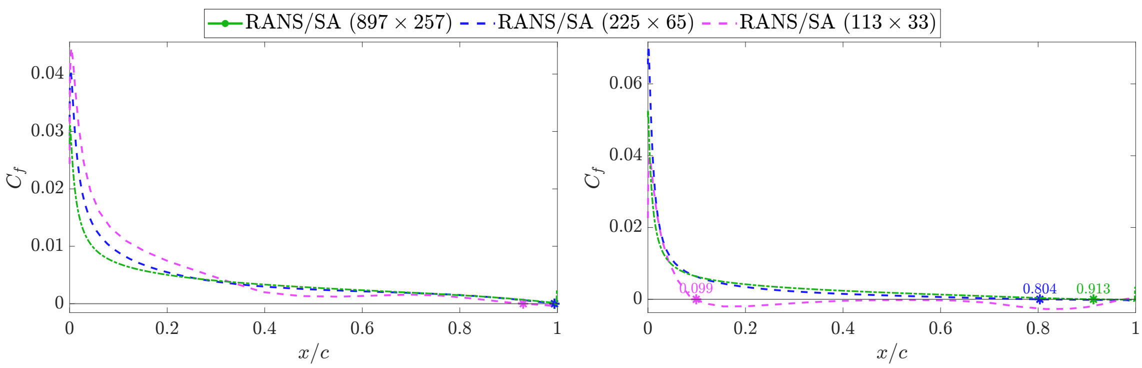

(a) $AoA = 10°$ **(b)** $AoA = 15°$

Figure 4.3: *Suction-side skin-friction coefficient (C_f) for different mesh resolutions; the separation point is marked for $AoA = 15°$.*

for both cases, in order to improve the prediction of the aerodynamic coefficients and, consequently the accuracy of the computed flow field around the airfoil.

4.2.1 Coarse mesh (4k cells) at 10° AoA

At AoA = 10°, the coarse mesh results deviate from the experimental data and fine-mesh solution (Fig. 4.2). As illustrated in Fig. 4.3a, the coarse mesh predicts negative C_f values starting at $x/c \approx 0.93$, signaling an exaggerated recirculation zone for this relatively low AoA. Comparing the trailing edge streamlines confirms this discrepancy; the coarse mesh yields a distinct separation region (Fig. 4.5b), whereas the fine mesh resolves a fully attached flow (Fig. 4.5a).

The EVA method is consequently applied, utilizing the available experimental data through the following loss functions:

- The minimization of the discrepancy between the computed and experimental drag coefficients:
$$J = \frac{1}{2}\left(C_D - C_{D,\mathrm{exp}}\right)^2 \equiv f(C_D) \tag{4.1}$$
presented in Sec. 2.3.2, where $C_{D,\mathrm{exp}} = 0.0118$ corresponds to the experimental value reported in Tab. 4.1.
- A combined loss function defined as:
$$J = 0.5\,\frac{1}{2}\left(C_D - C_{D,\mathrm{exp}}\right)^2 + 0.5\,\frac{1}{2}\left(C_L - C_{L,\mathrm{exp}}\right)^2 \equiv 0.5\,f(C_D) + 0.5\,f(C_L) \tag{4.2}$$
where $C_{D,\mathrm{exp}} = 0.0118$ and $C_{L,\mathrm{exp}} = 1.076$ are the experimental values listed in Tab. 4.1. This formulation is introduced to prevent convergence toward nonphysical solutions by simultaneously constraining both aerodynamic coefficients through a weighted combination of drag and lift contributions. The lift-related term in the EVA method is implemented analogously to the drag formulation described in Sec. 2.3.2, with the force direction aligned with the lift direction, i.e., perpendicular to the drag direction.

The flow-field solution $(\mathbf{v}, p, \nu_t)$ obtained from the RANS/SA simulation is utilized to initialize the EVA. Both the primal and adjoint problems are discretized using second-order schemes; their convergence history for the first EVA cycle is illustrated in Fig. 4.4. At the end of each cycle, the steepest descent method is employed to update ν_t within each mesh cell. The results for the two EVA problems (with the rEV field incorporated into the RANS equations) are summarized in Tab. 4.2. The loss function $J = f(C_D)$ converges exactly to the target $C_{D,\mathrm{exp}}$ within 7 cycles using a steepest descent step size of $\eta = 5 \cdot 10^{-8}$, while for the second formulation, $J = 0.5\,f(C_D) + 0.5\,f(C_L)$, it is reduced by ~99.8% relative to its initial value after only 20 cycles.

Tab. 4.2 indicates that both EVA formulations provide excellent predictions of the aerodynamic coefficients C_L and C_D, in close agreement with the experimental data (relative error < 1%), even surpassing the accuracy of the finest mesh

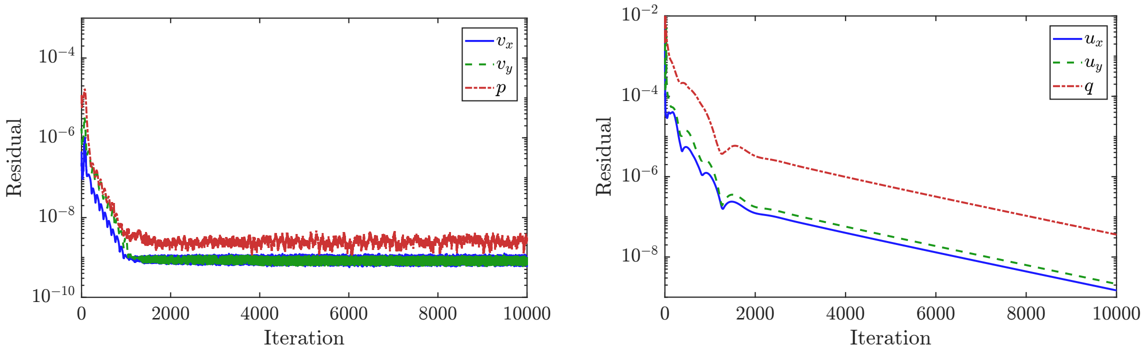

Figure 4.4: *EVA for the coarse mesh, 10° AoA. Convergence history for the primal (left) and adjoint (right) problem for the first cycle for* $J = f(C_D)$.

Table 4.2: *EVA for the coarse mesh, 10° AoA. Aerodynamic coefficients and corresponding relative errors w.r.t. experimental data.*

Simulation type	C_L	**Rel. error in** C_L **(%)**	C_D	**Rel. error in** C_D **(%)**	**Separat. point** (x/c)
Exp. [73]	1.076	—	0.0118	—	no data
RANS/SA (230k cells)	1.082	0.6	0.0123	4.2	0.994
RANS/SA (4k cells)	1.030	4.3	0.0154	30.5	0.930
RANS/rEV (4k cells) $J = f(C_D)$	1.082	**0.6**	0.0118	**0.0**	0.975
RANS/rEV (4k cells) $J = 0.5\, f(C_D) + 0.5\, f(C_L)$	1.078	**0.2**	0.0119	**0.8**	0.973

simulation. Moreover, both formulations shift the separation point further downstream on the suction side, thereby eliminating the unphysical recirculation zones observed in the RANS/SA solution.

This behavior is clearly illustrated in the velocity contours in Fig. 4.5, where both EVA-based solutions produce a flowfield similar to that of the fine-mesh case (230k cells). Furthermore, in the C_f distribution in Fig. 4.6, the corrected RANS/rEV curves approach the RANS/SA results on the finer mesh; in particular, the excessive leading-edge force predicted by RANS/SA on the coarse mesh is significantly reduced, and the separation point is more accurately captured.

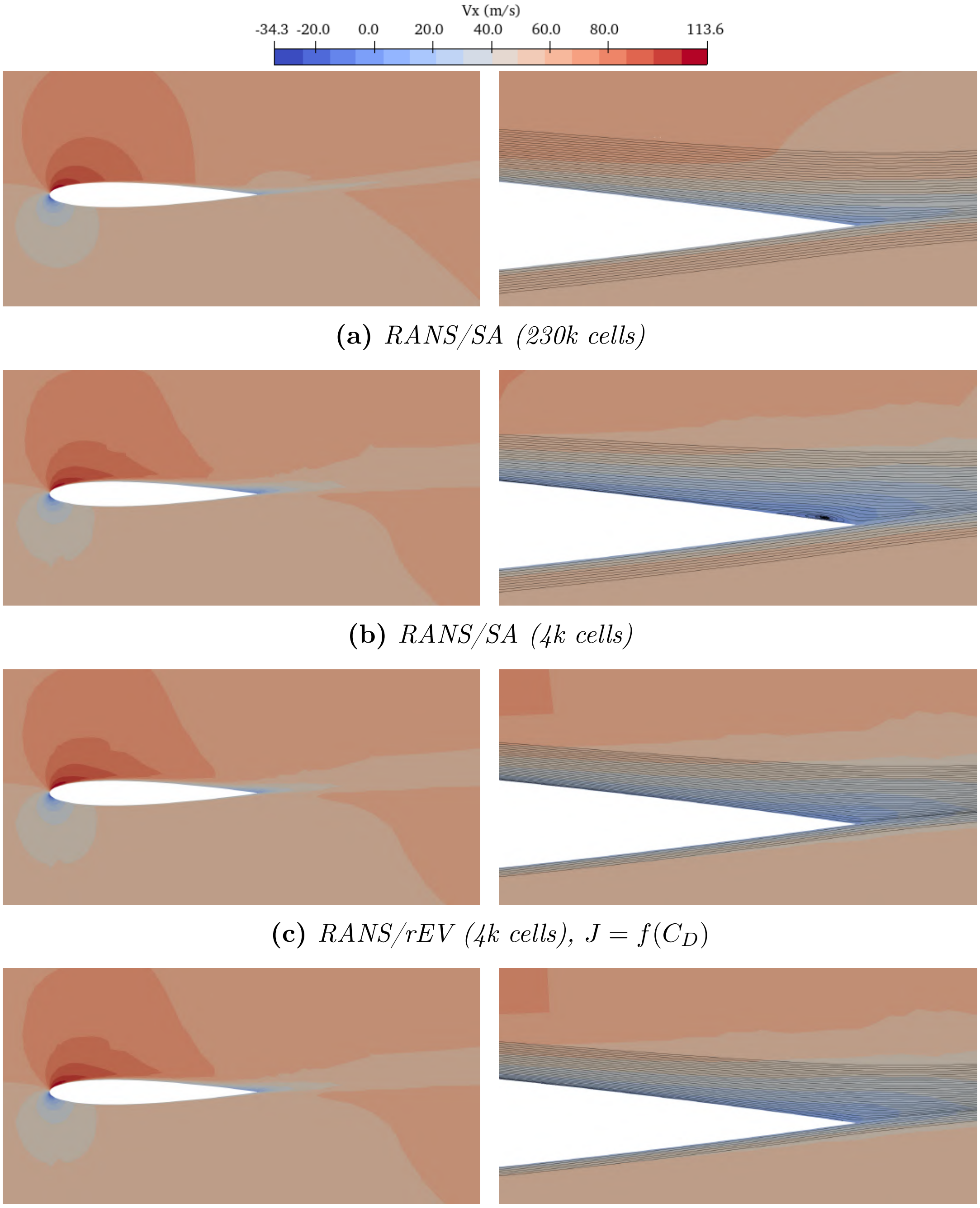

(a) *RANS/SA (230k cells)*

(b) *RANS/SA (4k cells)*

(c) *RANS/rEV (4k cells),* $J = f(C_D)$

(d) *RANS/rEV (4k cells),* $J = 0.5\, f(C_D) + 0,5\, f(C_L)$

Figure 4.5: *EVA for the coarse mesh,* 10° *AoA. Streamwise velocity contours (left) and streamlines near the trailing edge (right) for different turbulence models.*

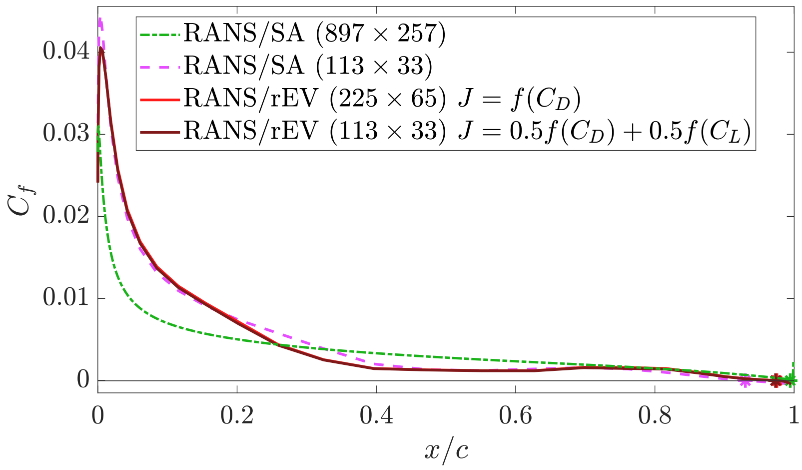

Figure 4.6: *EVA for the coarse mesh, 10° AoA. Suction-side skin-friction coefficient (C_f) for different turbulence models.*

4.2.2 Coarse & intermediate mesh (4k , 13k cells) at 15° AoA

In this case, the same loss functions employed for the EVA problem in Sec. 4.2.1 are considered, targeting the experimental data at AoA $= 15°$ ($C_{D,\text{exp}} = 0.0185$, $C_{L,\text{exp}} = 1.361$). As reported in Tab. 4.1, the fine mesh solution remains in relatively good agreement with the experimental measurements. In contrast, the intermediate mesh (15k cells) underpredicts lift while overpredicting drag, indicating an earlier onset of stall. Meanwhile, the coarse mesh (4k cells) exhibits significantly poorer performance, having developed extensive recirculation regions, as illustrated in the velocity contours provided in Fig. 4.9b. Both deficient cases will be subsequently corrected through the application of the two alternative EVA formulations. All simulation results are summarized in Tab. 4.3.

EVA for the intermediate mesh

For the intermediate mesh (13k cells), the SD of the design variables are updated (throughout the 50 EVA cycles) using the steepest descent method with a step size of $\eta = 5 \cdot 10^{-9}$. As shown in Tab. 4.3, the RANS/rEV approach employing the EVA-v_t field and targeting solely the drag coefficient matches the experimental value $C_{D,\text{exp}}$ exactly. However, this comes at a cost for C_L, as it is overpredicted to a greater extent than in the baseline RANS/SA solution. Conversely, when the EVA process is performed using a weighted loss function that accounts for both C_L and C_D, substantial improvements are achieved for both quantities relative to the initial solution. In this case, the cost function decreases by 86.5% after 50 cycles, though the final C_D still deviates from the experimental reference by approximately 16.7%. Notably, both RANS/rEV variants successfully shift the separation point of the intermediate mesh closer to the fine-mesh (230k cells) reference.

Further insight can be obtained from the velocity contours shown in Fig. 4.7, where the RANS/SA simulations on the fine and intermediate meshes are com-

Table 4.3: *EVA for the coarse & intermediate mesh,* 15° *AoA. Aerodynamic coefficients and corresponding relative errors w.r.t. experimental data.*

Simulation type	C_L	**Rel. error in** C_L **(%)**	C_D	**Rel. error in** C_D **(%)**	**Separat. point** (x/c)
Exp. [73]	1.519	—	0.0185	—	no data
RANS/SA (230k cells)	1.537	1.2	0.0203	9.7	0.913
RANS/SA (15k cells)	1.477	-2.8	0.0249	34.6	0.804
RANS/rEV (15k cells) $J = f(C_D)$	1.594	**4.9**	0.0185	**0.0**	0.932
RANS/rEV (15k cells) $J = 0.5\,f(C_D) + 0.5\,f(C_L)$	1.527	**0.5**	0.0216	**16.7**	0.865
RANS/SA (4k cells)	0.798	-47.5	0.119	543.2	0.099
RANS/rEV (4k cells) $J = f(C_D)$	1.717	**13.0**	0.00848	**54.2**	0.361
RANS/rEV (4k cells) $J = 0.5\,f(C_D) + 0.5\,f(C_L)$	1.586	**4.4**	0.0348	**88.1**	0.309

pared with the RANS/rEV results obtained using EVA. The application of EVA significantly reduces the overpredicted recirculation region observed in the baseline intermediate-mesh simulation. In particular, the $J = f(C_D)$ case reproduces the streamlines of the fine-mesh solution remarkably well, while the $J = 0.5, f(C_D) + 0.5, f(C_L)$ case predicts a slightly larger recirculation zone, although still substantially smaller than that of the baseline RANS/SA intermediate-mesh solution.

The effectiveness of the method is further demonstrated by the C_f distributions shown in Fig. 4.3b. Both RANS/rEV solutions closely follow the fine-mesh reference curve, especially in the region $x/c > 0.2$, providing a noticeably improved agreement compared with the baseline RANS/SA result. Near the leading edge, however, both cases still exhibit a slight overprediction of the skin-friction coefficient. Consequently, the $J = f(C_D)$ EVA process, shifts the separation point marginally downstream relative to the fine-mesh RANS/SA solution in order to match the experimental value.

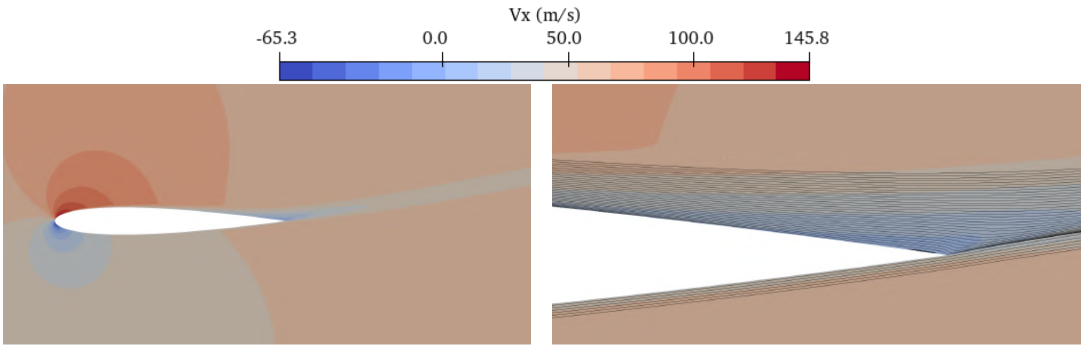

(a) *RANS/SA (230k cells)*

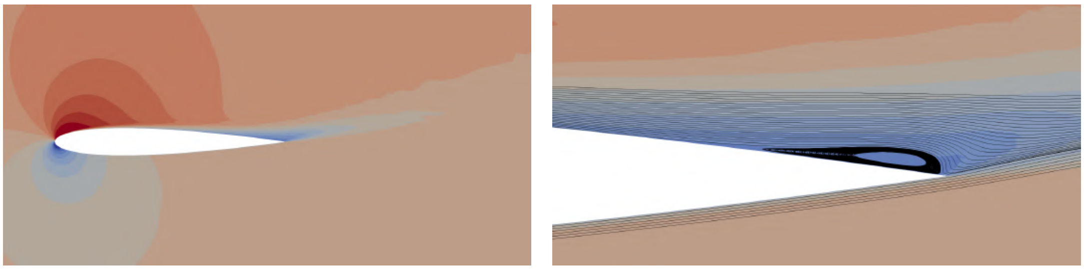

(b) *RANS/SA (13k cells)*

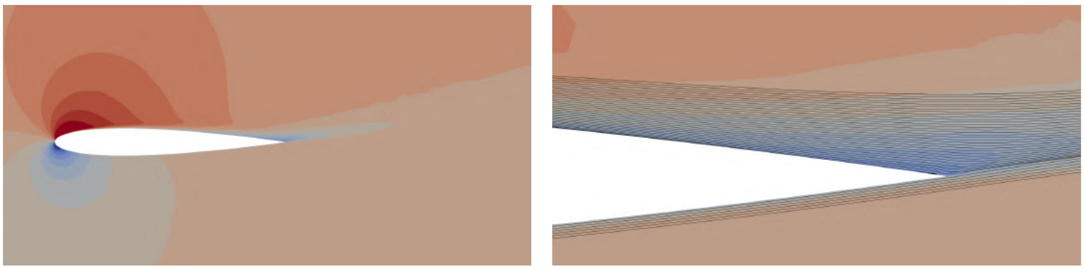

(c) *RANS/rEV (13k cells), $J = f(C_D)$*

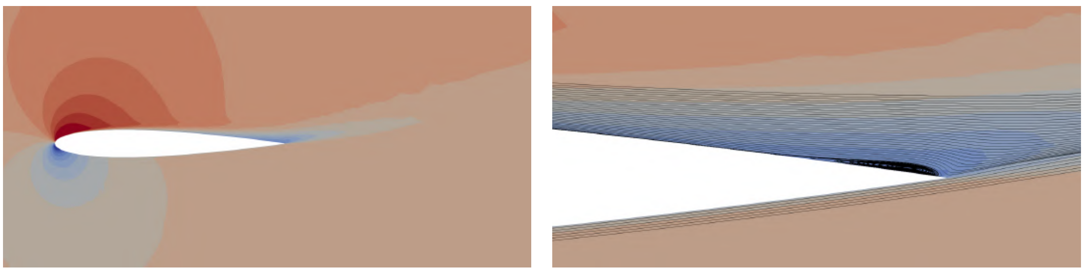

(d) *RANS/rEV (13k cells), $J = 0.5\, f(C_D) + 0{,}5\, f(C_L)$*

Figure 4.7: *EVA for the intermediate mesh, 15° AoA. Streamwise velocity contours (left) and streamlines near the trailing edge (right) for different turbulence models.*

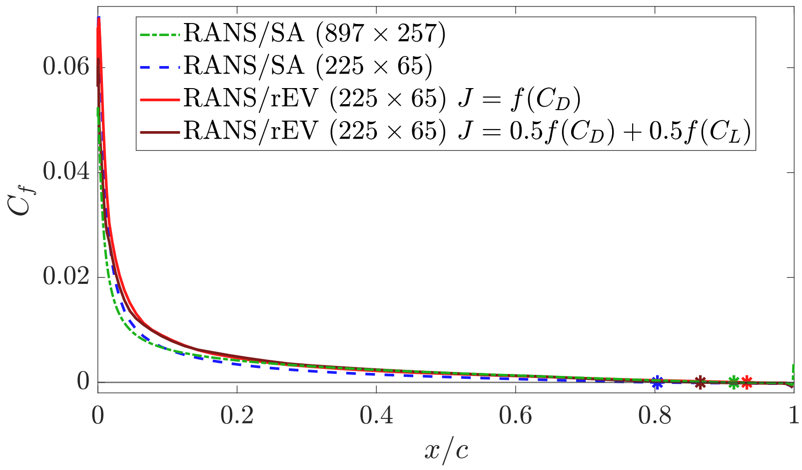

Figure 4.8: *EVA for the intermediate mesh,* 15° *AoA. Suction-side skin-friction coefficient (C_f) for different turbulence models.*

EVA for the coarse mesh

The coarse-mesh simulation at 15° AoA predicts a fully detached stalled flow when using the baseline RANS/SA model, whereas experimental observations indicate that the flow remains largely attached to the airfoil. Consequently, this case represents the most challenging test scenario considered in the present study. After 50 optimization cycles, using steepest-descent update with a step size of $\eta = 5 \times 10^{-8}$, both EVA formulations produce noticeable improvements, as summarized in Table 4.3. For the $J = f(C_D)$ problem, the J value is reduced by approximately 99%; the relative error for C_D decreases from more than 500% for the initial RANS/SA solution to 54.2% w.r.t. the experimental data, while the error in the C_L calculation is also reduced, from 47.5% to 13%. The alternative loss function, $J = 0.5, f(C_D) + 0.5, f(C_L)$, decreases by 98.2% overall, yielding a more accurate prediction of C_L (4.4% relative error compared to the reference data), while still providing a substantial improvement in drag prediction. Nevertheless, both optimized solutions continue to significantly overpredict the drag coefficient.

The underlying reason becomes evident when examining the velocity contours in Fig. 4.9. Although the corrected RANS/rEV solutions are considerably closer to the fine-grid results, the streamline patterns near the trailing edge still reveal the presence of large recirculation regions. This behavior is even more clearly illustrated in Fig. 4.10. While the RANS/rEV skin-friction distribution approaches that obtained from the fine-grid RANS/SA simulation, C_f remains negative over a significant portion of the airfoil surface ($x/c > 0.4$), indicating persistent flow separation.

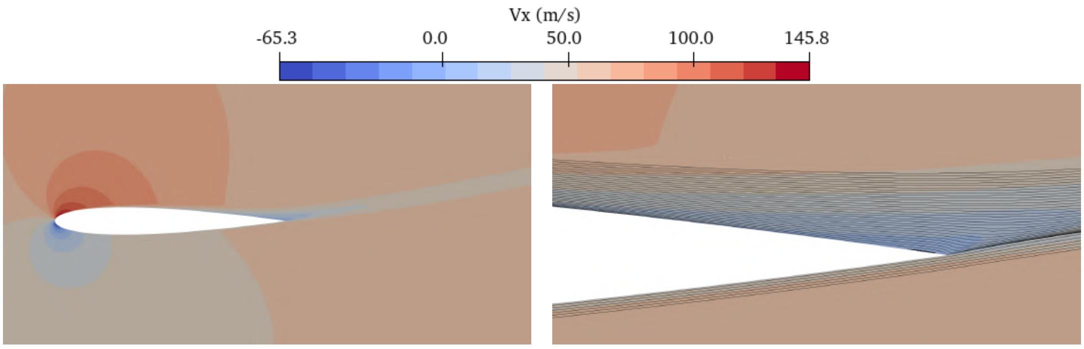

(a) *RANS/SA (230k cells)*

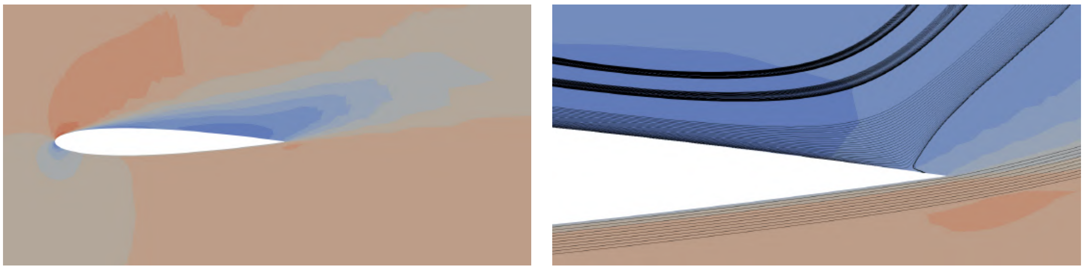

(b) *RANS/SA (4k cells)*

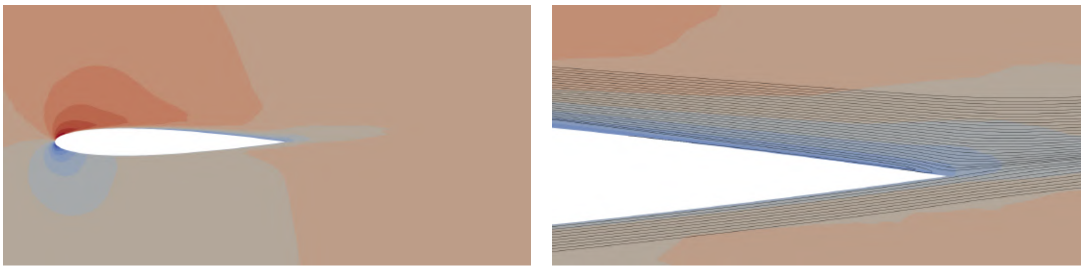

(c) *RANS/rEV (4k cells),* $J = f(C_D)$

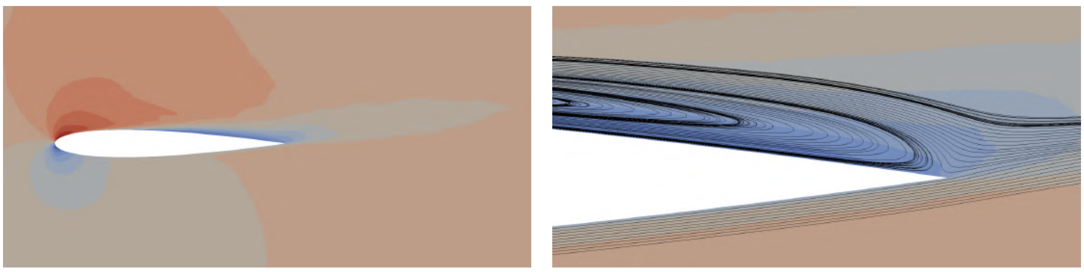

(d) *RANS/rEV (4k cells),* $J = 0.5\, f(C_D) + 0,5\, f(C_L)$

Figure 4.9: *EVA for the coarse mesh, 15° AoA. Streamwise velocity contours (left) and streamlines near the trailing edge (right) for different turbulence models.*

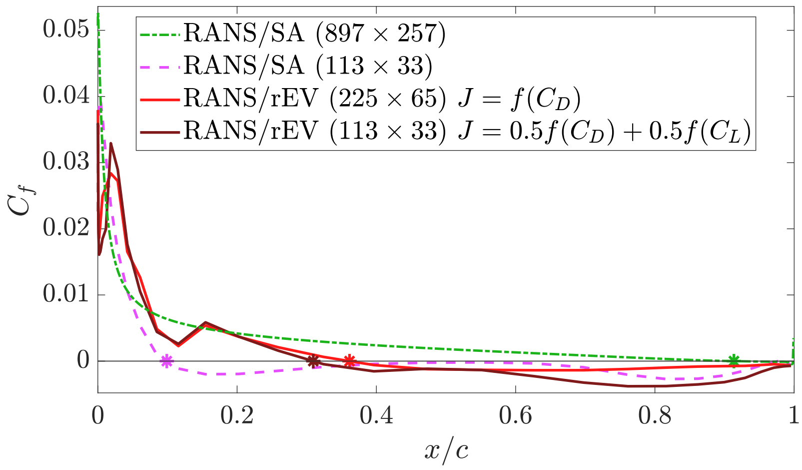

Figure 4.10: *EVA for the coarse mesh, 15° AoA. Suction-side skin-friction coefficient (C_f) for different turbulence models.*

Overall, these results suggest that EVA based solely on minimizing discrepancies in integral aerodynamic force coefficients between Low- and Hi-Fi datasets can correct the underlying flow field and substantially reduce the size of separated regions near stall conditions. However, the method performs best when the baseline solution is already reasonably close to the Hi-Fi reference, such as in cases where the separation is only moderately overpredicted (e.g., Figs. 4.5 and 4.7). In contrast, when the Low-Fi solution is quite different than the targeted Hi-Fi one, as in Fig. 4.9, the optimization may converge to flowfields that improvs the loss function value but remain physically unrealistic. Despite this limitation, the results presented in this chapter demonstrate the potential of the EVA framework as a tool for improving conventional turbulence model predictions in near-stall conditions, where accurately capturing separation and reattachment phenomena remains particularly challenging.

Chapter 5
Velocity-based EVA for 3D Car Models

In this chapter, the EVA method is applied to complex 3D automotive flows. To the author's knowledge, only Tsolakos [36] has previously attempted FI for 3D automotive cases, specifically for the Toyota Aygo X vehicle, successfully completing three EVA cycles. Most other studies have focused on utilizing only the ML component of their FI/ML frameworks for 3D applications, where the learned corrections are trained on 2D benchmark turbulence-modelling cases. For example, Wu et al. [16] employed an SR relation extracted through FI from the NASA hump and curved backward-facing step cases, and applied it to the Ahmed body and the SAE Reference Model. Similarly, Nishi et al. [18] trained a neural network on several airfoils exhibiting flow separation and applied the resulting model to the NASA Common Research Model (CRM) aircraft.

In the following sections, the wall-function variant of the EVA method is employed to improve the prediction of the flow-field around the Ahmed body, the SAE Notchback Reference Model, and two variants of the DrivAer car model. The loss function to be minimized is:

$$J = \frac{1}{2}\int_{\Omega} \left(v_i - v_{i,\text{hi-fi}}\right)^2 \, d\Omega \tag{5.1}$$

which worked well in the periodic hills case (Chapt. 3). The objective is to assess the capability of the proposed EVA framework to improve aerodynamic predictions in realistic, industrially relevant 3D flow configurations.

DES will be employed as the Hi-Fi solver; this stands for a (unsteady) hybrid RANS–LES approach, proposed by Spalart et al. [38], which employs a RANS model in the boundary layer and transitions to LES in detached regions. Compared with LES, the DES model significantly reduces computational cost at high Reynolds numbers while maintaining improved accuracy in separated flow regions [74], making it well suited for complex 3D automotive aerodynamics.

5.1 Ahmed Body with 35° Slant Angle

The Ahmed body, first proposed by Ahmed in 1984 [56], serves as a standard generic car model widely used to investigate wake dynamics, vortex structures, and aerodynamic forces across a broad range of geometric configurations. As displayed in Fig. 5.1, the standardized geometry consists of a rounded front end, a flat roof, a flat underbody section, an angled back slant (or a rear window) and a vertical base at the rear.

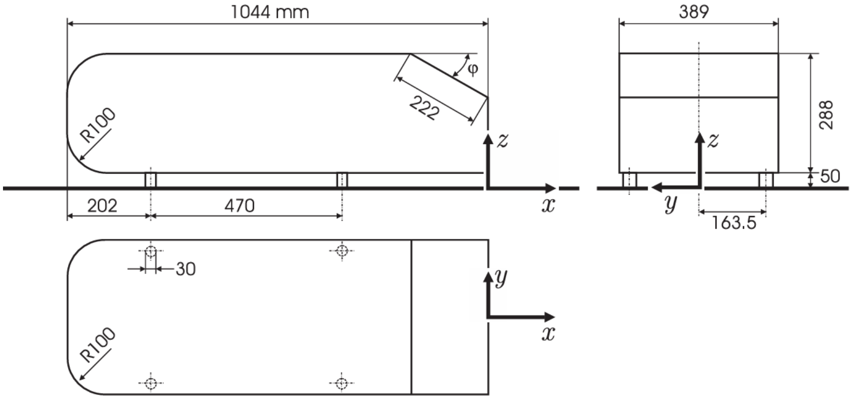

Figure 5.1: *Ahmed body geometry (dimensions in millimeters); in this work $\phi = 35°$.*

The flow behind the Ahmed body aligned with the incoming stream consists of a pair of longitudinal vortices (often referred to as C-pillar vortices), a region of either separated or attached flow over the rear slant, and a highly turbulent recirculating wake behind the vertical base [75]. The wake structure, the reattachment location of the separation bubble, and the strength of the counter-rotating vortices all depend strongly on the rear slant angle ϕ. The maximum drag has been reported at a slant angle of 30° [56]. Below this critical angle, strong counter-rotating vortices are present, and the flow separates near the mid-region of the upper edge and reattaches on the slanted surface. For angles above the critical value (such as in the present study), these vortices weaken significantly, leading to fully separated flow over the entire slant surface [76, 77]. A schematic representation of the flow topology expected for each case is provided in Fig. 5.2.

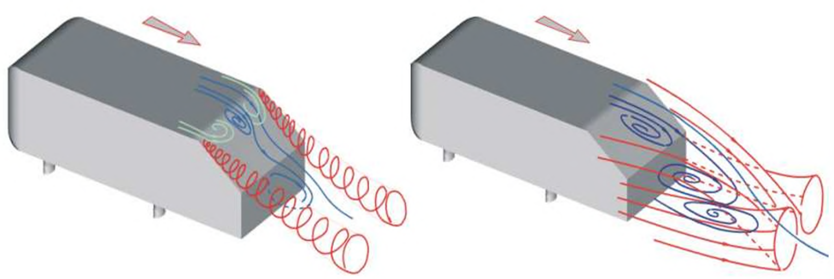

Figure 5.2: *Ahmed body. Flow topology for two different slant angles: $\phi = 25°$, with closed separation bubble (left), and $\phi = 35°$ with fully separated flow (right); taken from [78].*

The test case considered in this thesis, replicates the configuration defined in the 10th ERCOFTAC Workshop on Refined Turbulence Modelling [78]: a body with a supercritical angle of $\phi = 35°$. The working fluid is air, with a kinematic viscosity of $\nu = 1.5 \cdot 10^{-5}$ m^2/s and a freestream velocity of $v_b = 40$ m/s, resulting in a Reynolds number of $Re = 768,000$, based on the body height $H = 288$ mm. Under these conditions, experiments were performed by Lienhart and Becker [79], comprising flow visualization, hot-wire measurements, and laser-Doppler anemometer (LDA) data; the dataset is available in [80].

For the simulations conducted in this thesis, a full-car wind tunnel computational domain is employed (due to DES inherently asymmetric nature of transient wake shedding), shown in Fig. 5.3a. The coordinate system is defined with the x-axis in the streamwise direction, the y-axis in the lateral direction, and the z-axis in the vertical direction. The boundary conditions for the domain are prescribed as follows:

- Inlet: A uniform streamwise velocity profile of $\mathbf{v} = (v_b, 0, 0) = (40, 0, 0)$ m/s is specified.
- Domain Sides and Top: Modeled using symmetry conditions, by exploiting the fact these are situated sufficiently far from the vehicle.
- Floor and Car Surface: No-slip conditions.

The computational mesh is generated using `OpenFOAM`'s integrated meshing utilities, `blockMesh` and `snappyHexMesh`, the resulting resolution is approx. 2.2M cells. The mesh layout and local refinement zones are illustrated in Fig. 5.3b and Fig. 5.3c. To verify the near-wall grid resolution, a RANS/SA simulation was conducted, resulting in an average y^+ value across the vehicle body surface of $\sim$88, as shown in Fig. 5.3d.

A DES/SA simulation was conducted for 5 s of physical time, with the final 3 s used for time-averaging, in order to extract the mean flow profiles. Fig. 5.4 presents three instantaneous velocity contours on the symmetry plane. A noticeable recirculation bubble is observed over the slant surface, complemented by a substantial region of strong reverse flow downstream of the vehicle.

The mean drag coefficient computed from the DES/SA simulation is $C_D^{\text{DES,mean}} = 0.306$; its instantaneous evolution is shown in Fig. 5.5. In comparison, the steady-state RANS/SA simulation yields a value of $C_D^{\text{RANS/SA}} = 0.329$ after 5,000 iterations, representing a 7.5% overprediction of the Hi-Fi corresponding figure.

The v_x contours and streamlines for the two solvers are depicted in Figs. 5.6a and 5.6b. It is observed that the DES/SA model resolves a larger recirculation bubble; this complete separation causes the trailing C-pillar longitudinal vortices to break down and burst in the near-wake. The differences in wake dynamics are further illustrated through visualizations of the coherent flow structures using the non-dimensional λ_2-criterion ($\lambda_2^* = \lambda_2 H^2 / v_b^2$, where $H = 0.288$ m is the body height), which identifies vortex cores as regions where pressure effects dominate over strain [81]; the resulting iso-surfaces are colored by the normalized helicity, indicating the rotation direction (see App. A for details). While the RANS/SA

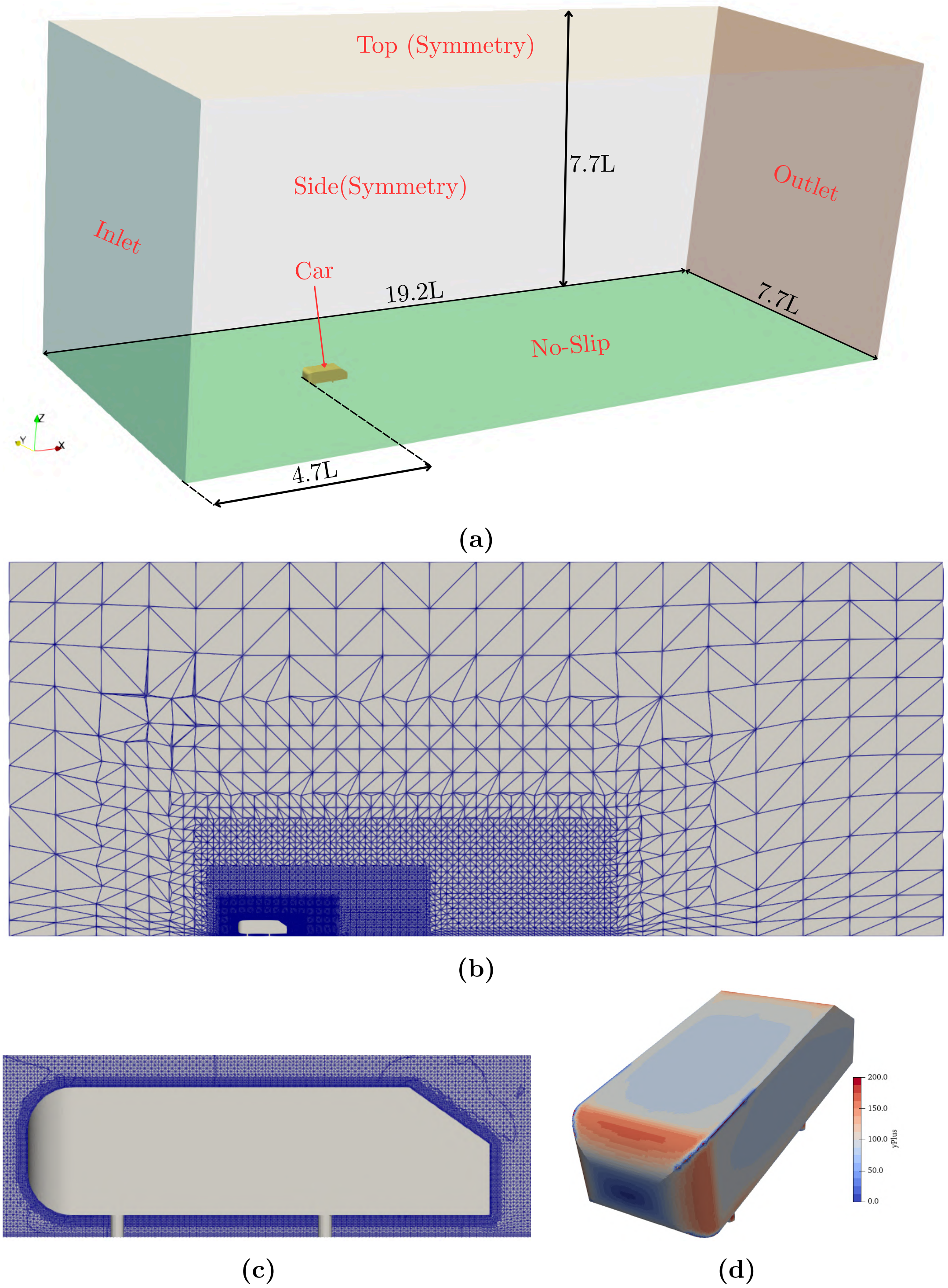

Figure 5.3: *Ahmed body. (a) Computational domain based on the length* $L = 1.044$ *m of the car, (b) mesh on the symmetry plane, (c) close-up view of the mesh around the car on the symmetry plane, (d)* y^+ *distribution on the first near-wall cell over the full-car surface.*

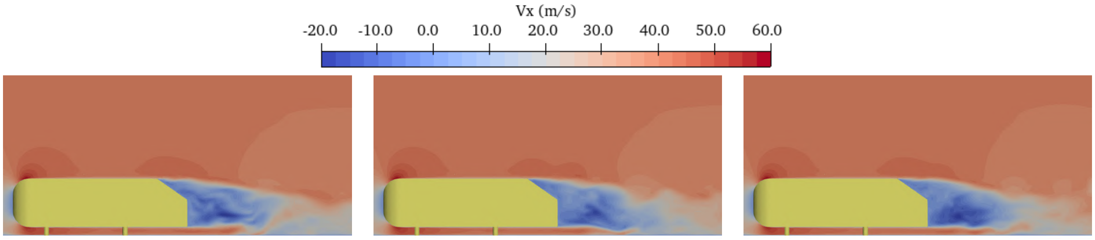

(a) $t = 4.8\ s$ **(b)** $t = 4.9\ s$ **(c)** $t = 5.0\ s$

Figure 5.4: *Ahmed body. DES/SA instantaneous streamwise velocity contours on the symmetry plane.*

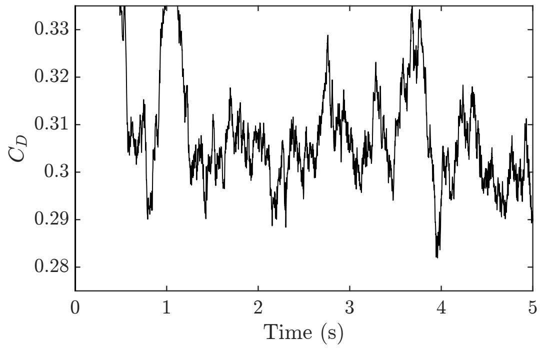

Figure 5.5: *Ahmed body. C_D convergence for the unsteady DES/SA simulation.*

simulation predicts highly stable, prominent C-pillar vortices that induce strong suction over the rear slant, the mean DES/SA flowfield captures their breakdown. The subsequent loss of vortex-induced low pressure over the rear slant decreases the pressure drag, explaining the lower C_D yielded by the Hi-Fi simulation.

The wall-function based variant of the EVA framework (described in Sec. 2.8) is subsequently applied, utilizing the baseline RANS/SA $\mathbf{v}, p, \nu_t$ fields for initialization. Indicative convergence histories for both the primal and adjoint problems during the first EVA cycle are presented in Fig. 5.7. Due to numerical challenges in fully converging the primal residuals, the fields are averaged over the last 2,000 of the total 5,000-iteration run. In total, 16 EVA cycles are executed using the steepest descent method to update the design variables (the eddy viscosity field), yielding a 4.6% reduction in J value. The initial and corrected ν_t fields are compared in Fig. 5.8, where it is apparent that the EVA method attenuates the eddy viscosity near the rear slant region.

When the corrected ν_t fields are incorporated into the RANS equations through the RANS/rEV solver, the resulting velocity contours and vortex iso-surfaces exhibit substantial changes, as depicted in Fig. 5.6c. Relative to the baseline RANS/SA solution, the RANS/rEV model decreases the length of the longitudinal C-pillar vortices, enlarges the recirculation region, extending it downward into the wake, and improves the agreement of the streamline topology with the DES/SA reference solution. Consequently, the drag prediction improves, yielding

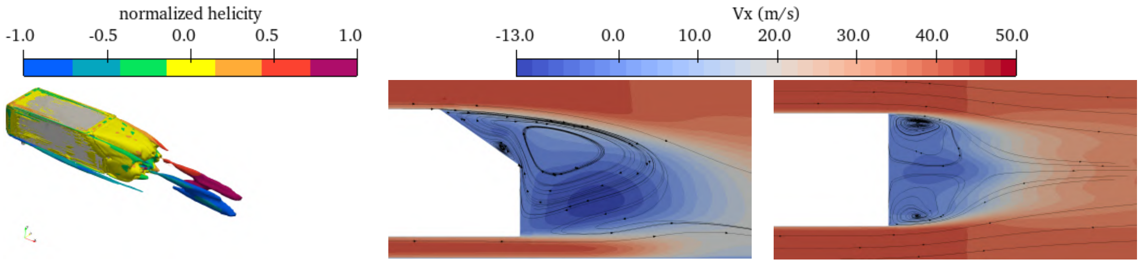

(a) *DES/SA*

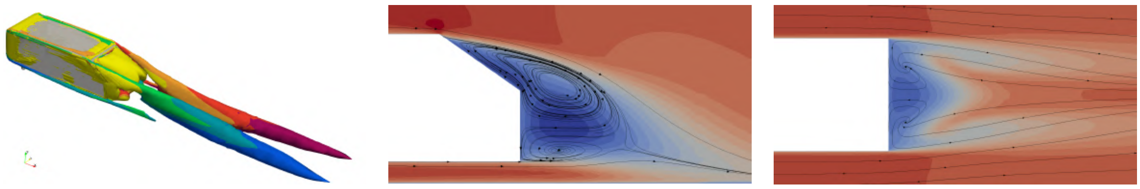

(b) *RANS/SA*

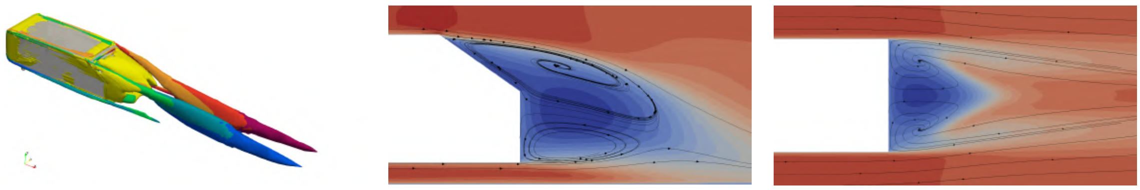

(c) *RANS/rEV*

Figure 5.6: *Ahmed body. Iso-surfaces of the non-dimensional λ_2-criterion ($\lambda_2{}^* = -0.1$) (left), mean streamwise velocity contours and streamlines on the symmetry plane near the slant (middle), and on a plane at $z = 0.2$ m normal to the ground (right).*

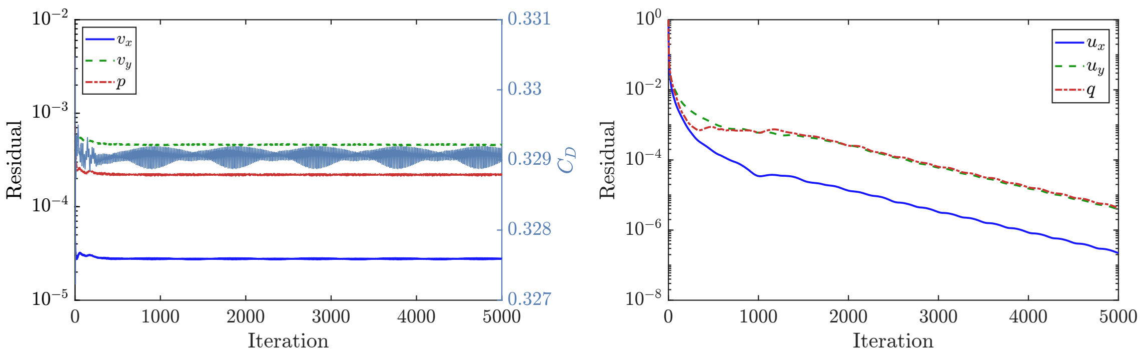

Figure 5.7: *Ahmed body. Convergence history for the primal (left) and adjoint (right) EVA problem for the first cycle.*

$C_D^{\text{RANS/rEV}} = 0.302$, which is significantly closer to the Hi-Fi DES/SA result.

The effectiveness of the proposed correction is further verified by analyzing specific v_x profiles within the slant region and the wake of the body (Fig. 5.9). The DES/SA profiles exhibit excellent agreement with the hot-wire measurements of [79], thereby justifying its use as the Hi-Fi reference solution. In contrast, the

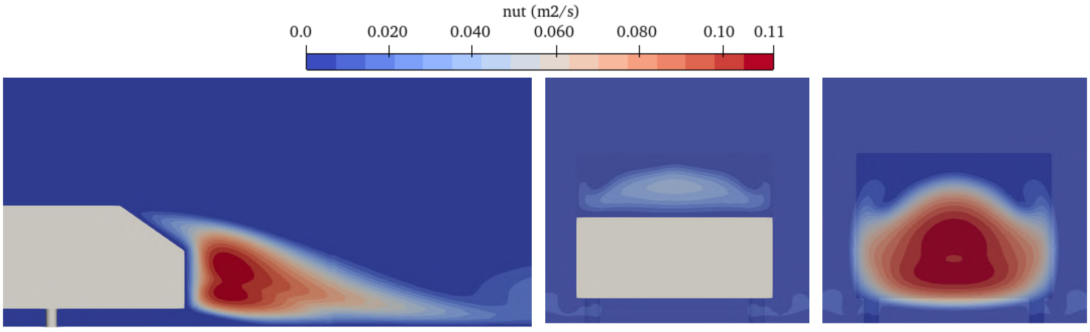

(a) *ν_t contours for RANS/SA.*

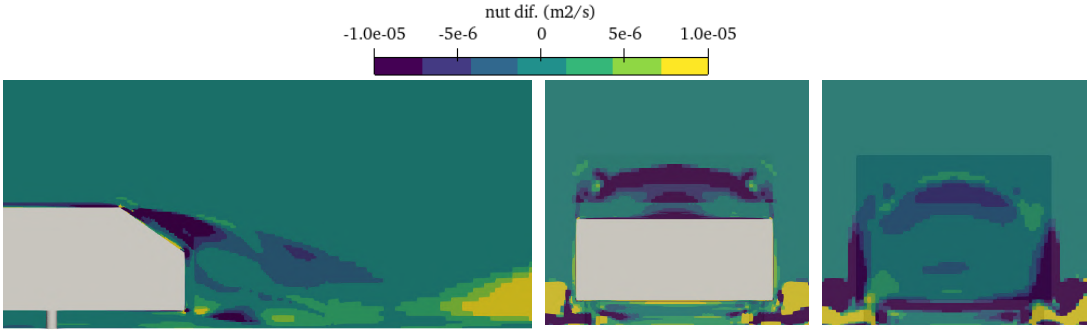

(b) $\Delta\nu_t = \nu_t^{RANS/rEV} - \nu_t^{RANS/SA}$, *for the EVA solution.*

Figure 5.8: *Ahmed body. Contours of ν_t obtained from the intial RANS/SA simulation, and the corresponding correction, $\Delta\nu_t$, after EVA; results are shown on the symmetry plane (left), on a transversal plane located at the rear-end of the body (middle), and* 0.1 *m downstream of the body (right).*

baseline RANS/SA model displays substantial deviations, particularly in the rear-slant region and in the near wake, while the proposed RANS/rEV solution shifts the profiles toward the DES/SA benchmark, achieving an excellent reproduction of the flowfield.

5.2 SAE 20° Notchback Reference Model

While the Ahmed body serves as a standard aerodynamic benchmark, its flow characteristics differ significantly from those of conventional production vehicles. A more realistic representation is the generic vehicle body originally introduced by Cogotti [57] and subsequently adopted by the Society of Automotive Engineers (SAE) to investigate wind-tunnel model interference effects. Commonly referred to as the SAE model, this geometry incorporates various rear-end configurations. In this work, the Notchback variant with a 20° backlight angle is considered, representative of a conventional saloon vehicle featuring a distinct trunk compartment; its schematic is illustrated in Fig. 5.10. Consequently, it exhibits characteristic automotive flow features, such as realistic frontal impingement, A-pillar vortices and a complex flow field across the backlight and boot-deck regions characterized by

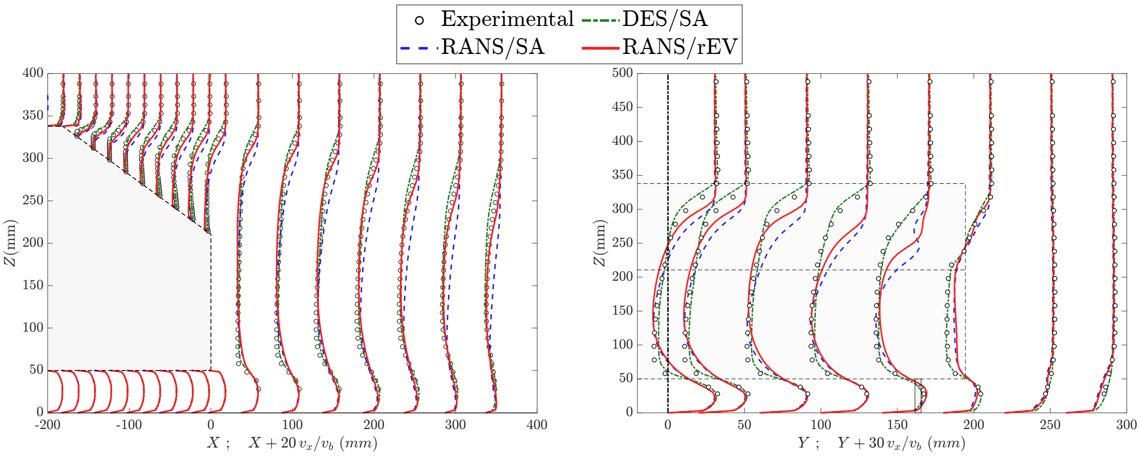

Figure 5.9: *Ahmed body. Mean streamwise velocity profiles for different flowfield solvers; profiles are shown on the symmetry plane (left), and on a transversal plane located* $x = 80\,\mathrm{mm}$ *downstream of the body (bottom).*

localized separation and subsequent reattachment. These characteristics make this geometry a valuable benchmark for the development, assessment, and validation of numerical methodologies.

In the present study, simulations are performed on the 1/5-scale model at an inlet velocity of $v_b = 40$ m/s and zero-yaw angle. The computational domain, shown in Fig. 5.11a, is designed to closely replicate the experimental configuration of Wood et al. [82]. Mesh generation is carried out using the `OpenFOAM` meshing utilities, resulting in a grid comprising ∼1.3 million cells, Fig. 5.11b. An additional refinement region has been added around the notchback section, Fig. 5.11c, to accurately capture the weak separation observed experimentally on the backlight surface and the associated flow displacement above the boot deck [82]. The boundary conditions are identical to those imposed for the Ahmed body simulations in Sec. 5.1. Following a preliminary RANS/SA flow simulation, the average non-dimensional wall distance is $y^+ \sim 90$; the resulted surface distribution of y^+ values is shown in Fig. 5.11d.

The first step in the process is the generation of the Hi-Fi dataset that the EVA methodology aims to match. To this end, a DES/SA simulation was performed for 5 s of physical time, with the final 3 s used for time averaging to obtain the mean flow properties. Throughout the simulation, the Courant number (Co) was maintained below 1 to ensure temporal accuracy. Representative instantaneous contours of the v_x component, are presented in Fig. 5.12.

Fig. 5.13 compares the time-averaged streamwise velocity field and the corresponding streamlines obtained from DES/SA with the PIV measurements of [82] and the RANS/SA solution. The DES/SA results exhibit significantly better agreement with the experimental data, particularly in capturing the shape and extent of the wake lobes behind the vehicle. Furthermore, DES/SA predicts a small recirculation region near the slant surface that is absent in the RANS/SA solution.

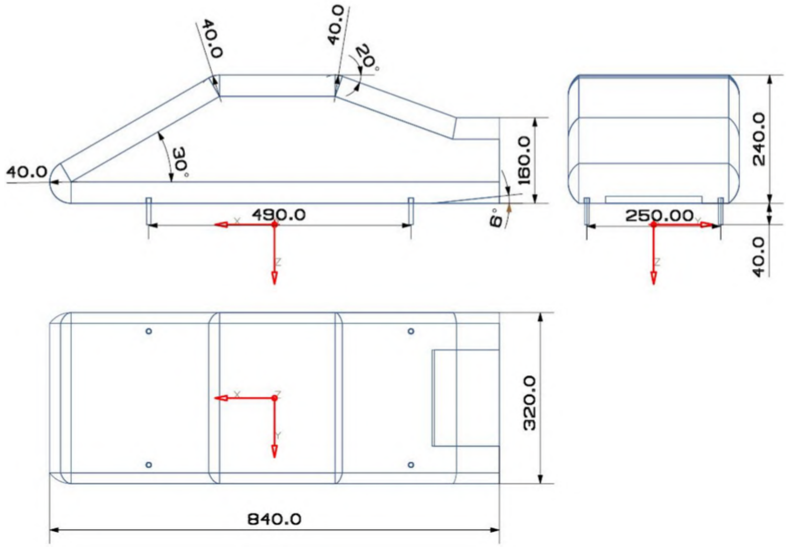

Figure 5.10: *1/5 SAE Notchback geometry (dimensions in millimeters).*

Although this feature cannot be clearly identified in the PIV measurements due to its proximity to the wall, where experimental data is unavailable, its presence is consistent with the improved resolution of the separated flow computed by the DES model.

EVA was subsequently applied starting from the RANS/SA as initialization and executed for a total of 100 cycles, leading to a 46% decrease in the loss function J (Eq. (5.1)). As observed in Fig. 5.13d, the final RANS/rEV solution manages to predict the localized separation in the slant region and to shift the large recirculation zones in the wake towards thE DES/SA results.

A clearer representation of the improved flow field is provided in Fig. 5.14, where vortical structures originating from different regions of the vehicle (as defined in Fig. 5.14a) are identified using the non-dimensional (λ_2) criterion (here, $\lambda_2^* = \lambda_2 \cdot H^2/v_b^2$, where ($H = 0.24$ m denotes the vehicle height):

- In the baseline RANS/SA solution (Fig. 5.14c), the trailing longitudinal vortices generated by the **C-pillars** and **rear edges**, dissipate rapidly, terminating shortly downstream of the vehicle rear-end. In contrast, the RANS/rEV model (Fig. 5.14d) allows these vortex cores to persist significantly further downstream, yielding a wake topology that is in closer agreement with the Hi-Fi DES/SA reference (Fig. 5.14a).
- The RANS/rEV solution successfully captures localized vortical structures associated with the recirculation zone, in the **rear slant** region, a feature that is entirely absent in the baseline RANS/SA prediction.
- RANS.rEV predicts the presence of vortical structures originating from the **underbody**, which are not reproduced by the standard RANS/SA model.
- The development of the **A-pillar** vortices is notably improved. In the RAN-

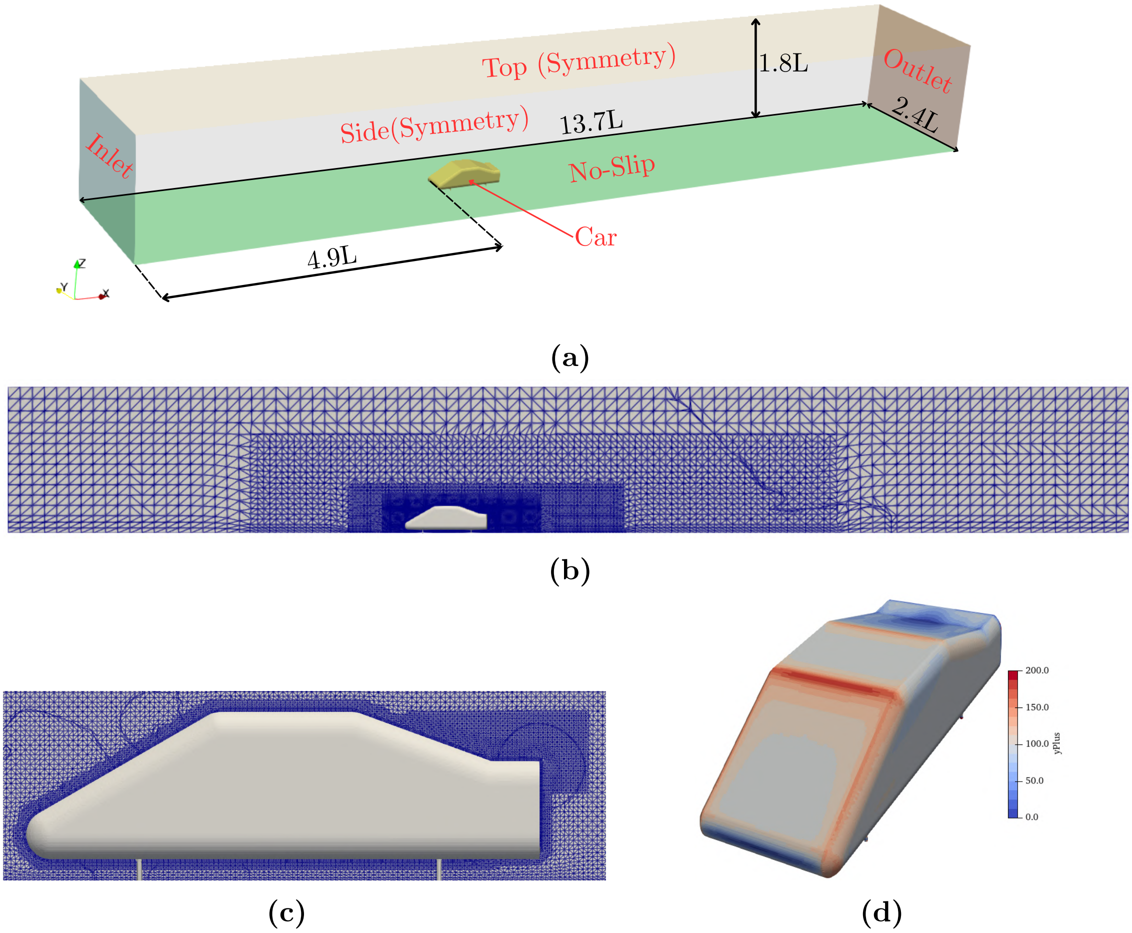

Figure 5.11: *SAE Notchback. (a) Computational domain based on the length $L = 0.84$ m of the car, (b) mesh on the symmetry plane, (c) close-up view of the mesh around the car on the symmetry plane, (d) y^+ distribution on the first near-wall cell over the full-car surface.*

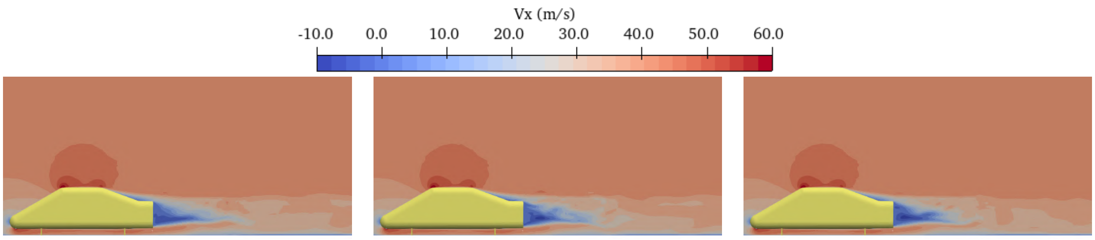

(a) $t = 4.8$ s **(b)** $t = 4.9$ s **(c)** $t = 5.0$ s

Figure 5.12: *SAE Notchback. DES instantaneous streamwise velocity contours on the symmetry plane.*

S/rEV solution, these structures remain coherent and are advected along the vehicle sides rather than dissipating prematurely over the slant, as observed in the RANS/SA case.

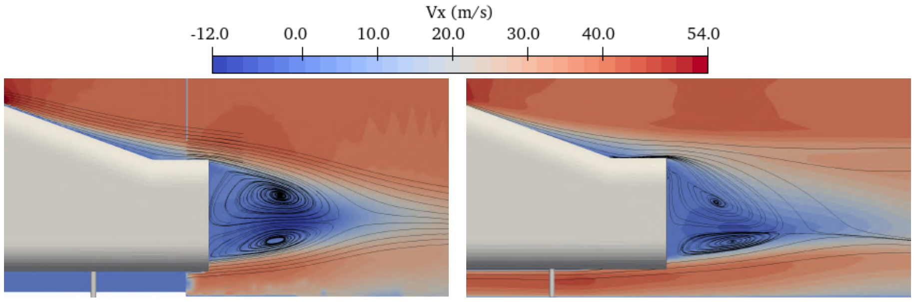

(a) *PIV; adapted from [82]* **(b)** *DES/SA*

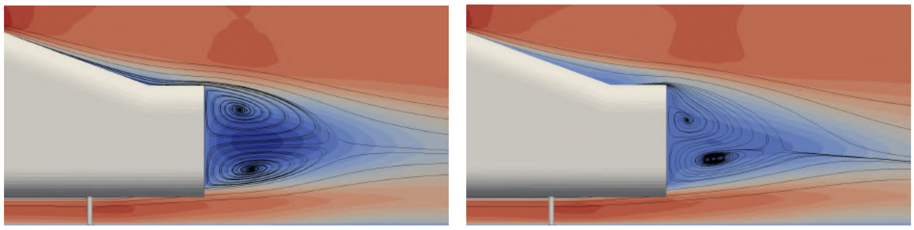

(c) *RANS/SA* **(d)** *RANS/rEV*

Figure 5.13: *SAE Notchback. Mean streamwise velocity contours and streamlines on the symmetry plane near the slant.*

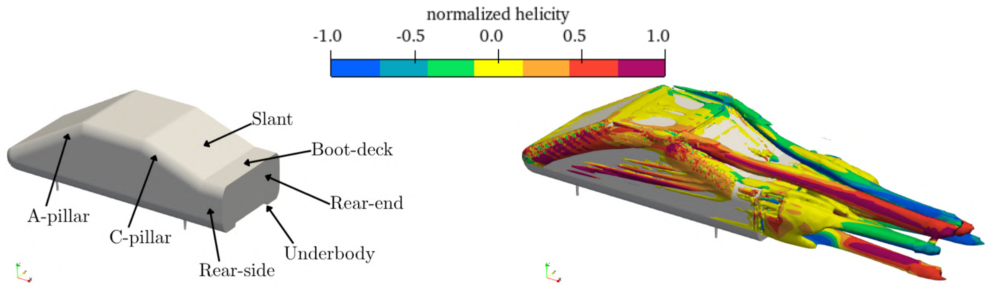

(a) *Car regions* **(b)** *DES/SA*

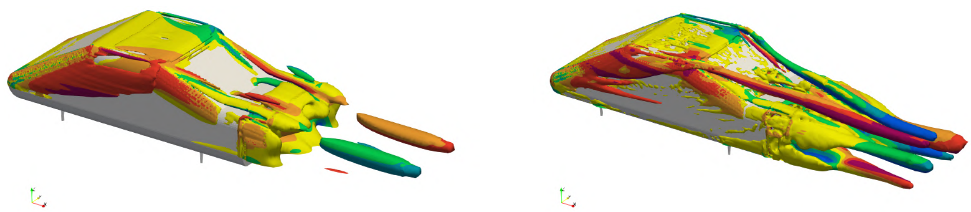

(c) *RANS/SA* **(d)** *RANS/rEV*

Figure 5.14: *SAE Notchback. Iso-surfaces of the non-dimensional λ_2-criterion ($\lambda_2{}^* = -0.1$).*

Overall, the RANS/rEV formulation provides a substantially more accurate representation of the 3D separation mechanisms and overall wake dynamics. This improvement is also reflected in the prediction of the drag coefficient, C_D:

- The experimental value reported by [82] is $C_D^{\text{exp}} = 0.207$.
- The Hi-Fi simulation yielded $C_D^{\text{DES/SA}} = 0.214$, corresponding to a deviation of only 3.4% from the experimental value (under identical test conditions), providing a reliable reference solution.
- The baseline RANS/SA model gives $C_D^{\text{RANS/SA}} = 0.235$, representing a significant overprediction of 9.8% relative to the DES result.
- The final RANS/rEV formulation produced $C_D^{\text{RANS/rEV}} = 0.217$, reducing the discrepancy with the DES/SA reference to less than 1.5%.

Finally, the ν_t field obtained from the baseline RANS/SA simulation, together with the corresponding correction introduced by EVA, is presented in Fig. 5.15. Similar to the Ahmed body case (Fig. 5.8), ν_t is reduced over the slant region, while localized increases are observed mainly near sharp edges.

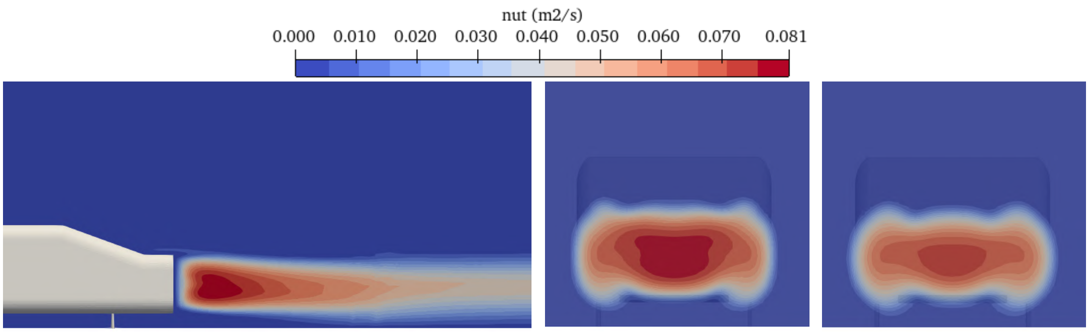

(a) *ν_t contours for RANS/SA.*

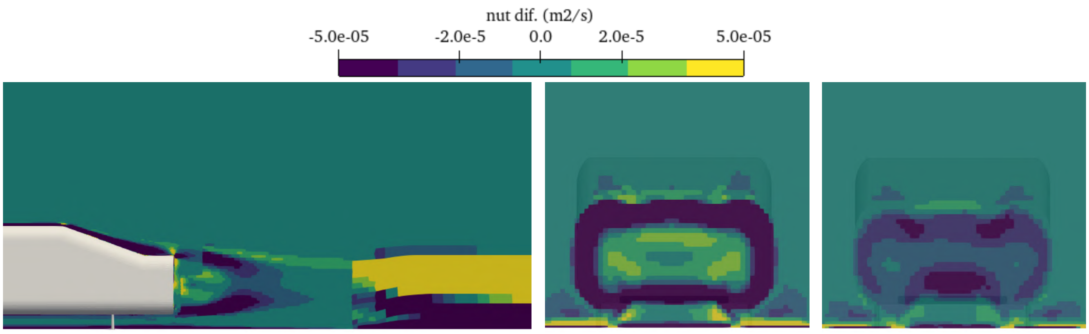

(b) $\Delta\nu_t = \nu_t^{RANS/rEV} - \nu_t^{RANS/SA}$, *for the EVA solution.*

Figure 5.15: *SAE Notchback. Contours of ν_t obtained from the intial RANS/SA simulation, and the corresponding correction, $\Delta\nu_t$, after EVA results are shown on the symmetry plane (left), on a transversal plane located 0.1 m downstream of the body (middle), and 0.2 m downstream of the body (right).*

5.3 DrivAer Without Wheels and Mirrors

The final automotive application considered for the assessment of EVA method is the DrivAer model. This geometry provides a considerably more realistic representation of a passenger vehicle, having been developed through the combination of features from two typical mid-size production cars, namely the Audi A4 and BMW 3 Series [58]. It includes a range of interchangeable components, such as three different rear-end configurations, realistic, smooth, or omitted wheels, underbody detailing of varying complexity, and side mirrors, thereby enabling investigations across a broad spectrum of aerodynamic scenarios [58, 83, 84]. In Fig. 5.16 the main dimensions are presented, along with the available rear-end configurations: Fastback, Notchback, and Estateback. In the present study, only the Fastback and Estateback variants are considered, while furthermore the wheels and mirrors are removed (hereafter denoted as woWwoM) in order to reduce computational cost, particularly regarding the Hi-Fi DES/SA simulations.

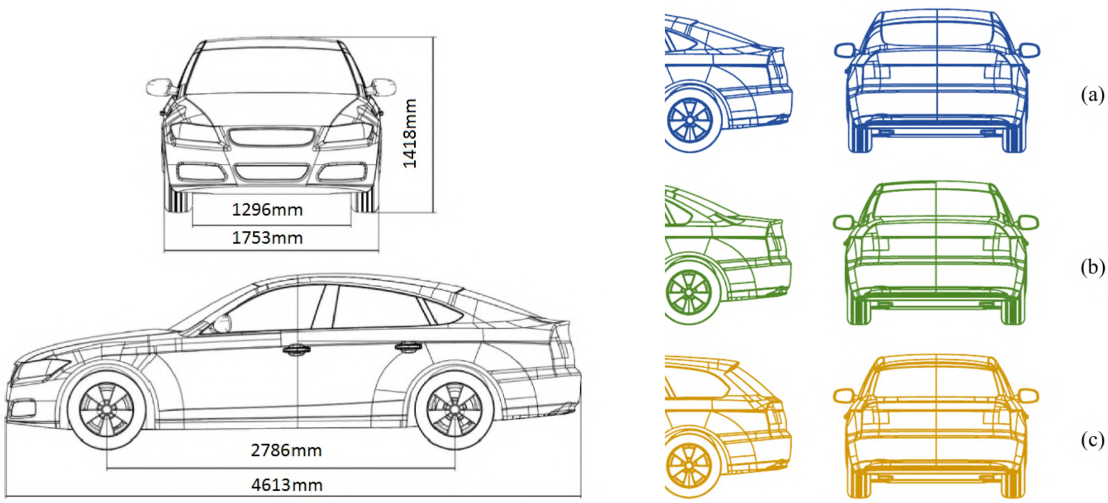

Figure 5.16: *DrivAer geometry; Overall dimensions in millimeters (left), and rear-end variants (right): (a) Fastback, (b) Notchback, (c) Estateback, adapted from [85].*

The flow is simulated within a wind tunnel domain (see Fig. 5.17a), employing the same boundary conditions as in the previous cases, with the exception of the inlet velocity, which is prescribed as $v_x = v_b = 16$ m/s. This value is selected to achieve a Reynolds number of $Re = 4.87 \times 10^6$, based on the total vehicle length $L_c = 4.613$ m.. The computational mesh for the Estateback configuration is shown in Figs. 5.17b and 5.17c and consists of ~ 7.4 M cells. Following a baseline RANS/SA simulation, the resulting average y^+ value is $\sim$55; the corresponding y^+ distribution along the vehicle's surface is presented in Fig. 5.17d.

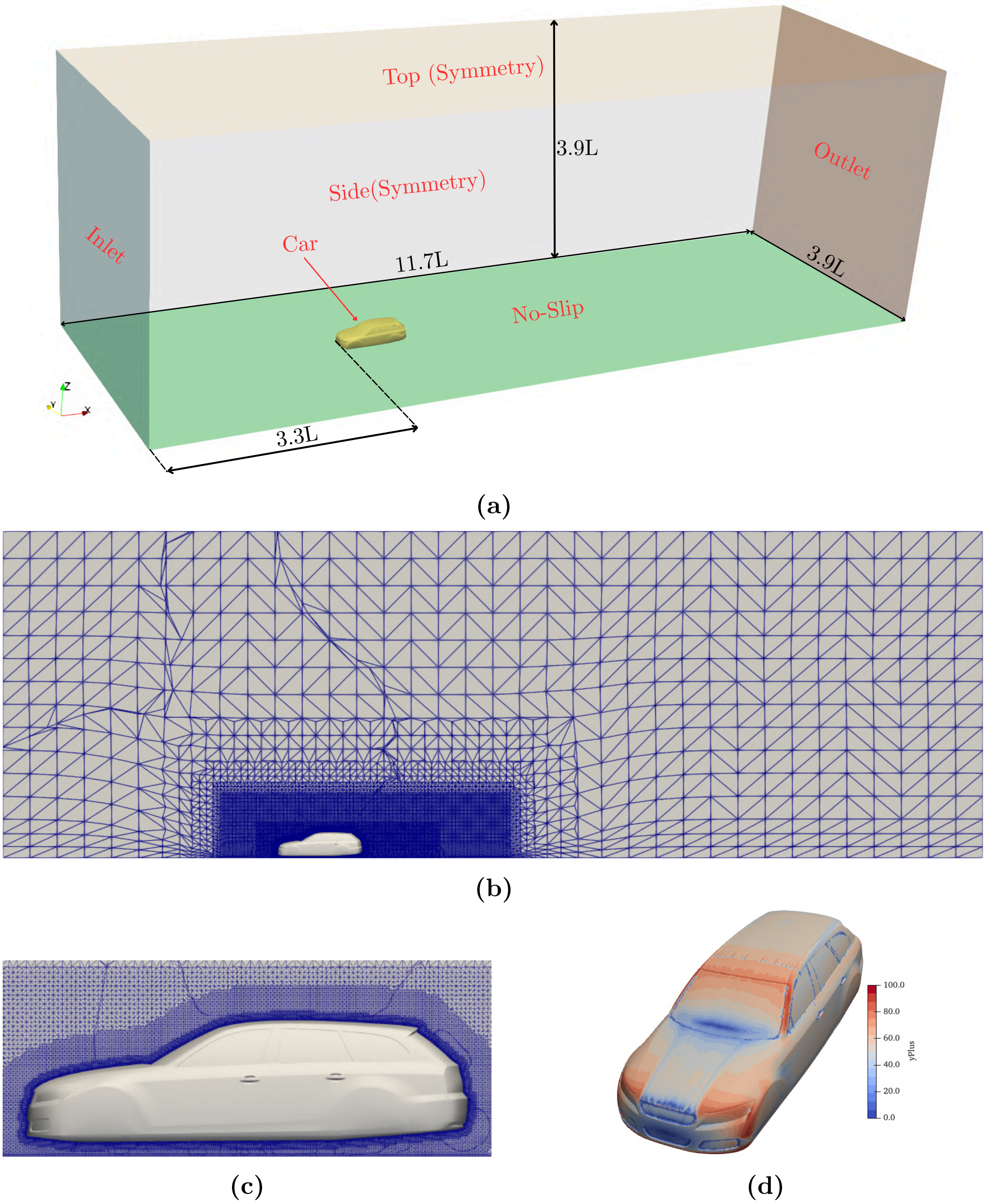

Figure 5.17: *DrivAer Estateback. (a) Computational domain based on the length $L = 4.6$ m of the car, (b) mesh on the symmetry plane, (c) close-up view of the mesh around the car on the symmetry plane, (d) y^+ distribution on the first near-wall cell over the full-car surface.*

The Hi-Fi data were obtained by executing a 6 s DES/SA simulation, averaging the last 4 s; representative velocity contours for the two configurations are presented in Fig. 5.18 and 5.19.

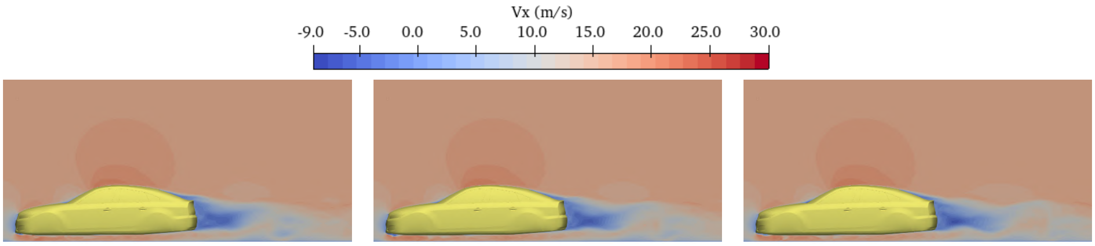

(a) $t = 5.8\ s$ **(b)** $t = 5.9\ s$ **(c)** $t = 6.0\ s$

Figure 5.18: *DrivAer Fastback. DES instantaneous streamwise velocity contours on the symmetry plane.*

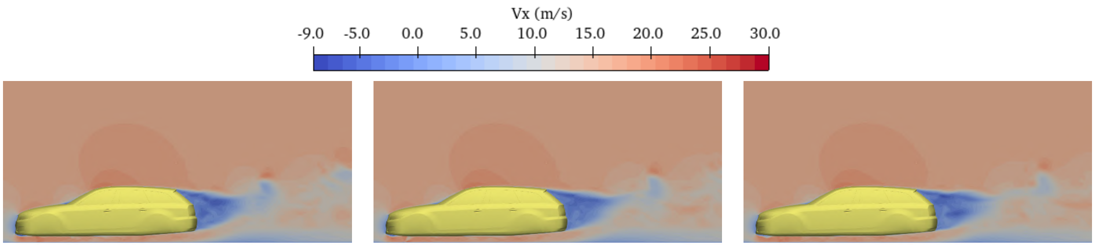

(a) $t = 5.8\ s$ **(b)** $t = 5.9\ s$ **(c)** $t = 6.0\ s$

Figure 5.19: *DrivAer Estateback. DES instantaneous streamwise velocity contours on the symmetry plane.*

5.3.1 Fastback Configuration

For the fastback case, the EVA approach reduces the value of the loss function by 25.6% after 21 cycles. As shown in Figs. 5.20 and 5.21, the resulting streamwise velocity contours and profiles exhibit significantly improved agreement with the DES/SA solution compared to the initial RANS/SA. Furthermore, inspection of the streamlines in Fig. 5.23c indicates that the recirculation bubble forming at the upper rear of the vehicle closely matches the DES/SA benchmark (Fig. 5.20a). Moreover, the incorrect mid-height downstream separation point found in the RANS/SA case (Fig. 5.20b) is eliminated through the application of EVA. Additionally, the EVA-corrected solution exhibits streamlines that are more strongly deflected downward, consistent with the DES/SA behaviour.

In the same figure, the iso-λ_2^* surfaces (non-dimensionalised using the vehicle height $H = 1.418$ m and inlet velocity v_b) showcase a clear weakening of the dominant rear-end longitudinal vortex compared to the RANS/SA solution, closely matching the DES/SA benchmark. Accordingly, the EVA procedure reduces the deviation in drag coefficient relative to DES/SA; specifically, $C_D^{\mathrm{DES/SA}} = 0.113$, while $C_D^{\mathrm{RANS/SA}} = 0.132$ (16.8% difference), and $C_D^{\mathrm{RANS/rEV}} = 0.124$, corresponding

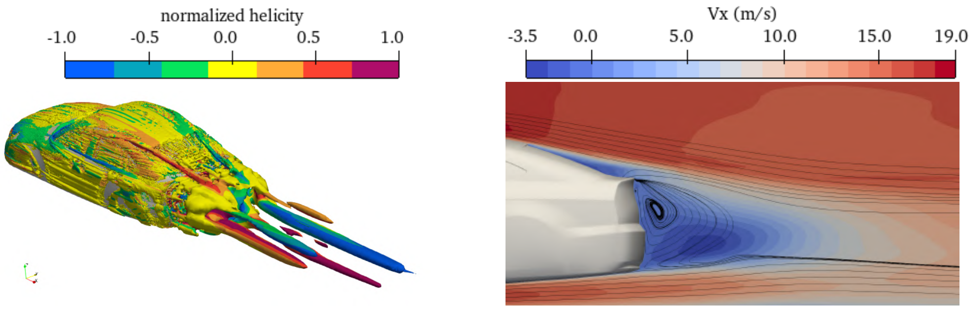

(a) *DES/SA*

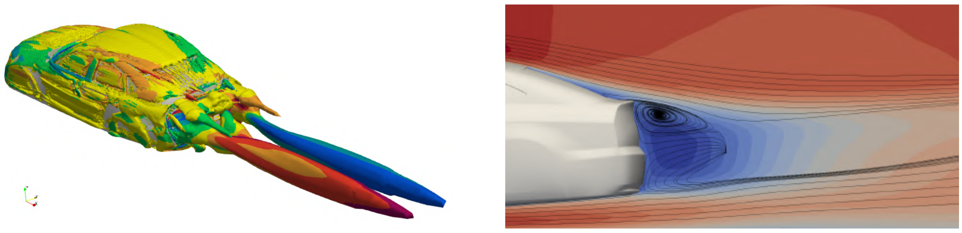

(b) *RANS/SA*

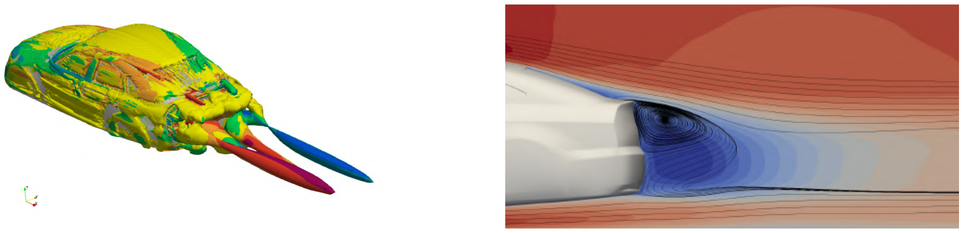

(c) *RANS/rEV*

Figure 5.20: *DrivAer Fastback. Iso-surfaces of the non-dimensional λ_2-criterion ($\lambda_2{}^* = -0.1$) (left), and mean streamwise velocity contours and streamlines on the symmetry plane in the near wake (right).*

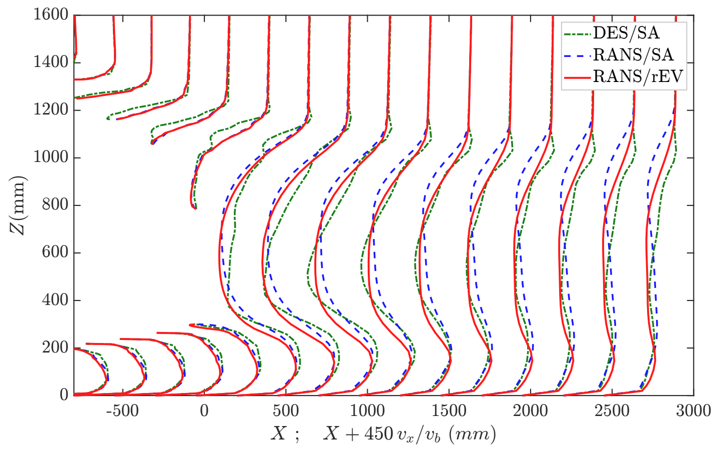

Figure 5.21: *DrivAer Fastback. Mean streamwise velocity profiles for different flowfield solvers; profiles are shown on the symmetry plane.*

to a reduced difference of 9.7% w.r.t. DES/SA. Finally, the initial and corrected turbulent viscosity fields ν_t are presented in Fig. 5.22.

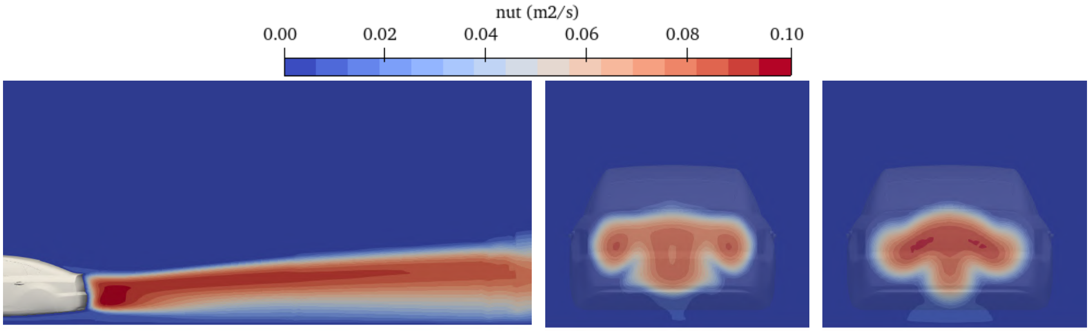

(a) ν_t *contours for RANS/SA.*

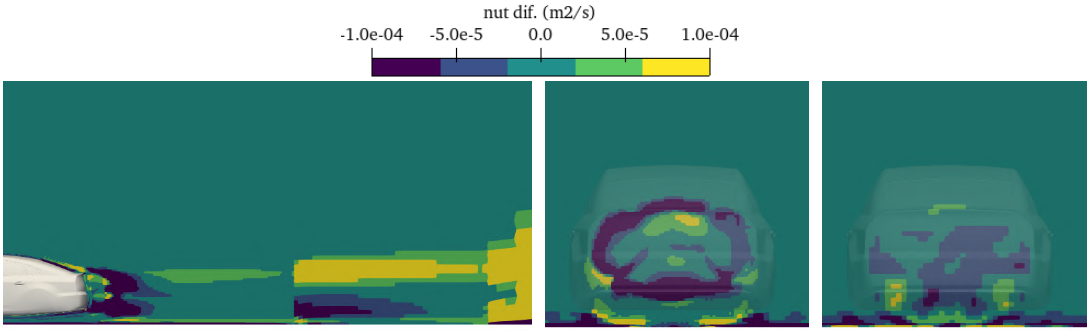

(b) $\Delta\nu_t = \nu_t^{RANS/rEV} - \nu_t^{RANS/SA}$*, for the EVA solution.*

Figure 5.22: *DrivAer Fastback. Contours of* ν_t*, obtained from the intial RANS/SA simulation, and the corresponding correction,* $\Delta\nu_t$*, after EVA, ; results are shown on the symmetry plane (left), on a transversal plane located* 0.2 *m (middle), and* 1.2 *m downstream of the body (right).*

5.3.2 Estateback Configuration

The final case is the DrivAer Estateback woWwoM configuration. Here, J decreases by 17.8% after 37 cycles. Examining the streamwise v_x field in the symmetry plane (Fig. 5.23), EVA is observed to shift the rear lower recirculation zone upstream, closely matching the DES/SA results. Furthermore, the λ_2^* iso-surfaces indicate that the longitudinal vortices in RANS/rEV are reduced in size compared to RANS/SA, consistent with DES/SA behavior. This trend is reflected in the drag coefficient predictions; the discrepancy between DES/SA ($C_D^{\text{DES/SA}} = 0.191$) and the initial RANS/SA solution ($C_D^{\text{RANS/SA}} = 0.210$) is 9.9%, whereas it decreases to only 1.0% for the final RANS/rEV solution ($C_D^{\text{RANS/rEV}} = 0.193$). The initial v_t field and the corresponding correction are provided in Fig. 5.24.

Finally, the comparative C_D results for all models and test cases are summarized in Ta. 5.1.The results demonstrate that the EVA framework, utilizing the

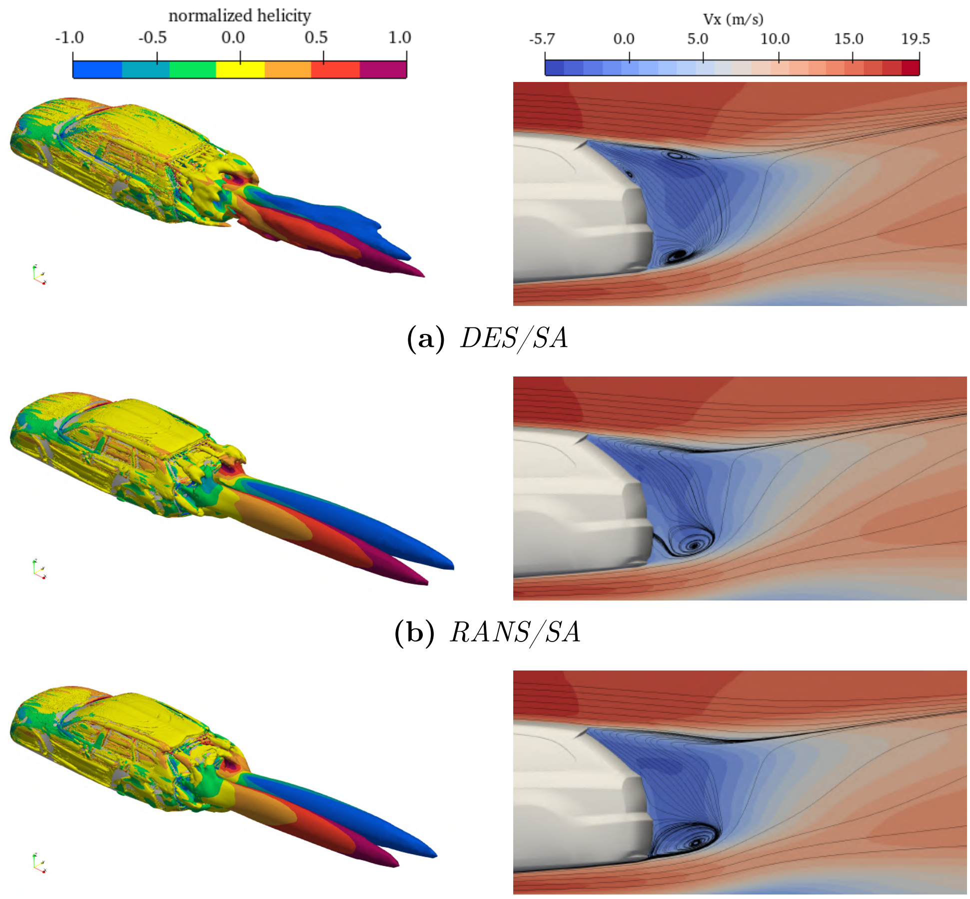

(a) *DES/SA*

(b) *RANS/SA*

(c) *RANS/rEV*

Figure 5.23: *DrivAer Estateback. Iso-surfaces of the non-dimensional λ_2-criterion ($\lambda_2{}^* = -0.2$) (left), and mean streamwise velocity contours and streamlines on the symmetry plane in the near wake (right).*

velocity-based loss function in Eq. (5.1), provides not only a more accurate representation of the Hi-Fi flowfield, but also improved aerodynamic force predictions across various 3D car geometries.

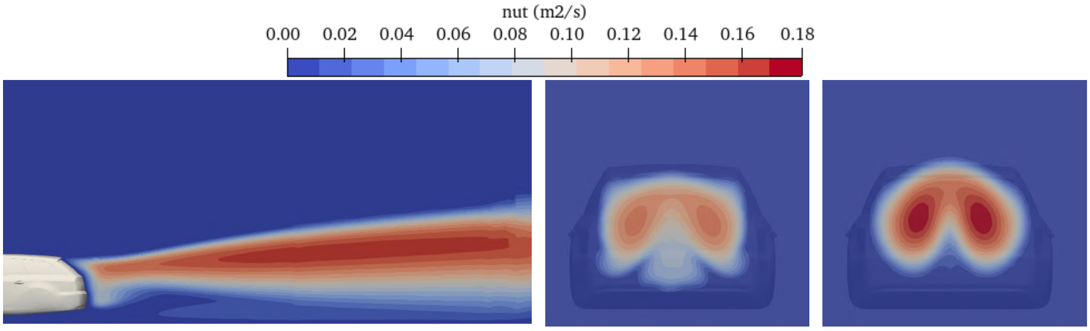

(a) *ν_t contours for RANS/SA.*

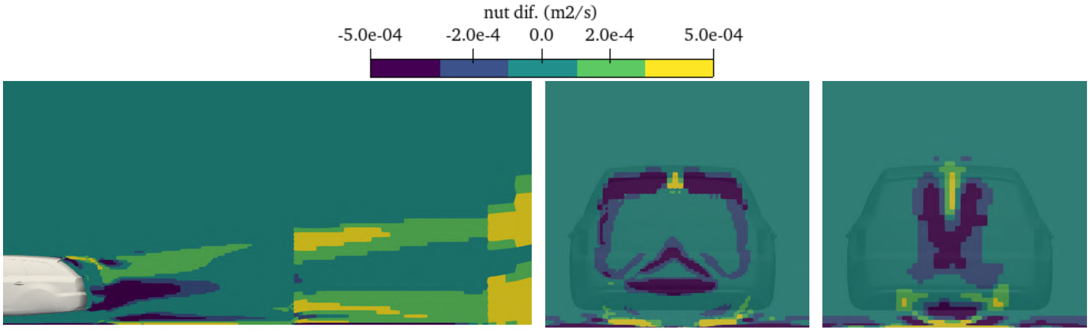

(b) $\Delta\nu_t = \nu_t^{RANS/rEV} - \nu_t^{RANS/SA}$*, for the EVA solution.*

Figure 5.24: *DrivAer Estateback. Contours of ν_t, obtained from the intial RANS/SA simulation, and the corresponding correction, $\Delta\nu_t$, after EVA; results are shown on the symmetry plane (left), on a transversal plane located 0.2 m (middle), and 1.2 m downstream of the body (right).*

Table 5.1: *Comparison of C_D predictions for all cases.*

Case	C_D^{exp}	$C_D^{\text{DES/SA}}$	$C_D^{\text{RANS/SA}}$ / **diff. from DES/SA**	$C_D^{\text{RANS/rEV}}$ / **diff. from DES/SA**
35° slant angle Ahmed body	0.279 [1] [56]	0.306	0.329 (7.5%)	0.302 (-1.3%)
20° 1/5 SAE Notchback	0.207 [82]	0.214	0.235 (9.8%)	0.217 (1.4%)
DrivAer Fastback woWwoM	0.124 [2] [58]	0.113	0.132 (16.8%)	0.124 (9.7%)
DrivAer Estateback woWwoM	0.195 [2] [58]	0.191	0.210 (9.9%)	0.193 (1.0%)

[1]Experimental value corresponds to an inlet velocity of 60 m/s, while CFD simulations were performed at 40 m/s.

[2]Evaluated at the same Re using a 1:2.5 scale model for the experimental setup.

Chapter 6

Ahmed Body Shape Optimization Using EVA/SR

In this chapter, the flowfield correction obtained through the EVA process, is exploited within the ShpO of the 35° slant angle Ahmed bod,y targeting minimization of drag ($F = C_D$). Unlike conventional optimization approaches, where closure is effected by a standard turbulence model, the present work exploits the EVA-corrected ν_t field, to improve the accuracy of the flow predictions. The problem is formulated as a gradient-based optimization case, therefore the Continuous Adjoint Method is employed via the `adjointOptimisationFoam` library in `OpenFOAM`.

As discussed in Sec. 5.1, the flowfield predicted by the RANS/SA model exhibits significant discrepancies, compared to experimental and Hi-Fi DES/SA data, failing to accurately predict the extent of the recirculation region downstream of the body and consequently overestimating the drag coefficient by ∼7.5%. Such deficiencies raise concerns regarding the suitability of the baseline turbulence model within a ShpO routine. Although an optimization process based on the RANS/SA model (fully differentiated in the adjoint equations [86, 51, 49]) may still lead to reduction of the F value, the resulting geometry would be driven by inaccurate flow physics and may not correspond to an optimized design.

To address this limitation, three alternative optimization strategies are investigated by incorporating information from the EVA-corrected ν_t fields. The overall methodology follows the procedure presented in Fig. 1.3:

- **Direct utilization of the EVA-corrected field (RANS/rEV).** The corrected ν_t field, shown in Fig. 5.8, is directly employed in the primal equations using the RANS/rEV solver. In this approach, the ν_t field remains constant throughout the optimization process; both the primal and adjoint equations are solved with a fixed value of the effective viscosity ($\nu_{\text{eff},P} = \nu + \nu_{t,P}$) in each cell P of the domain, and the ν_t field remains unchanged even when the geometry changes during the optimization. Such a method has been employed by Tsolakos [36] for the ShpO of a NACA0012 airfoil, by Alessi [22] for the minimization of pressure losses in a U-bend using EVA, and by Fidkowski [29] for the optimization of 3 airfoils (in the latter, a multiplicative factor applied to the production term of the SA model served as the correction field for FI).
- **Development of a surrogate turbulence model through SR (RANS/cfEV).** A SR procedure is performed with the objective of deriving an analytical, closed-form expression for ν_t, as a function of local flow and ge-

ometrical quantities that reproduces the EVA-corrected ν_t field [53]. The resulting surrogate turbulence model can subsequently be incorporated into the optimization framework in two ways, both of which are introduced herein for the first time in the literature:

◇ **Frozen turbulence in the adjoint equations.** The analytical SR model is used to update the ν_t field at each optimization cycle during the primal solution; however within the adjoint formulation, ν_t is treated as frozen; the sensitivity of ν_t w.r.t. shape modifications is neglected.

◇ **Fully differentiated in the adjoint equations.** The analytical expression obtained through SR is explicitly differentiated, and contributions are introduced into the adjoint equations, thereby accounting for the dependence of ν_t on the flow and geometrical variables during their solution. Previous studies have demonstrated that differentiating conventional turbulence models into the adjoint formulation, leads to more accurate sensitivity derivatives calculation, consistent with the(surrogate) turbulence model and, subsequent, improved optimization performance compared to frozen-turbulence approaches [51, 47].

6.1 Symbolic Regression Implementation

SR is a supervised ML task that, unlike conventional regression methods (e.g., Deep Neural Networks)–which optimize numerical parameters within a fixed, complex, and uninterpretable architecture–searches the space of mathematical operators, variables, and constants to uncover simple, closed-form equations that best describe a dataset [87]. This capability is particularly attractive for data-driven turbulence modeling, as it enables the EVA-corrected ν_t to be represented in analytical form using geometrical and flow quantities, similar to those employed in conventional turbulence models. For this approach to be successful, the closed-form surrogate model embedded in the RANS equations (RANS/cfEV solver), must produce a flowfield that better matches the Hi-Fi solution than the baseline Low-Fi models (e.g., RANS/SA or RANS/k–ω).

In this work, the SR framework is treated as a black box, utilizing the open-source library `PySR` [88]. The implementation for the specific case considered can be found in Batsi's Diploma Thesis [53], along a detailed description of the underlying algorithms and parameter settings. The inputs to the SR model are provided in the form of continuous fields obtained from the EVA solution (Fig. 1.3) and specifically the are:

- **Geometrical features**: the spatial coordinates (x, y, z) of the cell centers in the global system, as well as the distance Δ from the nearest wall, which is commonly used in conventional turbulence models.
- **Flow features**: the velocity components (v_x, v_y, v_z), pressure field p, and the strain-rate S_{ij} and vorticity Ω_{ij} tensors.

All fields are illustrated in Fig. 6.1 and are subsequently normalized prior to being fed into the SR framework. The normalization is performed using the freestream velocity $v_b = 40$ m/s and the total length of the Ahmed body $L = 1044$ mm, as summarized in Tab. 6.1.

Table 6.1: *Normalization of input quantities for the SR procedure.*

Symbol	Normalization	Symbol	Normalization
$\hat{x}$	x/L	$\hat{v}_x$	v_x/v_b
$\hat{y}$	y/L	$\hat{v}_y$	v_y/v_b
$\hat{z}$	z/L	$\hat{v}_z$	v_z/v_b
$\hat{p}$	$p/(0.5 \cdot v_b^2)$	$\hat{\Omega}$	$\Omega_{ij} \cdot L/v_b$
$\hat{S}_{ij}$	$S_{ij} \cdot L/v_b$	$\hat{\Delta}$	Δ/L

The objective of the SR procedure is to minimize the following loss function:

$$F_{\text{loss}} = \frac{1}{N} \sum_{p=1}^{N} (\hat{\nu}_{t_p} - \hat{\nu}_{t_{p,\text{EVA}}})^2 \tag{6.1}$$

where N is the total number of cells in the computational domain, $\hat{\nu}_{t_p}$ is the normalized eddy viscosity in cell p and $\hat{\nu}_{t_{p,\text{EVA}}}$ denotes the corresponding target value from the EVA solution (see Fig. 6.1k). The normalization is based on the following relation:

$$\hat{\nu}_{t_p} = \frac{\nu_{tp} - \nu_t^{\text{min}}}{\nu_t^{\text{max}} - \nu_t^{\text{min}}} \tag{6.2}$$

where ν_{tp} is evaluated using the closed-form expression obtained from the SR model. The normalization limits are set to $\nu_t^{\text{min}} = 0$, consistent with the negligible turbulence viscosity levels sufficiently far from the body, and $\nu_t^{\text{max}} = 0.13$ m^2/s^2. The latter is selected slightly above the maximum value observed in the EVA field, $\max(\nu_t^{\text{EVA}}) = 0.118$ m^2/s^2, in order to allow additional flexibility during SR training.

For the SR model, the set of available binary operators consisted of $+$, $-$, $\times$, and $/$, while the unary operators included exp, log, and $\sqrt{\cdot}$. The SR procedure, implemented via `PySR`, produced closed-form expressions of varying complexity; representative resulting expressions are reported in Tab. 6.2.

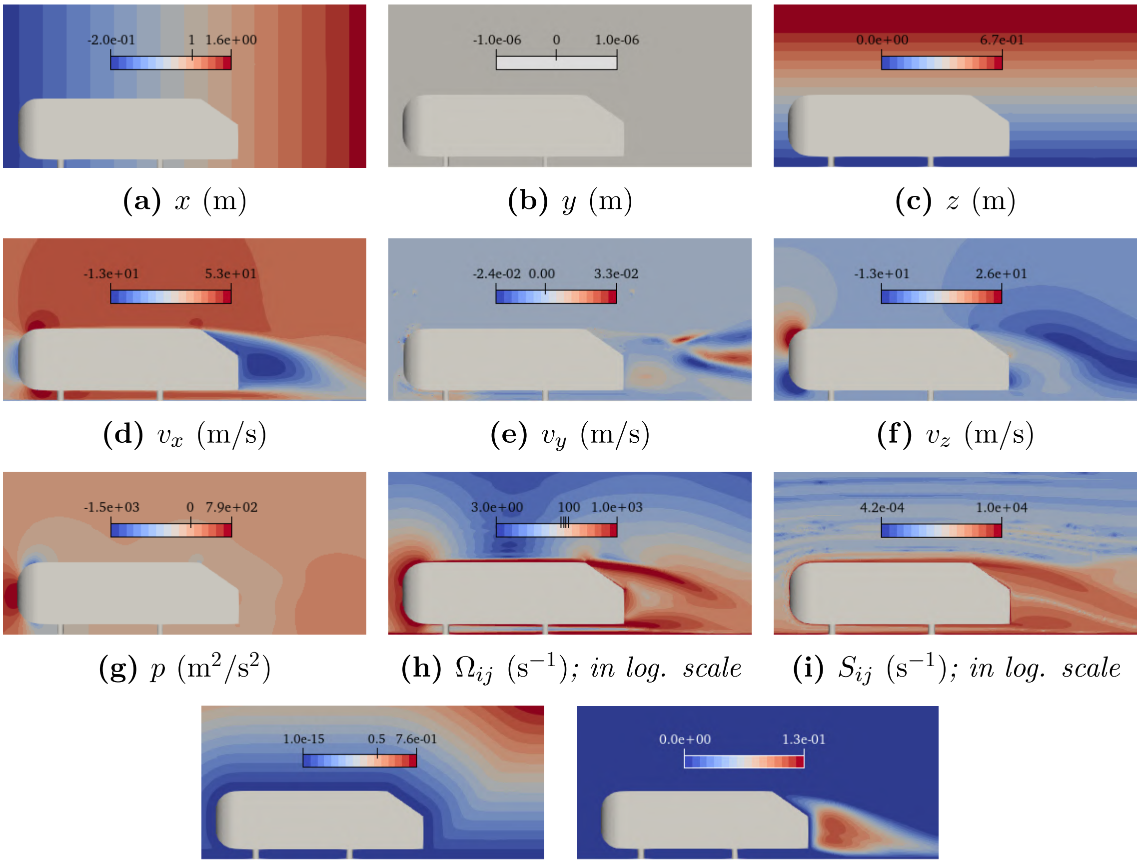

(a) x (m) **(b)** y (m) **(c)** z (m)

(d) v_x (m/s) **(e)** v_y (m/s) **(f)** v_z (m/s)

(g) p ($\mathrm{m}^2/\mathrm{s}^2$) **(h)** Ω_{ij} (s^{-1}); *in log. scale* **(i)** S_{ij} (s^{-1}); *in log. scale*

(j) Δ (m) **(k)** ν_t (m^2/s); *SR aim*

Figure 6.1: *The 10 EVA-derived fields provided as inputs into SR and the ν_t field serving as the target, displayed in the symmetry plane.*

Table 6.2: *Indicative SR-derived surrogate algebraic turbulence models trained on the EVA results.*

Complexity	Loss Function	Equation
5	0.0076437	$\hat{\nu}_t = -0.18852139 \cdot (\hat{v}_x - 1.0577825)$
6	0.0072101	$\hat{\nu}_t = \sqrt{\hat{\Omega}} \cdot \left(\frac{\hat{\Delta}}{0.049802374}\right)$
7	0.0035884	$\hat{\nu}_t = (\hat{v}_x - 1.0012314) \cdot (-5234.8203 \cdot \hat{\Delta})$
12	0.0022985	$\hat{\nu}_t = -66.30894 \cdot \hat{\Delta} \cdot \left(\frac{\hat{v}_x - 0.99205315}{\sqrt{\hat{z}}}\right) + 0.011900872$
17	1.3498e-03	$\hat{\nu}_t = -1.0010344 \cdot (\hat{v}_x - 1.0010344) \cdot \left[\frac{\hat{x} \cdot \hat{\Delta}}{\hat{y}^2 + 0.001325371 \cdot \hat{z}}\right]$
23	9.2413e-04	$\hat{\nu}_t = -4.174718 \cdot \hat{x} \cdot \hat{\Delta} \cdot \left[\frac{\hat{v}_x - 1.0007439}{\left(\frac{\hat{y}^2}{\hat{\Omega} \cdot \hat{z}}\right) + 0.0028072656 \cdot (\hat{\Delta} + \hat{z})}\right]$
27	7.6663e-04	$\hat{\nu}_t = -2.1297116 \cdot \hat{x} \cdot \hat{\Delta} \cdot \left[\frac{(\hat{v}_x - 1.0526726) - 0.48446792 \cdot \hat{v}_z}{\left(\frac{\hat{y}^2}{\hat{z} \cdot \hat{\Omega}}\right) + 0.0015322493 \cdot (\hat{\Delta} + \hat{z})}\right]$

As shown in Tab. 6.2, increasing the complexity of the SR relations reduces the loss function value defined in Eq. (6.1), indicating a better fit to the EVA ν_t data. Most of the expressions, except for the model with complexity 6, utilize v_x, while Ω_{ij} and Δ also appear frequently among the selected input variables.

To assess their performance, the SR relations were implemented within `OpenFOAM`, forming the RANS/cfEV solver. In contrast to conventional turbulence models, ν_t is evaluated directly from the closed-form SR expression, eliminating the need to solve additional turbulence transport equations. The resulting flowfields, obtained after 5,000 iterations and averaged over the final 2,000 (to mitigate convergence difficulties associated with the Ahmed body case), are presented in Fig. 6.2. The coupled RANS/SR simulations reveal that a lower regression loss does not necessarily translate into improved flow predictions. For instance, the near-wake streamlines show that the complexity-17 model (Fig. 6.2f) predicts the recirculation region less accurately than the complexity-12 model (Fig. 6.2e), compared with the RANS/rEV benchmark solution (Fig. 6.2a). This discrepancy can be explained by the corresponding ν_t distributions.

For the lower-complexity models (Figs. 6.2b–6.2d), increasing complexity improves both the ν_t fitting and the resulting v_x field. However, for the complexity-12 model, ν_t within the wake core at the $z = 0.2$ m plane is underpredicted relative to both the complexity-7 model and the RANS/rEV solution, resulting in a less accurate representation of the velocity field despite the lower regression loss. This reduction in SR-loss is primarily achieved through a superior ν_t prediction upstream of the car, where it is estimated closer to zero than in the complexity-7 model, consistent with the RANS/rEV solution. However, this region has a relatively minor influence on the overall flow dynamics compared with even a slightly poorer fit in the wake region. This limitation becomes even more pronounced for the complexity-17 model. Although ν_t is correctly predicted as virtually zero upstream of the car, its downstream distribution is poorly reproduced, causing the recirculation zone above the slant to vanish in the v_x contours. Finally, the higher-complexity models (Figs. 6.2g and 6.2h) successfully recover the wake structure, though they ultimately overpredict ν_t within the wake core.

These findings are further detailed in Tab. 6.3, which reports the performance metrics for each model, including F, quantifying the velocity discrepancy with the Hi-Fi DES/SA data (Eq. (5.1)), and the C_D prediction. Only the complexity-7 model achieves a lower F value than the baseline RANS/SA model, while improved C_D predictions are obtained with models 7, 23, and 27. Since SR-relation 7 outperforms RANS/SA in both metrics and is less complex than the other two candidates, it is selected as the surrogate turbulence model for ShpO.

Finally, Fig. 6.3 compares experimental data, Hi-Fi DES/SA, Low-Fi RANS/SA, EVA-derived RANS/rEV and EVA/SR-derived RANS/cfEV v_x profiles, highlighting the superior performance of the data-driven models over RANS/SA. Notably, the RANS/cfEV results are generally closer to the DES/SA data than the RANS/rEV solution, consistent with the reduced F value shown in Tab. 6.3.

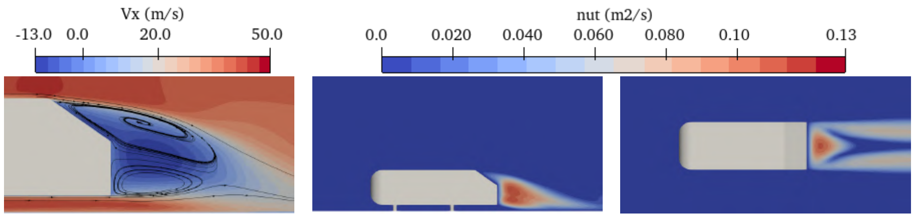

(a) *RANS/rEV*

(b) *RANS/cfEV (complexity 5)*

(c) *RANS/cfEV (complexity 6)*

(d) *RANS/cfEV (complexity 7)*

(e) *RANS/cfEV (complexity 12)*

(f) *RANS/cfEV (complexity 17)*

(g) *RANS/cfEV (complexity 23)*

(h) *RANS/cfEV (complexity 27)*

Figure 6.2: *Fields obtained using different SR-derived surrogate turbulence models; streamwise velocity contours and streamlines in the symmetry plane near the slant (left), ν_t on the symmetry planes (middle), and on a plane at $z = 0.2$ m normal to the ground (right).*

Table 6.3: *Performance comparison of the SR-derived surrogate models.*

Simulation type	F **value (Eq.** (5.1)**)**	**Rel. diff. in** F **(%) from RANS/SA**	C_D	**Rel. error in** C_D **(%) from DES/SA**
DES/SA	—	—	**0.306**	—
RANS/SA	**25.42**	—	0.329	7.5
RANS/rEV	24.27	**-4.5**	0.302	**-1.3**
RANS/cfEV (comp. 5)	72.94	186.9	0.402	31.4
RANS/cfEV (comp. 6)	32.21	26.7	0.347	13.4
RANS/cfEV (comp. 7)	22.66	**-10.9**	0.310	**1.3**
RANS/cfEV (comp. 12)	29.67	16.7	0.329	7.5
RANS/cfEV (comp. 17)	61.04	140.1	0.425	38.9
RANS/cfEV (comp. 23)	27.46	8.0	0.307	**0.3**
RANS/cfEV (comp. 27)	26.88	5.7	0.307	**0.3**

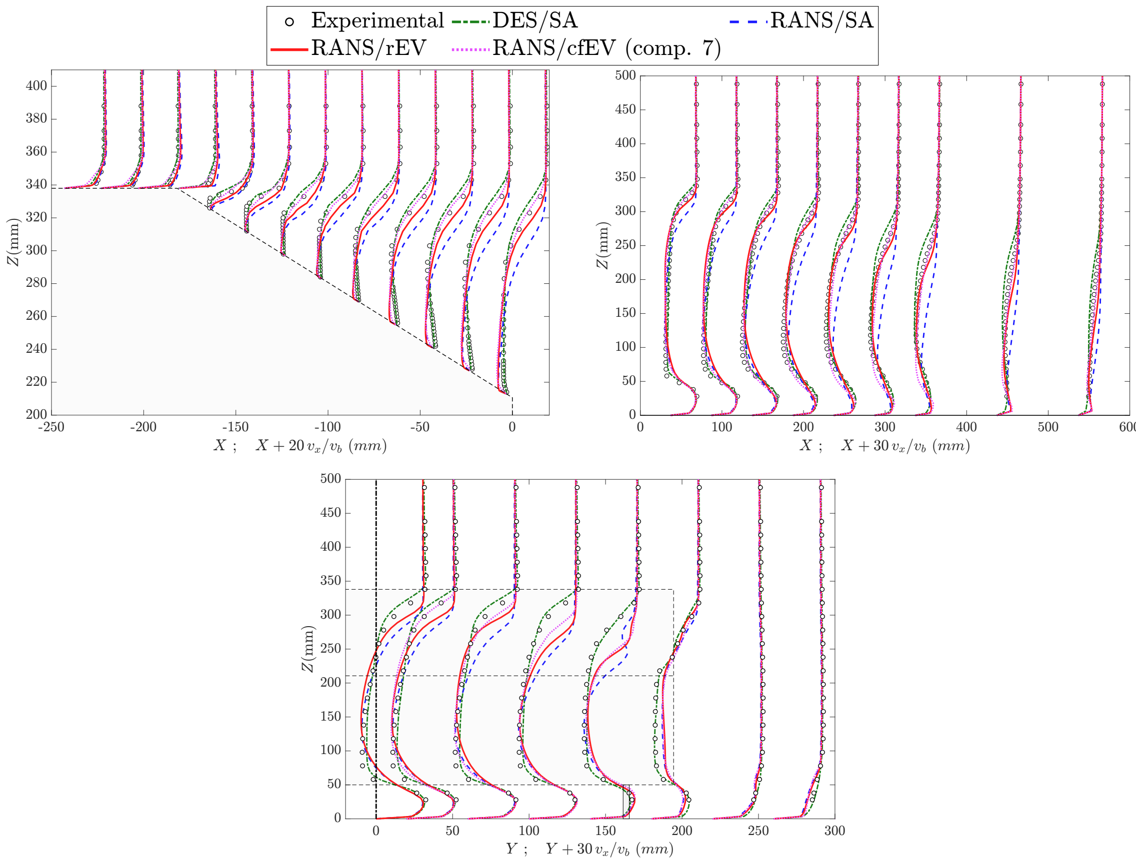

Figure 6.3: *Mean streamwise velocity profiles for different flowfield solvers; profiles are shown on the symmetry plane in the slant region (top left), on the symmetry plane in the wake region (top right), and on a transversal plane located* $x = 80\,\mathrm{mm}$ *downstream of the body (bottom).*

6.2 Differentiation of the SR Relation in the Continuous Adjoint Equations

The closed-form surrogate turbulence model selected in the previous section is obtained by dimensionalizing the relation from Tab. 6.2 based on Tab. 6.1 and Eq. (6.2):

$$\frac{\nu_t - 0}{0.013 - 0} = \left(\frac{v_x}{v_b} - 1.0012314\right) \cdot \left(-5234.8203\frac{\Delta}{L}\right) \Rightarrow \boxed{\nu_t = a_1 \cdot (v_x - a_0) \cdot \Delta} \tag{6.3}$$

where $a_1 = -0.001629613$ and $a_0 = 1.0012314$.

In continuous adjoint formulation, as implemented in the `adjointOptimisationFoam` library of `OpenFOAM`, wall boundaries are classified into two types: fixed walls S_W and parameterized walls S_{W_p}. The latter are defined via volumetric B-spline/NURBS control boxes consisting of control points (CPs), each of which can move in the three spatial directions, thereby deforming the geometry. The positions of the CPs in each direction, serve as the design variables b_n for the optimization problem. Following a similar methodology to the one outlined in Chapter 2, the final expression for the sensitivity derivatives in the adjoint ShpO problem based on the "frozen turbulence assumption" (ν_t const. at each cell during the optimization loop) is formulated as follows, based on [46, 49]:

$$\begin{aligned}
\frac{\delta L}{\delta b_n} &= \int_S \left[u_i v_j n_j + (\nu + \nu_t)\left(\frac{\partial u_i}{\partial x_j} + \frac{\partial u_j}{\partial x_i}\right) n_j - q n_i + \frac{\partial F_{S_k}}{\partial v_i} n_k + \acute{F}^v_{S,i}\right] \frac{\partial v_i}{\partial b_n} dS \\
&+ \int_S \left(u_j n_j + \frac{\partial F_{S_i}}{\partial p} n_i + \acute{F}^p_S\right) \frac{\partial p}{\partial b_n} dS + \int_S \left(-u_i n_j + \frac{\partial F_{S_k}}{\partial \tau_{ij}} n_k\right) \frac{\partial \tau_{ij}}{\partial b_n} dS \\
&+ \int_{S_{W_p}} n_i \frac{\partial F_{S_i}}{\partial x_m} n_m \frac{\delta x_k}{\delta b_n} n_k dS + \int_{S_{W_p}} F_{S_i} \frac{\delta n_i}{\delta b_n} dS + \int_{S_{W_p}} F_{S_i} n_i \frac{\delta (dS)}{\delta b_n} \\
&+ \int_{S_{W_p}} (u_i R^v_i + q R^p + F_\Omega) \frac{\delta x_k}{\delta b_n} n_k dS \\
&+ \int_\Omega \left\{u_j \frac{\partial v_j}{\partial x_i} - \frac{\partial (v_j u_i)}{\partial x_j} - \frac{\partial}{\partial x_j}\left[(\nu + \nu_t)\left(\frac{\partial u_i}{\partial x_j} + \frac{\partial u_j}{\partial x_i}\right)\right] + \frac{\partial q}{\partial x_i} + \acute{F}^v_{\Omega,i}\right\} \frac{\partial v_i}{\partial b_n} d\Omega \\
&+ \int_\Omega \left(-\frac{\partial u_j}{\partial x_j} + \acute{F}^p_\Omega\right) \frac{\partial p}{\partial b_n} d\Omega
\end{aligned} \tag{6.4}$$

where the objective function F, which comprises both surface and volume integrals, is written as:

$$F = \int_S F_S dS + \int_\Omega F_\Omega d\Omega \tag{6.5}$$

In general, F may depend on the primal flow variables v_i and p, as well as their differential operators (such as the stress tensor). For this reason, evaluating $\partial F_\Omega / \partial b_n$

using a simple chain rule w.r.t $v_i,\ p$ is avoided. Instead, the expression:

$$\int_\Omega \frac{\partial F_\Omega}{\partial b_n} d\Omega = \int_\Omega \acute{F}^v_{\Omega,i} \frac{\partial v_i}{\partial b_n} d\Omega + \int_\Omega \acute{F}^p_\Omega \frac{\partial p}{\partial b_n} d\Omega + \int_S \acute{F}^v_{S,i} \frac{\partial v_i}{\partial b_n} dS + \int_S \acute{F}^p_S \frac{\partial p}{\partial b_n} dS \quad (6.6)$$

is used, where $\acute{F}^\Phi_\Omega$ includes the partial derivative $\partial F_\Omega/\partial\Phi$ plus any term that might result from the use of the Gauss divergence theorem for integrals of the form $\int_\Omega \frac{\partial}{\partial b_n}\left(\frac{\partial \Phi}{\partial x_j}\right) d\Omega$ [49].

Compared to Eq. (2.30) in Chapter 2, Eq. (6.4) includes surface integrals over the parameterized walls and additional terms arising from the differentiation of the general objective function F. It also omits the term: $\int_\Omega \frac{\partial u_i}{\partial x_j}\frac{\partial \nu_t}{\partial \nu_{tp}}\left(\frac{\partial v_i}{\partial x_j}+\frac{\partial v_j}{\partial x_i}\right) d\Omega$, since ν_t is no longer dependent on b_n. The last two volume integrals in Eq. (6.4) are set to to zero, giving the adjoint mean flow equations $R^q = 0,\ R^u_i = 0$.

However, as shown in Eq. (6.3), $\nu_t = f(v_x, \Delta)$ and new terms should be added in Eq. (6.4). The difference with the "frozen turbulence" formulation, arises when differentiating the momentum equations w.r.t. b_n:

$$\begin{aligned}\int_\Omega u_i \frac{\partial R^v_i}{\partial b_n} d\Omega = & \underbrace{\int_\Omega u_i \frac{\partial v_j}{\partial b_n}\frac{\partial v_i}{\partial x_j} d\Omega}_{(1)} + \underbrace{\int_\Omega u_i v_j \frac{\partial}{\partial x_j}\left(\frac{\partial v_i}{\partial b_n}\right) d\Omega}_{(2)} + \underbrace{\int_\Omega u_i \frac{\partial}{\partial x_i}\left(\frac{\partial p}{\partial b_n}\right) d\Omega}_{(3)} \\ & - \underbrace{\int_\Omega u_i \frac{\partial}{\partial x_j}\left[(\nu+\nu_t)\frac{\partial}{\partial b_n}\left(\frac{\partial v_i}{\partial x_j}+\frac{\partial v_j}{\partial x_i}\right)\right] d\Omega}_{(4)} \\ & - \underbrace{\int_\Omega u_i \frac{\partial}{\partial x_j}\left[\frac{\partial(\nu+\nu_t)}{\partial b_n}\left(\frac{\partial v_i}{\partial x_j}+\frac{\partial v_j}{\partial x_i}\right)\right] d\Omega}_{(5)} \end{aligned} \quad (6.7)$$

with terms (1) and (2) analyzed analogously to Eq. (2.24) (replacing ν_{tp} with b_n), and term (3) treated as in Eq. (2.27). For the other two terms, further analysis is required.

Calculation of term (4) in Eq. (6.7)

$$(4) = -\int_S u_i n_j (\nu+\nu_t)\frac{\partial}{\partial b_n}\left(\frac{\partial v_i}{\partial x_j}+\frac{\partial v_j}{\partial x_i}\right) dS + \underbrace{\int_\Omega \frac{\partial u_i}{\partial x_j}(\nu+\nu_t)\frac{\partial}{\partial b_n}\left(\frac{\partial v_i}{\partial x_j}+\frac{\partial v_j}{\partial x_i}\right) d\Omega}_{t_2} \quad (6.8)$$

with the last term t_2 further analyzed as:

$$t_2 = \int_\Omega \frac{\partial u_i}{\partial x_j}(\nu+\nu_t)\frac{\partial}{\partial x_j}\left(\frac{\partial v_i}{\partial b_n}\right) d\Omega + \int_\Omega \frac{\partial u_i}{\partial x_j}(\nu+\nu_t)\frac{\partial}{\partial x_i}\left(\frac{\partial v_j}{\partial b_n}\right) d\Omega$$

$$
\begin{aligned}
&= \left[\int_S (\nu+\nu_t) \frac{\partial u_i}{\partial x_j} \frac{\partial v_i}{\partial b_n} n_j dS - \int_\Omega \frac{\partial}{\partial x_j} \left((\nu+\nu_t) \frac{\partial u_i}{\partial x_j} \right) \frac{\partial v_i}{\partial b_n} d\Omega \right] \\
&\quad + \left[\int_S (\nu+\nu_t) \frac{\partial u_i}{\partial x_j} \frac{\partial v_j}{\partial b_n} n_i dS - \int_\Omega \frac{\partial}{\partial x_i} \left((\nu+\nu_t) \frac{\partial u_i}{\partial x_j} \right) \frac{\partial v_j}{\partial b_n} d\Omega \right] \\
&= \int_S (\nu+\nu_t) \left(\frac{\partial u_i}{\partial x_j} + \frac{\partial u_j}{\partial x_i} \right) \frac{\partial v_i}{\partial b_n} n_j dS \\
&\quad - \int_\Omega \frac{\partial}{\partial x_j} \left((\nu+\nu_t) \left(\frac{\partial u_i}{\partial x_j} + \frac{\partial u_j}{\partial x_i} \right) \right) \frac{\partial v_i}{\partial b_n} d\Omega
\end{aligned} \tag{6.9}
$$

which is essentially Eq. (2.26) with the sole exception of the missing term $\int_\Omega \frac{\partial u_i}{\partial x_j} \frac{\partial \nu_t}{\partial \nu_{tp}} \left(\frac{\partial v_i}{\partial x_j} + \frac{\partial v_j}{\partial x_i} \right) d\Omega$.

Calculation of term (5) in Eq. (6.7) This term arises from the differentiation of ν_t. Since ν_t depends only on v_x (Eq. (6.3)) among the flow variables, the term vanishes for $i = 2, 3$. Only for $i = 1$ (the streamwise direction) does the term contribute, yielding:

$$
\begin{aligned}
(5) &\underset{v_1 = v_x}{\overset{i=1}{=}} \int_\Omega u_i \frac{\partial}{\partial x_j} \left[\frac{\partial}{\partial b_n} \left(\nu + a_1 (v_i - a_0) \Delta \right) \left(\frac{\partial v_i}{\partial x_j} + \frac{\partial v_j}{\partial x_i} \right) \right] d\Omega \\
&= \int_S u_i \left(\frac{\partial v_i}{\partial x_j} + \frac{\partial v_j}{\partial x_i} \right) a_1 \Delta n_j \frac{\partial v_i}{\partial b_n} dS \\
&\quad + \int_\Omega \underline{\frac{\partial u_i}{\partial x_j} \left(\frac{\partial v_i}{\partial x_j} + \frac{\partial v_j}{\partial x_i} \right) a_1 \Delta} \frac{\partial v_i}{\partial b_n} d\Omega
\end{aligned} \tag{6.10}
$$

with both terms added to the sensitivity derivative expression in Eq. (6.4). The first term on the right-hand side vanishes after the introduction of the ABCs, while the second one, corresponds to the **extra term arising in the adjoint momentum equation** R_1^u.

Influence in the Eikonal Equation During ShpO, the displacement of the parameterized wall boundaries causes the wall-distance field to vary at each optimization cycle, necessitating an efficient recomputation method. Consequently, the Δ field is obtained by solving a reformulated Eikonal equation [49]:

$$
R^\Delta = \frac{\partial (c_j \Delta)}{\partial x_j} - \Delta \frac{\partial^2 \Delta}{\partial x_j^2} - 1 = 0 \tag{6.11}
$$

where $c_j = \partial \Delta / \partial x_j$ denotes the components of a "convecting velocity" term. Eq. (6.11) is also known as the Hamilton–Jacobi equation and consists of non-linear convection and diffusion terms; a zero Dirichlet condition is imposed on solid walls, while on the remaining boundaries the condition $\frac{\partial \Delta}{\partial x_i} n_i = 1$ is applied [49]. To account for this geometric dependence within the continuous adjoint framework, the augmented objective function relation from Eq. (2.1) is extended:

$$L = F + \int_\Omega u_i R_i^v d\Omega + \int_\Omega q R^p d\Omega + \int_\Omega \Delta_a R^\Delta d\Omega \tag{6.12}$$

where Δ_a is the adjoint wall distance field.

Since the state unknowns include $\{v_i, p, \Delta\}$, the variation of term (5) in Eq. (6.7) must account for the dependence of ν_t on Δ [Eq. (6.3)]. This yields:

$$\begin{aligned}
(5) =& \int_\Omega u_i \frac{\partial}{\partial x_j}\left[\frac{\partial}{\partial b_n}\left(\nu + a_1(v_1 - a_0)\Delta\right)\left(\frac{\partial v_i}{\partial x_j} + \frac{\partial v_j}{\partial x_i}\right)\right] d\Omega \\
=& \int_S u_i \left(\frac{\partial v_i}{\partial x_j} + \frac{\partial v_j}{\partial x_i}\right) a_1 \Delta n_j \frac{\partial v_i}{\partial b_n}\delta_{i1} dS + \int_S u_i \left(\frac{\partial v_i}{\partial x_j} + \frac{\partial v_j}{\partial x_i}\right) a_1(v_1 - a_0) n_j \frac{\partial \Delta}{\partial b_n} dS \\
&+ \int_\Omega \underbrace{\frac{\partial u_i}{\partial x_j}\left(\frac{\partial v_i}{\partial x_j} + \frac{\partial v_j}{\partial x_i}\right) a_1 \Delta}_{\text{to } R_1^u} \frac{\partial v_i}{\partial b_n}\delta_{i1} d\Omega \\
&+ \int_\Omega \underbrace{\frac{\partial u_i}{\partial x_j}\left(\frac{\partial v_i}{\partial x_j} + \frac{\partial v_j}{\partial x_i}\right) a_1 (v_1 - a_0)}_{\text{to } R^{\Delta_a}} \frac{\partial \Delta}{\partial b_n} d\Omega
\end{aligned} \tag{6.13}$$

the second term in the r.h.s. is neglected after the introduction of the ABCs into the sensitivity derivative relation, while **the last integral term is added in the adjoint wall distance equation** R^{Δ_a}. A detailed analysis of the continuous adjoint formulation for the distance field, alongside its impact on the sensitivity derivatives, lies beyond the scope of this work and can be found in [49]. For completeness, the final adjoint distance equation R^{Δ_a} is provided for the specific case:

$$R^{\Delta_a} = -2\frac{\partial}{\partial x_j}\left(\Delta_a \frac{\partial \Delta}{\partial x_j}\right) + \frac{\partial u_i}{\partial x_j}\left(\frac{\partial v_i}{\partial x_j} + \frac{\partial v_j}{\partial x_i}\right) a_1(v_1 - a_0) = 0 \tag{6.14}$$

where the first term originates from the differentiation of the primal Eikonal equation (Eq. (6.11)), and the second one arises from the differentiation of the surrogate turbulence model (Eq. (6.3)) within the momentum equations (Eq. (6.7)). Together with the source term introduced in the adjoint momentum equation R_1^u in Eq. (6.13), these contributions fully close the dependencies of the ν_t field within the continuous adjoint framework.

6.3 ShpO using Surrogate Turbulence Models

The first step of the ShpO routine is the parameterization of the geometry. Specifically for the Ahmed Body case, two Cartesian NURBS boxes are defined around the upper and lower regions of the slant (Fig. 6.4), while the intermediate region, corresponding to a rear window, remains unchanged. Each morphing box consists of a structured lattice of CPs; 7 points in the streamwise (x), 12 in the spanwise (y), and 5 in the vertical (z) direction, yielding a total of 420 CPs per box. The boundary CPs remain still in all directions. In addition, the second rows of CPs at both the upstream and downstream ends in the x direction are fixed to ensure second-order streamwise geometric continuity. Furthermore, the displacement of all CPs in the y direction is confined, and CPs belonging to the same spanwise line are constrained to undergo identical displacements, thereby ensuring smooth deformation and a manufacturable final geometry. The resulting geometric deformation is subsequently propagated to the computational mesh using the `dynamicMesh` utility of `OpenFOAM`. Further details on the parameterization and mesh movement procedure can be found in [45].

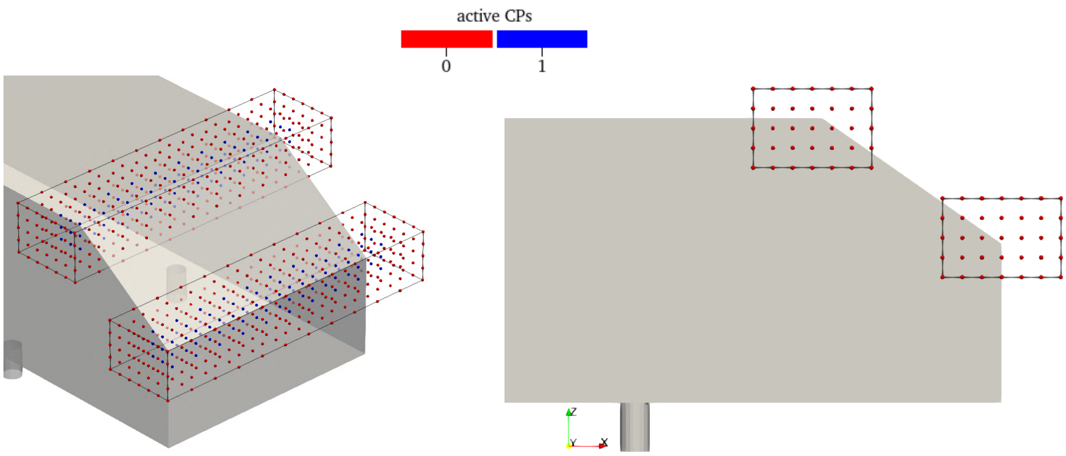

Figure 6.4: *NURBS boxes on the upper and lower regions of the slant for shape parametrization; CPs are fixed along the y-direction.*

All simulations were performed using the `adjointOptimisationFoam` library within `OpenFOAM`. The objective function was defined as $F = C_D$ of the Ahmed body. In each optimization cycle, 5,000 iterations of the primal problem were performed and the flowfields were averaged over the final 2,000 iterations before being passed to the adjoint solver; a similar averaging procedure was applied to the adjoint fields. Sensitivity derivatives were updated using a conjugate gradient method [89], with the step size η selected such that the maximum displacement of the control points during the first cycle was limited to 0.001 m.

For the RANS/rEV and RANS/cfEV models, only 2 ShpO cycles were performed, since the EVA model (and in the latter case, also the SR correction) was trained exclusively on the baseline geometry. Consequently, the models cannot be trusted for large geometric displacements. Conversely, the optimization employing the RANS/SA solver was extended to 4 cycles; as it is a standard turbulence model, possessing global validity and not being restricted to a specific geometry. Subsequently, the resulting geometries from the various ShpO routines are evaluated using the Hi-Fi DES/SA solver (with the flowfields averaged over the final 3 s of a 5 s simulation), which as demonstrated in Fig. 5.9, closely matches the experimental data, thereby it is considered as the ground truth. This re-evaluation ultimately assess the true efficacy of the ShpO achieved by each candidate model.

The optimized geometries are illustrated in Fig. 6.5. As expected for drag minimization, all frameworks tend to generate a spoiler-like feature along the upper slant region; however, the resulting profiles differ substantially depending on the model utilized. The frameworks employing the frozen-adjoint approach (RANS/rEV and RANS/cfEV) displace the geometry upward near the edge tip. Conversely, the solvers utilizing the differentiated adjoint formulation (RANS/SA and RANS/cfEV) shift the profile upstream of the slant's leading edge inward. Notably, the RANS/rEV model yields the largest overall geometric deformation. Along the lower region of the slant, all solvers move the geometry inward, with the differentiated RANS/cfEV and RANS/SA models exhibiting more pronounced displacements than the frozen-adjoint variants. The deformation direction and magnitude are both detailed in Fig. 6.6, along with their corresponding Low- and Hi-Fi flowfields.

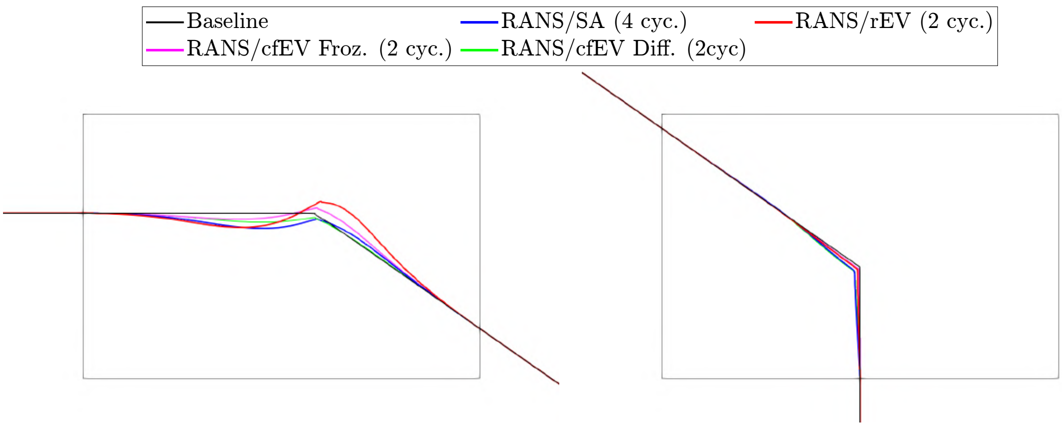

Figure 6.5: *Final geometries of the upper (left), and lower (right) slant for different flowfield solvers, including the corresponding NURBS box boundaries.*

The v_x contours and streamlines presented in Fig. 6.6b reveal substantial differences between the Low- and Hi-Fi solvers; while the former predicts a localized recirculation zone confined near the rear-end of the car, the latter reveals a large separation bubble covering the entire slant region. This discrepancy indicates that the frozen EVA-derived ν_t field is incapable of accurately reproducing the flow behavior, even for this relative small geometry change. Similar differences are evident in Fig. 6.6c, particularly regarding the extent of the low-velocity wake region, which is significantly larger in the DES/SA re-evaluation. Conversely, the framework employing the differentiated RANS/cfEV model (Fig. 6.6d) yields a closer agreement with the Hi-Fi results.

Finally, a comparison of all C_D predictions is provided in Tab. 6.4. The main observations for each solver are summarized below:

(a) The **RANS/SA** framework effectively decreases the F value from 0.329

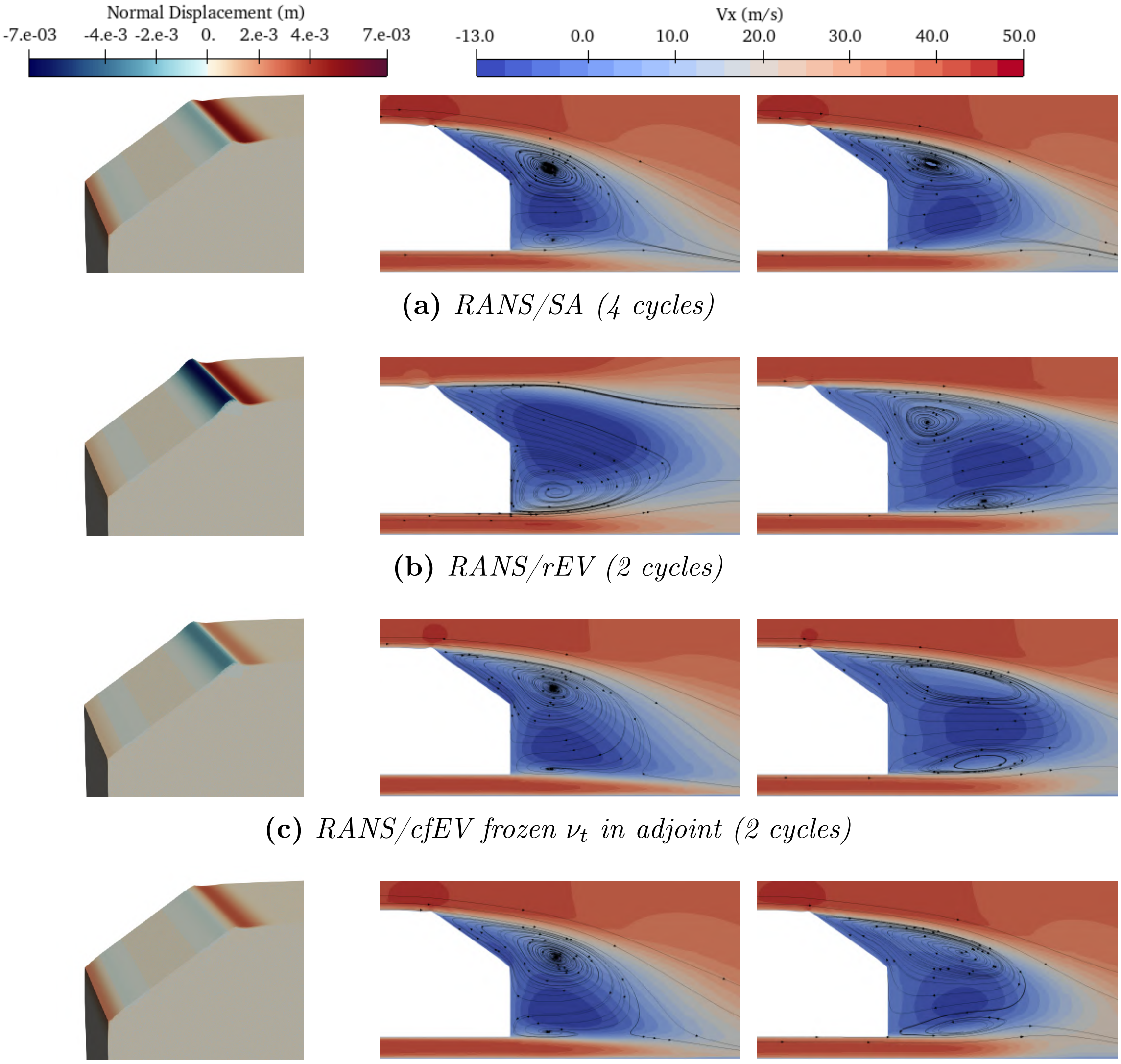

(a) *RANS/SA (4 cycles)*

(b) *RANS/rEV (2 cycles)*

(c) *RANS/cfEV frozen ν_t in adjoint (2 cycles)*

(d) *RANS/cfEV differentiated in adjoint (2 cycles)*

Figure 6.6: *Comparison of different ShpO routines: final geometries and displacements relative to the initial shape (left), streamwise velocity contours and streamlines predicted by the corresponding solver on the symmetry plane, and the reevaluation using the Hi-Fi DES/SA solver.*

to 0.326 over 4 cycles. Hi-Fi re-evaluation confirms this trend, with the true C_D dropping from 0.306 to 0.303. Notably, the discrepancy between the RANS/SA and Hi-Fi predictions remains nearly identical (7.5% for the baseline vs. 7.6% for the optimized), even though this solver executed double the number of cycles from the others. This consistency can be attributed to the global and geometry-independent nature of the RANS/SA turbulence model. Nevertheless, the achieved drag reduction remains modest, corresponding to an improvement of only 1% relative to the baseline Hi-Fi result.

Table 6.4: *Comparison of C_D predictions for all ShpO cases.*

Shape	**Model**	C_D^{model}	$C_D^{\text{DES/SA}}$ / **diff. from benchmark**	**diff. of model from DES/SA**
$\phi = 35°$ Ahmed body.	RANS/SA	0.329	0.306	7.5%
	RANS/rEV	0.302		**-1.3%**
	RANS/cfEV	0.310		**1.3%**
ShpO with RANS/SA, 4 cycles.	RANS/SA	0.326	0.303 (-1.0%)	7.6%
ShpO with RANS/rEV, 2 cycles.	RANS/rEV	0.336	0.288 (-5.9%)	16.7%
ShpO with RANS/cfEV frozen ν_t in adjoint, 2 cycles.	RANS/cfEV	0.305	0.271 (-11.4%)	12.5%
ShpO with RANS/cfEV diff. ν_t in adjoint, 2 cycles.	RANS/cfEV	0.306	0.292 (-4.6%)	**4.8%**

(b) The **RANS/rEV** model yields a seemingly improved final shape, as the Hi-Fi re-evaluation indicates an ~6% reduction in C_D. However, this improvement appears to be incidental. In fact, the Low-Fi prediction of C_D increases from 0.302 for the baseline configuration to 0.336 for the final geometry. This behaviour can be attributed to the use of the EVA ν_t field, which remains constant despite changes in the shape and furthermore, is not incorporated into the adjoint formulation, resulting in inaccurate sensitivity derivatives. The limitations of the model are further highlighted by the increase in discrepancy between Low- and Hi-Fi predictions: the error rises to 16.7% for the "optimized" shape, compared to 1.3% for the initial configuration. This indicates that RANS/rEV is not reliable for ShpO, even for relatively modest geometry changes; its usage would require significantly smaller CP displacements.

(c) The **RANS/cfEV model with frozen-turbulence assumption in the adjoint** produces the most favourable shape according to the Hi-Fi re-evaluation, reducing C_D more than 11%. However, this result should be interpreted with caution, as the discrepancy between the Low- and Hi-Fi solvers increases to 16.7% for the optimized geometry, compared to only 1.3% for the baseline case. This deterioration is attributed to the limited generalization capability of the surrogate model, which has been trained exclusively on the baseline Ahmed body and therefore degrades as geometric deviations increase.

(d) The **RANS/cfEV model differentiated within the adjoint formu-**

lation leads to a moderately improved design, with the Hi-Fi solver indicating a drag reduction of 4.6%. Furthermore, the discrepancy between the RANS/cfEV and DES/SA C_D calculation remains within acceptable levels (4.8% compared to 1.3% for the baseline configuration), which can be attributed to the more accurate sensitivity evaluation within the ShpO procedure.

Since the other two surrogate models are not differentiated in the adjoint formulation and exhibit significantly larger discrepancies with the DES/SA re-evaluation, the performance of the method is assessed by comparing it with the conventional RANS/SA solver. In this case, the closed-form model achieves a lower C_D in only half the ShpO cycles, while it also provides additional computational benefits due to the absence of turbulence-model partial differential equations. This demonstrates the potential of data-driven modelling within ShpO frameworks.

However, it should be noted that by further increasing the number of oprtimization cycles beyond this point is counterproductive; even if the RANS/cfEV objective function F continues to decrease, as the geometry deviates significantly from the baseline, consequently the SR-based relationship becomes unreliable. This behavior is clearly illustrated in Fig. 6.7 and Fig. 6.8, where Hi-Fi DES/SA re-evaluations reveal that the actual design progressively deteriorates after the second cycle.

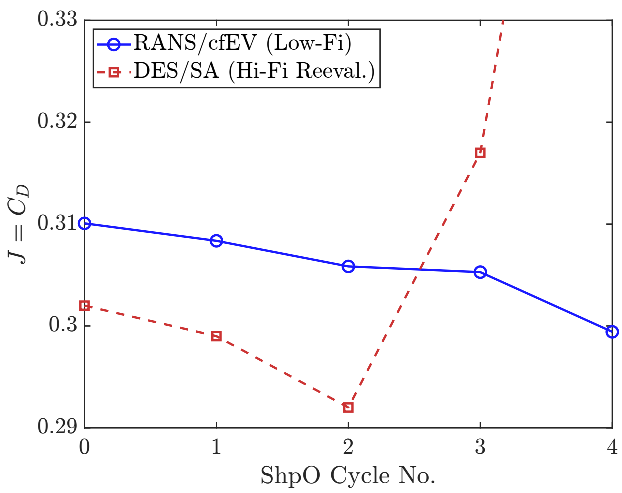

Figure 6.7: *Comparison of C_D from the RANS/cfEV (differentiated in adjoint) model ShpO and the corresponding DES/SA re-evaluation.*

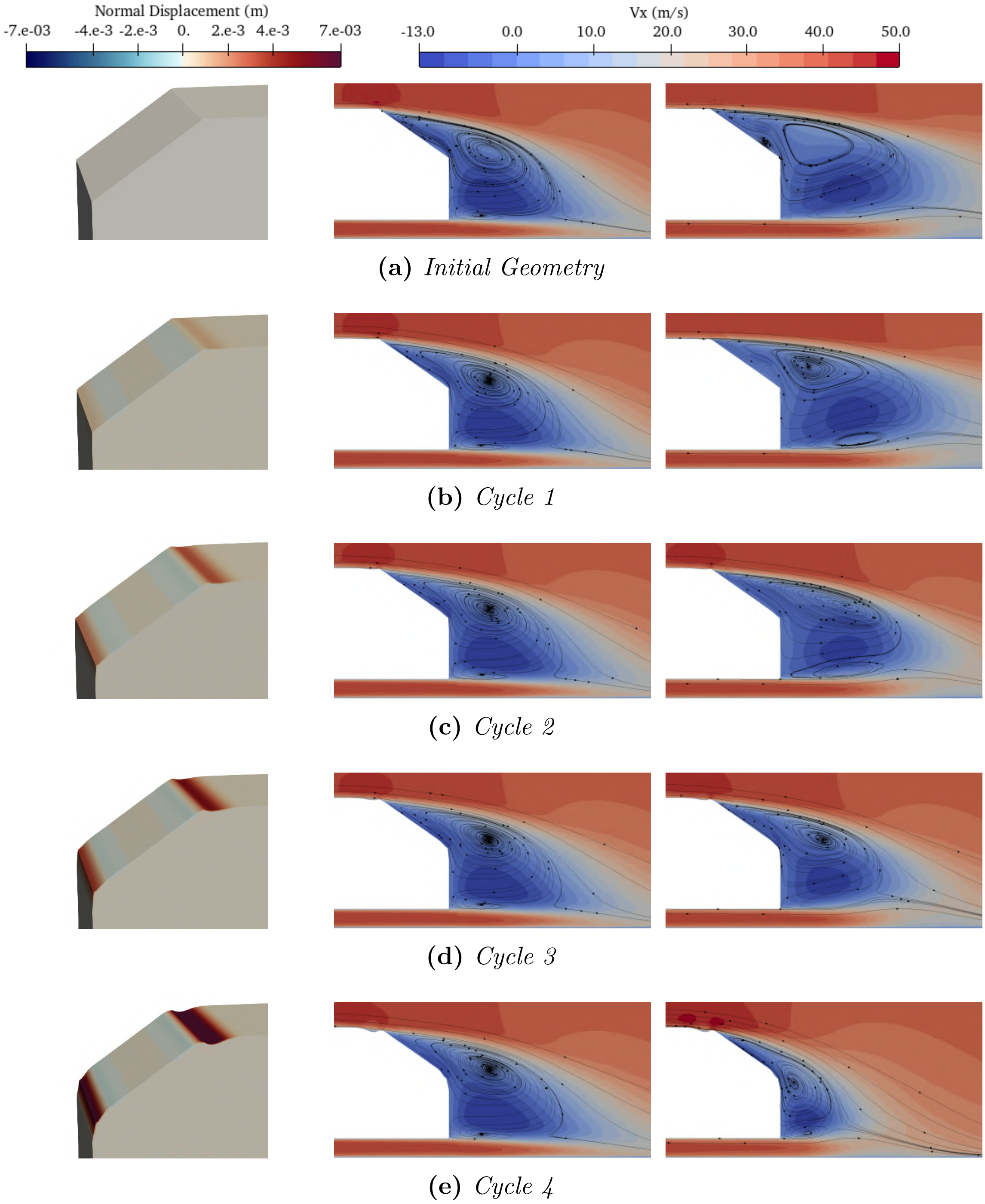

Figure 6.8: *Results for each ShpO cycle using the RANS/cfEV (differentiated in adjoint) model: final geometries and displacements relative to the initial shape (left), streamwise velocity contours and streamlines predicted by the RANS/cfEV solver on the symmetry plane, and the reevaluation using the Hi-Fi DES/SA solver.*

Chapter 7
Closure

7.1 Overview

The purpose of this thesis was to contribute in the advancement of data-driven turbulence modeling through the application of the EVA method. To this end, the following were accomplished:

1. The EVA method was extended through the formulation of new loss functions targeting:
   - discrepancies between Low- and Hi-Fi velocity fields. Five alternative formulations were investigated on the periodic hill benchmark, using DNS data as reference, and their performance was compared against standard RANS/SA and RANS/k–ϵ models.
   - deviations in integral surface forces. This formulation was evaluated in the NACA 0012 airfoil near stall, targeting experimental C_L, C_D values, to successfully correct the flowfield predictions of the RANS solver.
2. EVA was applied to complex 3D automotive flows, a relatively unexplored area in the FI literature. Four vehicle geometries were examined:
   - The Ahmed body with a 35° slant angle, a simplified hatchback/truck model featuring a large recirculation bubble, the extent of which is not accurately captured by conventional turbulence models.
   - The Notchback variant of the SAE reference model with a 20° slant angle, including A-pillars and a trunk region.
   - The Fastback woWwoM variant of the DrivAer model, resembling a realistic vehicle and including a modest rear spoiler.
   - The Estateback woWwoM variant of the DrivAer model, characterized by an elongated wake region.
3. EVA was coupled with SR for a ShpO application. A SR framework developed by [53] was trained to reproduce the EVA-corrected ν_t field, enabling the extraction of a surrogate algebraic turbulence model. This model was subsequently utilized for the minimization of the C_D of the Ahmed body, with the optimization conducted using two alternative formulations: one employing the frozen-turbulence assumption, and the other featuring full differentiation of the model within the continuous adjoint equations.

7.2 Conclusions

The main conclusions drawn from this diploma thesis are the following:

- For EVA setups targeting a Hi-Fi velocity field, the following loss function is proposed: $J = \frac{1}{2} \int_{\Omega} (v_i - v_{i,\text{hi-fi}})^2 \, d\Omega$. This formulation provides a significantly improved overall flowfield representation relative to the Low-Fi solver, yields more accurate predictions of recirculation zone size, and offers a modest improvement in the wall shear stress distribution, as demonstrated in Chapter 3.
- EVA is suitable for complex 3D aerodynamic cases, addressing a gap in the existing literature. As detailed in Chapter 5, the method consistently delivers improved flowfield accuracy, captures complex vortex structures and provides better C_D predictions than conventional turbulence models.
- EVA can be applied successfully regardless of the initialization (e.g., RANS/SA, RANS/k–ϵ). However, as a gradient-based method, it may converge to local minima; consequently, different initializations can lead to distinct final ν_t fields, as shown in Fig. 3.8.
- EVA is also successful when targeting solely the aerodynamic coefficients C_D and C_L, as demonstrated in Chapter 4, with the pronounced improvements observed for $J = \frac{1}{2} (C_D - C_{D,\text{hi-fi}})^2$. By targeting only experimental values–eliminating the need for Hi-Fi simulations–the method successfully corrected the flowfields around the NACA 0012 airfoil near stall, a regime where conventional turbulence models typically deteriorate. Even on very coarse meshes, it managed to completely eliminate erroneous recirculation zones while simultaneously providing a superior C_f distribution. This demonstrates that external aerodynamic flows may be resolved (and subsequently optimized via ShpO) much faster and on coarser grids than traditionally required, by first solving a low-cost EVA problem targeting only integral quantities.
- The EVA/SR framework for ShpO (presented in Chapter. 6) achieved more prominent C_D decrease compared to the conventional RANS/SA model in half the optimization cycles. Following re-evaluation with the Hi-Fi solver, the surrogate model yielded a 4.6% reduction in drag compared to only 1.0% for RANS/SA. However, it is noted that because the EVA and subsequent SR steps are trained exclusively on the initial geometry, the framework is restricted to minor shape deformations. Furthermore, the RANS/rEV and RANS/cfEV models employing the frozen turbulence assumption proved unreliable; after just two cycles, their predicted C_D deviated by more than 12% from the Hi-Fi re-evaluation, indicating that even smaller geometric displacements would be required.

7.3 Proposals for Future Work

Based on the findings of this diploma thesis, the following directions are proposed:

- Alternative EVA loss functions could be investigated, such as the discrepancy from the Hi-Fi C_f distribution, as surface-based quantities are particularly important in external aerodynamic ShpO problems, where EVA-based corrections are ultimately intended to be applied. This represents a step beyond specific integrated force coefficients, used as targets in this thesis, and could further be combined with EVA on the velocity field difference, within a multi-objective framework, aiming at improving both surface distributions and flowfield predictions.
- The continuous adjoint method for FI could be used to enhance, rather than replace, conventional turbulence models by correcting specific terms within them (e.g., the production term in RANS/SA). Such an approach would preserve the robustness of classical turbulence closures while addressing a key limitation of EVA: direct modifications of ν_t may generate unphysical fields that hinder RANS equations' convergence (which is the reason why only small changes in ν_t were allowed during each EVA cycle).
- In order to derive a surrogate turbulence model from the EVA/SR framework that is applicable for more ShpO cycles and larger geometric deformations, EVA could be applied to multiple variants of a given configuration (e.g., the Ahmed body with different slant angles or with a rear spoiler) and all resulting corrected fields subsequently used within the SR procedure. Although this approach would significantly increase computational cost due to the need for additional Hi-Fi data generation, multiple EVA cycles, and SR training, it may improve the generalization of the resulting model.

Appendix A
Formulation of the λ_2 Criterion and Helicity

This appendix outlines the generalized mathematical framework used for the identification of coherent vortex structures throughout this study, specifically detailing the non-dimensional λ_2 criterion [81] and the normalized helicity H_n.

The λ_2 method identifies vortex cores by locating regions where a local pressure minimum exists solely due to vortical rotation, effectively discarding contributions from unsteady straining or viscous shear. Utilizing Einstein summation notation with indices i and j, the velocity gradient tensor $\partial v_i/\partial x_j$ is decomposed into its symmetric part, the strain-rate tensor S_{ij}, and its antisymmetric part, the vorticity tensor Ω_{ij}:

$$S_{ij} = \frac{1}{2}\left(\frac{\partial v_i}{\partial x_j} + \frac{\partial v_j}{\partial x_i}\right), \quad \Omega_{ij} = \frac{1}{2}\left(\frac{\partial v_i}{\partial x_j} - \frac{\partial v_j}{\partial x_i}\right). \tag{A.1}$$

By taking the gradient of the Navier-Stokes equations and neglecting unsteady irrotational pressure fields as well as viscous diffusion effects, the local pressure Hessian is governed by the acceleration gradient. This isolates the contribution of fluid rotation to local pressure drops within the combined tensor A_{ij}:

$$A_{ij} = S_{ik}S_{kj} + \Omega_{ik}\Omega_{kj}. \tag{A.2}$$

The eigenvalues of this combined tensor A_{ij} are subsequently calculated and ordered such that $\lambda_1 \geq \lambda_2 \geq \lambda_3$. A vortex core region is defined where at least two eigenvalues are negative, corresponding to the condition:

$$\lambda_2 < 0. \tag{A.3}$$

To ensure a case-independent threshold across varying configurations, this parameter is non-dimensionalized using a characteristic velocity v_b and a characteristic length L:

$$\lambda_2^* = \lambda_2 \left(\frac{L}{v_b}\right)^2. \tag{A.4}$$

In practical application, specific negative thresholds of λ_2^* are prescribed to cleanly isolate the highly energetic core structures of primary longitudinal vortices while filtering out ambient background shear layers.

To characterize the local rotation and alignment of the flow within these isolated structures, the λ_2^* isosurfaces are mapped with the normalized helicity, H_n.

The components of the vorticity vector ω_i are mathematically linked to the anti-symmetric vorticity tensor Ω_{ij} through the Levi-Civita permutation symbol ϵ_{ijk}, defined as:

$$\omega_i = -\epsilon_{ijk}\Omega_{jk} = \epsilon_{ijk}\frac{\partial v_k}{\partial x_j}. \tag{A.5}$$

The helicity density H_d is then defined as the inner product of the local velocity vector v_i and the vorticity vector ω_i:

$$H_d = v_i\omega_i. \tag{A.6}$$

Normalizing this metric by the product of their respective vector magnitudes, scales the field between -1 and $+1$:

$$H_n = \frac{v_i\omega_i}{\sqrt{v_jv_j}\sqrt{\omega_j\omega_j}} = \cos\theta, \tag{A.7}$$

where θ represents the local angle between the velocity and vorticity vectors.

Consequently, regions where $H_n \to +1$ indicate right-handed (counter-clockwise) helical motion, while $H_n \to -1$ indicates left-handed (clockwise) helical motion, effectively exposing the counter-rotating structural dynamics of the wake flow field.

Bibliography

[1] Pope, S. B. *Turbulent Flows* (Cambridge University Press, Cambridge, UK, 2000).

[2] Hamlington, P. E. & Dahm, W. J. A. Reynolds stress closure for nonequilibrium effects in turbulent flows. *Physics of Fluids* **20** (2008). [Crossref].

[3] White, F. M. & Majdalani, J. *Viscous Fluid Flow* (McGraw Hill LLC, New York, NY, 2022), 4th edn.

[4] Schlichting, H. & Gersten, K. *Boundary-Layer Theory* (Springer-Verlag, Berlin Heidelberg, 2017), 9th edn.

[5] Spalart, P. & Allmaras, S. A one-equation turbulence model for aerodynamic flows. AIAA Paper 1992-439, 30th Aerospace Sciences Meeting and Exhibit, Reno, Nevada, USA (1992). [CrossRef].

[6] Launder, B. & Sharma, B. Application of the energy-dissipation model of turbulence to the calculation of flow near a spinning disc. *Letters in Heat and Mass Transfer* **1**, 131–137 (1974). [Crossref].

[7] Menter, F. R. Two-equation eddy-viscosity turbulence models for engineering applications. *AIAA Journal* **32**, 1598–1605 (1994). [Crossref].

[8] Slotnick, J. *et al.* Enabling the environmentally clean air transportation of the future: a vision of computational fluid dynamics in 2030. *Philosophical Transactions of the Royal Society A: Mathematical, Physical and Engineering Sciences* **372**, 20130317 (2014). [Crossref].

[9] Tracey, B., Duraisamy, K. & Alonso, J. J. A Machine Learning Strategy to Assist Turbulence Model Development. In *53rd AIAA Aerospace Sciences Meeting* (American Institute of Aeronautics and Astronautics, 2015). [Crossref].

[10] Martinelli, L. & Cowles, G. PV3 at the Princeton CFD Laboratory (2000). [Crossref].

[11] Sagaut, P., Deck, S. & Terracol, M. *Multiscale and Multiresolution Approaches in Turbulence* (Imperial College Press, 2013), 2nd edn.

[12] Duraisamy, K., Zhang, Z. J. & Singh, A. P. New approaches in turbulence and transition modeling using data-driven techniques. In *53rd AIAA Aerospace Sciences Meeting* (American Institute of Aeronautics and Astronautics, 2015). [Crossref].

[13] Parish, E. J. & Duraisamy, K. A paradigm for data-driven predictive modeling using field inversion and machine learning. *Journal of Computational Physics* **305**, 758–774 (2016). [Crossref].

[14] Singh, A. P., Medida, S. & Duraisamy, K. Machine learning-augmented predictive modeling of turbulent separated flows over airfoils. *AIAA Journal* **55**, 2215–2227 (2017). [Crossref].

[15] Wu, C. & Zhang, Y. Data-driven Turbulence Modeling Using Field Inversion and Deep Symbolic Regression. In *Proceedings of the Aerospace Europe Conference 2023, 10th EUCASS, 9th CEAS* (2023). [Crossref].

[16] Wu, C., Zhang, S. & Zhang, Y. Development of a Generalizable Data-Driven Turbulence Model: Conditioned Field Inversion and Symbolic Regression. *AIAA Journal*

63, 687–706 (2025). [Crossref].

[17] Diez, R., Smit, S., Peeters, J. & Pecnik, R. Machine learning for RANS turbulence modeling of variable property flows. *Computers & Fluids* **255**, 105835 (2023). [Crossref].

[18] Nishi, Y., Krumbein, A., Knopp, T., Probst, A. & Grabe, C. On the Generalization Capability of a Data-Driven Turbulence Model by Field Inversion and Machine Learning. *Aerospace* **11**, 592 (2024). [Crossref].

[19] Ferrero, A., Iollo, A. & Larocca, F. Field inversion for data-augmented RANS modelling in turbomachinery flows. *Computers & Fluids* **201**, 104474 (2020). [Crossref].

[20] He, Z., Wu, C. & Zhang, Y. A field inversion and symbolic regression enhanced spalart–allmaras model for airfoil stall prediction. *Physics of Fluids* **36** (2024). [Crossref].

[21] Hayek, M. *Adjoint-Based Optimization of U-Bend Channel Flow Using a Multi-Fidelity Eddy Viscosity Turbulence Model*. Master's thesis, Massachusetts Institute of Technology (2017). [Crossref].

[22] Alessi, G., Verstraete, T., Koloszar, L., Blocken, B. & van Beeck, J. Adjoint shape optimization coupled with LES-adapted RANS of a U-bend duct for pressure loss reduction. *Computers & Fluids* **228**, 105057 (2021). [CrossRef].

[23] Pickering, E., Rigas, G., Schmidt, O. T., Sipp, D. & Colonius, T. Optimal eddy viscosity for resolvent-based models of coherent structures in turbulent jets. *Journal of Fluid Mechanics* **917** (2021). [Crossref].

[24] Schmelzer, M., Dwight, R. P. & Cinnella, P. Discovery of Algebraic Reynolds-Stress Models Using Sparse Symbolic Regression. *Flow, Turbulence and Combustion* **104**, 579–603 (2020). [Crossref].

[25] Tang, H., Wang, Y., Wang, T. & Tian, L. Discovering explicit Reynolds-averaged turbulence closures for turbulent separated flows through deep learning-based symbolic regression with non-linear corrections. *Physics of Fluids* **35** (2023). [Crossref].

[26] Fang, L. & He, P. A Segregated Time-Accurate Adjoint Method for Field Inversion of Unsteady Flow. In *AIAA SCITECH 2024 Forum* (American Institute of Aeronautics and Astronautics, 2024). [Crossref].

[27] Li, Z., Fang, L., Sharma, A. & He, P. PField Inversion Machine Learning for Predicting Time-Resolved Unsteady Flows in Dynamic Stall. In *Proceedings of the 78th Annual Meeting of the APS Division of Fluid Dynamics* (American Physical Society, 2025). [Crossref].

[28] Matharu, P. & Protas, B. Optimal eddy viscosity in closure models for two-dimensional turbulent flows. *Physical Review Fluids* **7** (2022). [Crossref].

[29] Fidkowski, K. J. Gradient-based shape optimization for unsteady turbulent simulations using field inversion and machine learning. *Aerospace Science and Technology* **129**, 107843 (2022). [CrossRef].

[30] Volpiani, P. S., Bernardini, R. F. & Franceschini, L. Neural network-based eddy-viscosity correction for RANS simulations of flows over bi-dimensional bumps. *International Journal of Heat and Fluid Flow* **97**, 109034 (2022). [Crossref].

[31] Maulik, R., Sharma, H., Patel, S., Lusch, B. & Jennings, E. A turbulent eddy-viscosity surrogate modeling framework for Reynolds-averaged Navier-Stokes simula-

tions. *Computers & Fluids* **227**, 104777 (2021). [CrossRef].

[32] Zhao, Y., Akolekar, H. D., Weatheritt, J., Michelassi, V. & Sandberg, R. D. Rans turbulence model development using cfd-driven machine learning. *Journal of Computational Physics* **411**, 109413 (2020). [Crossref].

[33] Ying, A., Chen, X., Li, Z. & Fu, L. Optimisation and modelling of eddy viscosity in the resolvent analysis of turbulent channel flows. *Journal of Fluid Mechanics* **1001** (2024). [Crossref].

[34] Srivastava, V., Rumsey, C., Coleman, G. & Wang, L. Augmenting RANS Turbulence Models Guided by Field Inversion and Machine Learning. NASA Technical Memorandum, NASA Langley Research Center, Hampton, VA (2024). [CrossRef].

[35] Alessi, G. *Adjoint shape optimization based on large edy simulations through an adaptation of the Reynolds-averaged Navier–Stokes equations*. Ph.D. thesis, Katholieke Universiteit Leuven, Belgium (2020). [Crossref].

[36] Tsolakos, C. *Eddy Viscosity Adaptation Using the Continuous Adjoint Method with Application in Aerodynamic Shape Optimization*. Master's thesis, National Technical University of Athens, Greece (2026). [Crossref].

[37] Duraisamy, K. Perspectives on machine learning-augmented Reynolds-averaged and large eddy simulation models of turbulence. *Physical Review Fluids* **6** (2021). [Crossref].

[38] Spalart, P. *et al.* A New Version of Detached-eddy Simulation, Resistant to Ambiguous Grid Densities. *Theoretical and Computational Fluid Dynamics* **20**, 181–195 (2006). [Crossref].

[39] Giannakoglou, K. *Optimization Methods in Aerodynamics* (National Technical University of Athens, School of Mechanical Engineering, Athens, 2006), 4 edn. (in greek).

[40] Papadimitriou, D. & Giannakoglou, K. A continuous adjoint method with objective function derivatives based on boundary integrals, for inviscid and viscous flows. *Computers & Fluids* **36**, 325–341 (2007). [Crossref].

[41] Pironneau, O. Optimal shape design for elliptic systems. In Drenick, R. F. & Kozin, F. (eds.) *System Modeling and Optimization*, 42–66 (Springer Berlin Heidelberg, Berlin, Heidelberg, 1982). [Crossref].

[42] Piegl, L. A. & Tiller, W. *The NURBS Book* (Springer Berlin Heidelberg, 1997), 2nd edn.

[43] Papoutsis-Kiachagias, E., Magoulas, N., Mueller, J., Othmer, C. & Giannakoglou, K. Noise reduction in car aerodynamics using a surrogate objective function and the continuous adjoint method with wall functions. *Computers & Fluids* **122**, 223–232 (2015). [Crossref].

[44] Galanos, N. *Topology and Shape Optimization in Fluid Mechanics & Conjugate Heat Transfer using Continuous Adjoint with Consistent Discretization*. Ph.D. thesis, Parallel CFD Optimization Unit, School of Mechanical Engineering, National Technical University of Athens, Greece (2025). [Crossref].

[45] Galanos, N., Papoutsis-Kiachagias, E. & Giannakoglou, K. *adjointOptimisationFoam, an OpenFOAM-based optimisation tool*. Parallel CFD Optimization Unit, School of Mechanical Engineering, National Technical University of Athens, Athens, Greece (2023). [CrossRef].

[46] Zymaris, A. *Adjoint methods for the design of shapes with optimal aerodynamic performance in laminar and turbulent flows.* Ph.D. thesis, Parallel CFD Optimization Unit, School of Mechanical Engineering, National Technical University of Athens, Greece (2010). [Crossref].

[47] Kavvadias, I., Papoutsis-Kiachagias, E. & Giannakoglou, K. On the proper treatment of grid sensitivities in continuous adjoint methods for shape optimization. *Journal of Computational Physics* **301**, 1–18 (2015). [CrossRef].

[48] Gkaragkounis, K. *The Continuous Adjoint Method in Aerodynamic and Conjugate Heat Transfer Shape Optimization, for Turbulent Flows.* Ph.D. thesis, Parallel CFD Optimization Unit, School of Mechanical Engineering, National Technical University of Athens, Greece (2020). [Crossref].

[49] Papoutsis-Kiachagias, E. *Adjoint Methods for Turbulent Flows, Applied to Shape or Topology Optimization and Robust Design.* Ph.D. thesis, Parallel CFD Optimization Unit, School of Mechanical Engineering, National Technical University of Athens, Greece (2013). [Crossref].

[50] Kavadias, I. *Continuous Adjoint Methods for Steady and Unsteady Turbulent flows with Emphasis on the Accuracy of Sensitivity Derivatives.* Ph.D. thesis, Parallel CFD Optimization Unit, School of Mechanical Engineering, National Technical University of Athens, Greece (2016). [Crossref].

[51] Papoutsis-Kiachagias, E. & Giannakoglou, K. Continuous adjoint methods for turbulent flows, applied to shape and topology optimization: Industrial applications. *Archives of Computational Methods in Engineering* **23**, 255–299 (2014). [CrossRef].

[52] Margetis, A. *Unsteady RANS & (D)DES Continuous Adjoint and Compression Techniques in Aerodynamic Shape Optimization.* Ph.D. thesis, Parallel CFD Optimization Unit, School of Mechanical Engineering, National Technical University of Athens, Greece (2024). [Crossref].

[53] Batsi, K. *Symbolic Regression in Turbulence and Transition Modeling. Applications in Aerodynamic Shape Optimization.* Master's thesis, National Technical University of Athens, Greece (2026). [Crossref].

[54] Margetis, A., Papoutsis-Kiachagias, E. & Giannakoglou, K. The continuous adjoint to the incompressible (D)DES Spalart-Allmaras turbulence models. *Computers & Fluids* **284**, 106439 (2024). [CrossRef].

[55] Mellen, C. P., Fröhlich, J. & Rodi, W. Large-eddy simulation of the flow over periodic hills. In Deville, M. & Owens, R. (eds.) *Proceedings of the 16th IMACS World Congress* (Lausanne, Switzerland, 2000). [CrossRef].

[56] Ahmed, S. R., Ramm, G. & Faltin, G. Some Salient Features of the Time -Averaged Ground Vehicle Wake. *SAE Transactions* **93**, 473–503 (1984). [CrossRef].

[57] Cogotti, A. A Parametric Study on the Ground Effect of a Simplified Car Model. In *SAE Technical Paper Series*, vol. 1 (SAE International, 1998). [Crossref].

[58] Heft, A. I., Indinger, T. & Adams, N. A. Introduction of a New Realistic Generic Car Model for Aerodynamic Investigations. In *SAE Technical Paper Series*, vol. 1 (SAE International, 2012). [Crossref].

[59] Tsolakos, C., Petrocheilos, A. A., Batsi, K., Asouti, V. & Giannakoglou, K. Data Driven Turbulence Modelling through Eddy Viscosity Adaptation and Symbolic Regression. In *Proceedings of the 2nd International Symposium on AI and Fluid Me-*

chanics (Chania, Greece, 2026).

[60] Landau, L. D. & Lifshitz, E. M. *Fluid Mechanics*, vol. 6 of *Course of Theoretical Physics* (Pergamon Press, Oxford, 1987), 2 edn.

[61] Wilcox, D. C. *Turbulence Modeling for CFD* (DCW Industries, Inc., La Cañada, California, 2006), 3rd edn.

[62] Papoutsis-Kiachagias, E., Giannakoglou, K. & Othmer, C. Adjoint wall functions: Validation and application to vehicle aerodynamics. In *Proceedings of the 11th World Congress on Computational Mechanics (WCCM XI), 5th European Conference on Computational Mechanics (ECCM V), 6th European Conference on Computational Fluid Dynamics (ECFD VI)* (Barcelona, Spain, 2014). [CrossRef].

[63] Patankar, S. & Spalding, D. A calculation procedure for heat, mass and momentum transfer in three-dimensional parabolic flows. *International Journal of Heat and Mass Transfer* **15**, 1787–1806 (1972). [Crossref].

[64] Issa, R. Solution of the implicitly discretised fluid flow equations by operator-splitting. *Journal of Computational Physics* **62**, 40–65 (1986). [Crossref].

[65] ERCOFTAC Classic Collection. Ercoftac classic collection database (2024). URL `https://www.ercoftac.org/`. Accessed: 22/05/2026.

[66] Xiao, H., Wu, J.-L., Laizet, S. & Duan, L. Flows over periodic hills of parameterized geometries: A dataset for data-driven turbulence modeling from direct simulations. *Computers & Fluids* **200**, 104431 (2020). [CrossRef].

[67] Volpiani, P. S. *et al.* Machine learning-augmented turbulence modeling for RANS simulations of massively separated flows. *Physical Review Fluids* **6** (2021). [CrossRef].

[68] Brener, B., Cruz, M., Macedo, M. & Thompson, R. A highly accurate strategy for data-driven turbulence modeling. *Computational and Applied Mathematics* **43** (2024). [CrossRef].

[69] Svanberg, K. The method of moving asymptotes—a new method for structural optimization. *International Journal for Numerical Methods in Engineering* **24**, 359–373 (1987). [Crossref].

[70] Giannakoglou, K. & Asouti, V. Constrained Optimisation: The KKT Conditions. Lecture slides for the course Deterministic and Stochastic Optimization Methods and Applications, Interdepartmental Postgraduate Studies Program in Computational Mechanics, 2026. [Crossref].

[71] Krank, B., Kronbichler, M. & Wall, W. A. Direct Numerical Simulation of Flow over Periodic Hills up to $\mathrm{Re}_H = 10{,}595$. *Flow, Turbulence and Combustion* **101**, 521–551 (2018). [CrossRef].

[72] Rumsey, C. L., Vogel, E. & Pederson, C. Turbulence Modeling Resource (TMR). Turbulence Model Benchmarking Working Group (2026). URL `https://tmbwg.github.io/turbmodels/index.html`. Accessed: 27 May 2026.

[73] Ladson, C. Effects of Independent Variation of Mach and Reynolds Numbers on the Low-Speed Aerodynamic Characteristics of the NACA 0012 Airfoil Section. Tech. Rep. NASA-TM-4074, L-16472, NASA Langley Research Center, Hampton, VA, United States (1988). [Crossref].

[74] Guilmineau, E. *et al.* Assessment of hybrid RANS-LES formulations for flow simulation around the Ahmed body. *Computers & Fluids* **176**, 302–319 (2018). [CrossRef].

[75] Rao, A., Minelli, G., Basara, B. & Krajnović, S. On the two flow states in the wake of a hatchback Ahmed body. *Journal of Wind Engineering and Industrial Aerodynamics* **173**, 262–278 (2018). [CrossRef].

[76] Menter, F. R. & Kuntz, M. Adaptation of Eddy-Viscosity Turbulence Models to Unsteady Separated Flow Behind Vehicles. In McCallen, R., Browand, F. & Ross, J. (eds.) *The Aerodynamics of Heavy Vehicles: Trucks, Buses, and Trains*, Lecture Notes in Applied and Computational Mechanics, 339–352 (Springer Berlin Heidelberg, 2004). [CrossRef].

[77] Guilmineau, E. *et al.* Assessment of RANS and DES methods for the Ahmed body. In *Proceedings of the VII European Congress on Computational Methods in Applied Sciences and Engineering (ECCOMAS 2016)*, 912–921 (2016). [CrossRef].

[78] Manceau, R., Bonnet, J.-P., Leschziner, M. & Menter, F. *Proc. 10th ERCOFTAC (SIG-15)/IAHR/QNET-CFD Workshop on Refined Turbulence Modelling* (2002). [CrossRef].

[79] Lienhart, H., Stoots, C. & Becker, S. Flow and turbulence structures in the wake of a simplified car model (ahmed modell). In *New Results in Numerical and Experimental Fluid Mechanics III*, 323–330 (Springer Berlin Heidelberg, 2002). [CrossRef].

[80] European Research Community on Flow, Turbulence and Combustion (ERCOFTAC). Test data AC1-05: Ahmed body. ERCOFTAC Knowledge Base Wiki (2004). Last updated: March 4, 2024. Accessed: February 23, 2026. [CrossRef].

[81] Jeong, J. & Hussain, F. On the identification of a vortex. *Journal of Fluid Mechanics* **285**, 69–94 (1995). [Crossref].

[82] Wood, D., Passmore, M. A. & Perry, A.-K. Experimental Data for the Validation of Numerical Methods - SAE Reference Notchback Model. *SAE International Journal of Passenger Cars - Mechanical Systems* **7**, 145–154 (2014). [Crossref].

[83] Varney, M., Passmore, M., Wittmeier, F. & Kuthada, T. Experimental Data for the Validation of Numerical Methods: DrivAer Model. *Fluids* **5**, 236 (2020). [CrossRef].

[84] Yu, X., Jia, Q. & Yang, Z. Comprehensive Study of the Aerodynamic Influence of Ground and Wheel States on the Notchback DrivAer. *Energies* **15**, 1124 (2022). [Crossref].

[85] Soares, R. F. *Drag of Road Cars: Cost-effective CFD setup, Proposal of an aerodynamic concept and Case studies*. Master's thesis, Universidade Federal de Uberlândia, Brasil (2015). [Crossref].

[86] Zymaris, A., Papadimitriou, D., Giannakoglou, K. & Othmer, C. Continuous adjoint approach to the Spalart–Allmaras turbulence model for incompressible flows. *Computers & Fluids* **38**, 1528–1538 (2009). [CrossRef].

[87] Petersen, B. K. *et al.* Deep symbolic regression: Recovering mathematical expressions from data via risk-seeking policy gradients. *ArXiv* (2021). [Crossref].

[88] Cranmer, M. Interpretable machine learning for science with pysr and symbolicregression.jl. *ArXiv* **abs/2305.01582** (2023). [Crossref].

[89] Shewchuk, J. R. An Introduction to the Conjugate Gradient Method Without the Agonizing Pain. Tech. Rep., Carnegie Mellon University, USA (1994). [Crossref].

Εκτενής Περίληψη Διπλωματικής Εργασίας στα Ελληνικά

Εθνικό Μετσόβιο Πολυτεχνείο
Σχολή Μηχανολόγων Μηχανικών
Τομέας Ρευστών
Εργαστήριο Θερμικών Στροβιλομηχανών
Μονάδα Παράλληλης Υπολογιστικής Ρευστοδυναμικής & Βελτιστοποίησης

Προσαρμογή Τυρβώδους Συνεκτικότητας βασισμένη σε Δεδομένα, μέσω της Συνεχούς Συζυγούς Μεθόδου. Εφαρμογές στην Αεροδυναμική Βελτιστοποίηση Μορφής

Διπλωματική Εργασία

Άγγελος Αντώνιος Πετρόχειλος

Επιβλέποντες:

Κυριάκος Χ. Γιαννάκογλου, Καθηγητής ΕΜΠ

Βαρβάρα Γ. Ασούτη, Εντεταλμένη Διδάσκουσα ΕΜΠ

Αθήνα, 2026

1. Εισαγωγή

Όπως επισημαίνεται στη μελέτη «Όραμα για την Υπολογιστική Ρευστοδυναμική (ΥΡΔ) του 2030», η μοντελοποίηση της τύρβης για την επίλυση των εξισώσεων μέσης ροής RANS διανύει περίοδο στασιμότητας [1]. Πολλά από τα κλασικά μοντέλα τύρβης που χρησιμοποιούνται ευρέως σήμερα (λ.χ., Spalart-Allmaras (SA), k–ϵ) αναπτύχθηκαν πριν από αρκετές δεκαετίες, και οι παραδοχές τους προηγήθηκαν πολλών εξελίξεων της σύγχρονης ΥΡΔ και των υπολογιστικών συστημάτων [2]. Ο κύριος στόχος της διπλωματικής εργασίας είναι η αντιμετώπιση των περιορισμών των συμβατικών μοντέλων τύρβης, αναπτύσσοντας μια μέθοδο βασισμένη σε δεδομένα υψηλής πιστότητας (λ.χ., πειραματικά αποτελέσματα, απευθείας επίλυση των εξισώσεων Navier Stokes (DNS) κλπ) για τη μοντελοποίηση της τύρβης εντός των RANS· την Προσαρμογή Τυρβώδους Συνεκτικότητας (ΠΤΣ).

Αντιστροφή Πεδίου

Η προτεινόμενη μέθοδος εντάσσεται στην κατηγορία προβλημάτων Αντιστροφής Πεδίου (Field Inversion - FI) [3], τη διαδικασία προσδιορισμού ενός πεδίου διορθώσεων β, που στοχεύει στην ελαχιστοποίηση της απόκλισης συγκεκριμένων ποσοτήτων (λ.χ., κατανομή πεδίου ταχύτητας, μετρήσεις πίεσης στα τοιχώματα κλπ) που υπολογίζονται από την επίλυση των RANS εξισώσεων, από δεδομένα υψηλότερης πιστότητας. Το πεδίο β διορθώνει, πρακτικά, τα μοντέλα τύρβης, επιδρώντας σε συγκεκριμένους όρους τους, π.χ. χρησιμοποιείται ως πολλαπλασιαστής στον όρο παραγωγής τύρβης στη διαφορική εξίσωση του μοντέλου SA [4].

Στη γενική περίπτωση, σε ένα πλέγμα ΥΡΔ N_c κελιών, διαθέτοντας συνολικά N_d δεδομένα υψηλής πιστότητας (Hi-Fi) $G_{j,\text{hi-fi}}$ ($j = 1, \ldots, N_d$), το ανάστροφο πρόβλημα για τον υπολογισμό του πεδίου διόρθωσης $\beta \equiv \beta(x_n)$, $n = 1, \ldots, N_m$ (όπου τx_n η θέση του κελιού n και $N_m \leq N_c$) διατυπώνεται ως εξής:

$$\min_{\beta} \sum_{j=1}^{N_d} [G_{j,\text{hi-fi}} - G_j(\beta)]^2 + \lambda \sum_{n=1}^{N_m} [\beta(x_n) - 1]^2 \tag{1}$$

όπου με $G_j(\beta)$ συμβολίζεται η τιμή της ποσσότητας που υπολογίζεται από τον RANS επιλύτη [5] και λ ένας ρυθμιστικός παράγοντας ώστε το β να μην απομακρυνθεί υπερβολικά από το αρχικό μοντέλο [6].

Προσαρμογή Τυρβώδους Συνεκτικότητας

Η μέθοδος ΠΤΣ που χρησιμοποιείται σε αυτή την διπλωματική εργασία, επιδιώκει τη διόρθωση του πεδίου της τυρβώδους συνεκτικότητας ν_t, θέτοντας $\beta = \nu_t$, με την ελαχιστοποίηση της Εξ. (1) να πραγματοποιείται μέσω της συνεχούς συζυγούς μεθόδου. Το έτσι υπολογιζόμενο ν_t πεδίο της ΠΤΣ τροφοδοτείται απευθείας στις RANS, υποκαθιστώντας πλήρως τα συμβατικά μοντέλα τύρβης. Ο νέος αυτός επιλύτης ονομάζεται RANS/rEV (από τον όρο raw Eddy Viscocity– πρωτογενής τυρβώδης συνεκτικότητα) και παρουσιάστηκε πρώτη φορά στην διπλωματική εργασία [7].

Στις επόμενες ενότητες, ακολουθεί η μαθηματική διατύπωση της ΠΤΣ, με στόχο την ελαχιστοποίηση της απόκλισης: (α) του πεδίου ταχύτητας, και (β) της τιμής αεροδυναμικών συντελεστών του RANS επιλύτη από τα δεδομένα υψηλής πιστότητας, και η εφαρμογή της μεθόδου σε διαφορετικές περιπτώσεις: στη ροή σε κανάλι που διαθέτει περιοδικούς λόφους στη βάση του (πρόβλημα εσωτερικής αεροδυναμικής) και γύρω από μια αεροτομή κοντά στο σημείο απώλειας στήριξης (πρόβλημα εξωτερικής αεροδυναμικής). Έπειτα, η ΠΤΣ επεκτείνεται σε τριδιάστατες ροές γύρω από μοντέλα αυτοκινήτων και τέλος, θα συνδυαστεί με τη μέθοδο συμβολικής παλινδρόμισης (ΣΠ) [8] για την εξαγωγή μιας υποκατάστατης αλγεβρικής σχέσης για το ν_t, με χρήση της οποίας θα επιχειρηθεί βελτιστοποίηση μορφής για ελαχιστοποίηση του συντελεστή αντίστασης C_D. Ο επιλύτης αυτός ονομάζεται RANS/cfEV (από τον όρο closed-form Eddy Viscocity– κλειστής-μορφής τυρβώδης συνεκτικότητα).

2. Η Συνεχής Συζυγής Μέθοδος για την ΠΤΣ

Οι εξισώσεις RANS μόνιμης κατάστασης για ασυμπίεστα ρευστά χωρίς μεταφορά θερμότητας αποτελούν το πρωτεύον πρόβλημα:

$$R^p = -\frac{\partial v_j}{\partial x_j} = 0 \tag{2a}$$

$$R_i^v = v_j \frac{\partial v_i}{\partial x_j} - \frac{\partial \tau_{ij}}{\partial x_j} + \frac{\partial p}{\partial x_i} = 0, \quad i = 1, 2(, 3) \tag{2b}$$

όπου p η στατική πίεση διαιρεμένη με τη σταθερή πυκνότητα, v_i οι συνιστώσες της ταχύτητας, $\tau_{ij} = (\nu + \nu_t)\left(\frac{\partial v_i}{\partial x_j} + \frac{\partial v_j}{\partial x_i}\right)$. Οι επαναλαμβανόμενοι δείκτες υποδηλώνουν άθροιση κατά την σύμβαση Einstein.

Το σημείο εκκίνησης για τη διατύπωση του συζυγούς προβλήματος είναι η εισαγωγή της επαυξημένης (Lagrangian) συνάρτησης L, η οποία ορίζεται ως:

$$L = J + \int_\Omega u_i R_i^v \, d\Omega + \int_\Omega q R^p \, d\Omega \tag{3}$$

όπου u_i, q τα πεδία συζυγούς ταχύτητας και πίεσης αντίστοιχα και J η συνάρτηση προς ελαχιστοποίηση· για το πρόβημα της ΠΤΣ μελετώνται οι δύο ακόλουθες:

- Διαφορά πεδίων ταχυτήτων RANS και Hi-Fi:

$$J_v = \frac{1}{2} \int_{\Omega_E} w_p \, \left(v_i - v_{i,\text{hi-fi}}\right)^2 \, d\Omega_E \tag{4}$$

  όπου το Ω_E αντιπροσωπεύει είτε ολόκληρο το υπολογιστικό χωρίο Ω είτε μέρος αυτού, w_p συμβολίζει του συντελεστές βαρύτητας (για κάθε κελί p), και i την άθροιση κατά τις χωρικές συντεταγμένες (x, y, z).

- Διαφορά αεροδυναμικών συντελεστών RANS και Hi-Fi:

$$J_f = \frac{1}{2} \left(C_D - C_{D,\text{hi-fi}}\right)^2 \tag{5}$$

  όπου γενικά: $C_D = \frac{\int_{S_W} (-\tau_{ij} + p\,\delta_{ij})\, n_j \, r_i \, dS}{0.5 \, \|\mathbf{v}_\infty\|^2 c}$

Για τον υπολογισμό των παραγώγων ευαισθησίας, απαιτείται η διαφόριση της Εξ. (3) ως προς τις μεταβλητές σχεδιασμού (την τιμή του ν_t σε κάθε κόμβο p):

$$\frac{\delta L}{\delta \nu_{tp}} = \frac{\delta J}{\delta \nu_{tp}} + \int_\Omega u_i \frac{\delta R_i^v}{\delta \nu_{tp}} d\Omega + \int_\Omega q \frac{\delta R^p}{\delta \nu_{tp}} d\Omega \tag{6}$$

όπου $J = W_1 J_v + W_2 J_f$ με $W_1,\ W_2$ συντελεστές βαρύτητας. Διαφορίζοντας την J ξεκινώντας από τις Εξ. (4), (5), τις εξισώσεις συνέχειας (Εξ. (2a)) και ορμής (Εξ. (2b)) προκύπτει η παρακάτω έκφραση:

$$\begin{aligned}
\frac{\delta L}{\delta \nu_{tp}} =& \int_\Omega \Bigg[W_1 w_p \left(v_i - v_{i,\text{hi-fi}}\right) \mathbb{I}_{\Omega_E} + \frac{\partial q}{\partial x_i} + u_j \frac{\partial v_j}{\partial x_i} - \frac{\partial (u_i v_j)}{\partial x_j} \\
& - \frac{\partial}{\partial x_j} \left((\nu + \nu_t) \left(\frac{\partial u_i}{\partial x_j} + \frac{\partial u_j}{\partial x_i} \right) \right) \Bigg] \frac{\partial v_i}{\partial \nu_{tp}} d\Omega \\
& + \int_\Omega \left[-\frac{\partial u_i}{\partial x_i} \right] \frac{\partial p}{\partial \nu_{tp}} d\Omega \\
& + \int_\Omega \frac{\partial u_i}{\partial x_j} \frac{\delta \nu_t}{\delta \nu_{tp}} \left(\frac{\partial v_i}{\partial x_j} + \frac{\partial v_j}{\partial x_i} \right) d\Omega \\
& + \int_S \left[-q n_i + u_i v_j n_j + (\nu + \nu_t) \left(\frac{\partial u_i}{\partial x_j} + \frac{\partial u_j}{\partial x_i} \right) n_j \right] \frac{\partial v_i}{\partial \nu_{tp}} dS \\
& + \int_S \left[W_2 \kappa n_i r_i^{(D)} \mathbb{I}_{S_w} + u_i n_i \right] \frac{\partial p}{\partial \nu_{tp}} dS \\
& + \int_S \left[-W_2 \kappa n_j r_i^{(D)} \mathbb{I}_{S_w} - u_i n_j \right] \frac{\partial \tau_{ij}}{\partial \nu_{tp}} dS
\end{aligned} \tag{7}$$

με $\kappa = \frac{C_D - C_{D\text{hi-fi}}}{\frac{1}{2}\|v_\infty\|^2 c}$. Θέτοντας τους πολλαπλασιαστές των παραγώγων των ροϊκών ποσοτήτων ως προς τις μεταβλητές σχεδιασμού, εντός των χωρικών ολοκληρωμάτων, ίσους με το μηδέν, προκύπτουν οι συζυγείς πεδιακές εξισώσεις:

$$R^q = -\frac{\partial u_i}{\partial x_i} = 0 \tag{8a}$$

$$\begin{aligned}
R_i^u =& W_1 w_p \left(v_i - v_{i,\text{hi-fi}}\right) \mathbb{I}_{\Omega_E} + \frac{\partial q}{\partial x_i} + u_j \frac{\partial v_j}{\partial x_i} - \frac{\partial (u_i v_j)}{\partial x_j} \\
& - \frac{\partial}{\partial x_j} \left[(\nu + \nu_t) \left(\frac{\partial u_i}{\partial x_j} + \frac{\partial u_j}{\partial x_i} \right) \right] = 0
\end{aligned} \tag{8b}$$

Μετά την επιβολή κατάλληλων οριακών συνθηκών για το συζυγές πρόβλημα, η τελική έκφραση των παραγώγων ευαισθησίας δίνεται ως:

$$\frac{\delta L}{\delta \nu_{tp}} = \frac{\delta J}{\delta \nu_{tp}} = \int_\Omega \frac{\partial u_i}{\partial x_j} \frac{\partial \nu_t}{\partial \nu_{tp}} \left(\frac{\partial v_i}{\partial x_j} + \frac{\partial v_j}{\partial x_i} \right) d\Omega \tag{9}$$

3. ΠΤΣ σε Περιοδικούς Λόφους

Η ροή πάνω από 2D περιοδικούς λόφους αποτελεί ένα κλασικό πρόβλημα για την αξιολόγηση μοντέλων τύρβης, καθώς χαρακτηρίζεται από την εμφάνιση έντονης αποκόλλησης κατάντι του πρώτου λόφου, την οποία αδυνατούν να αναπαραστήσουν με ακρίβεια τα συμβατικά μοντέλα τύρβης, όπως παρατηρείται από τις γραμμές ροές στο Σχήμα 1b και 1c συγκριτικά με τα δεδομένα υψηλής πιστότητας 1a (πεδία χρονικά μέσων ταχυτήτων DNS προσομοίωσης που εκτελέστηκε από [9]). Δοκιμάστηκαν πέντε παραλλαγές της συνάρτησης κόστους διαφοράς ταχυτήτων (Εξ.(4)) για την επίλυση του προβλήματος ΠΤΣ:

1. $J_1 = \frac{1}{2}\int_{\Omega_1} \left(v_i - v_{i,\text{hi-fi}}\right)^2 d\Omega$, όπου το Ω_1 περιλαμβάνει 60 κελιά· τα 30 που εμφανίζουν την μεγαλύτερη διαφορά v_i μεταξύ του RANS/SA και του DNS επιλύτη και 30 τυχαία επιλεγμένα.
2. $J_2 = \frac{1}{2}\int_{\Omega} \left(v_i - v_{i,\text{hi-fi}}\right)^2 d\Omega$, που ελαχιστοποιεί την διαφορά ταχυτήτων σε όλα τα κελιά του πλέγματος.
3. $J_3 = \frac{1}{2}\int_{\Omega} \Delta_p \cdot \left(v_i - v_{i,\text{hi-fi}}\right)^2 d\Omega$, όπου Δ_p η απόσταση του κέντρου του κελιού p από τον κοντινότερο τοίχο, ώστε να δοθεί περισσότερη έμφαση σε περιοχές κοντά σε αυτόν που χαρακτηρίζονται από χαμηλές τιμές ταχυτήτων.
4. $J_4 = \frac{1}{2}\int_{\Omega} \frac{1}{\left(v_{i,\text{hi-fi}}\right)^2} \cdot \left(v_i - v_{i,\text{hi-fi}}\right)^2 d\Omega$, με στόχο την αδιαστατοποίηση της διαφοράς ταχυτήτων.
5. $J_5 = \frac{1}{2}\int_{\Omega} \frac{\Delta_p}{\left(v_{i,\text{hi-fi}}\right)^2} \cdot \left(v_i - v_{i,\text{hi-fi}}\right)^2 d\Omega$, συνδυασμός των δύο προηγούμενων.

Παρατηρείται στο Σχήμα 1 πως όλες οι παραλλαγές της ΠΤΣ παράγουν πεδία ταχυτήτων πολύ πιο κοντά στα DNS σε σύγκριση με τα συμβατικά μοντέλα τύρβης, τα οποία χρησιμοποιήθηκαν για την αρχικοποίηση της μεθόδου. Όλα τα αποτελέσματα συνοψίζονται

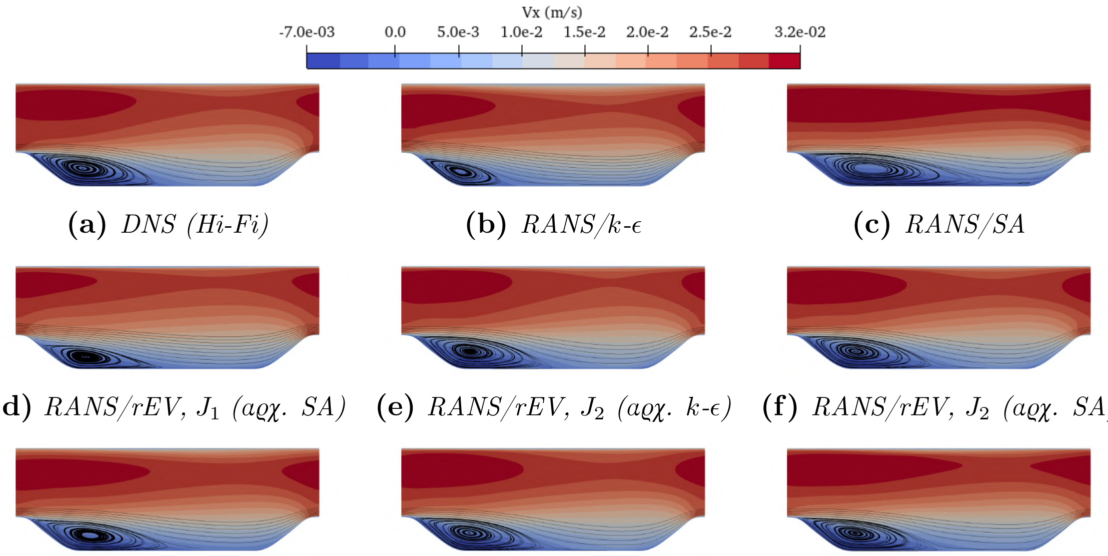

(a) *DNS (Hi-Fi)* **(b)** *RANS/k-ϵ* **(c)** *RANS/SA*

(d) *RANS/rEV, J_1 (αρχ. SA)* **(e)** *RANS/rEV, J_2 (αρχ. k-ϵ)* **(f)** *RANS/rEV, J_2 (αρχ. SA)*

(g) *RANS/rEV, J_3 (αρχ. SA)* **(h)** *RANS/rEV, J_4 (αρχ. SA)* **(i)** *RANS/rEV, J_5 (αρχ. SA)*

Σχήμα 1: *Περιοδικοί λόφοι. Πεδία διαμήκους ταχύτητας και γραμμές ροής για διαφορετικά μοντέλα τύρβης και συναρτήσεις στόχου J.*

στον Πίνακα 1, στον οποίο αναγράφεται επιπρόσθετα η τιμή της J_2 σε κάθε περίπτωση, η οποία εκφράζει την τετραγωνική απόκλιση της ταχύτητας από τα DNS αποτελέσματα σε ολόκληρο το υπολογιστικό χωρίο. Μεγαλύτερη μείωση της J_2, παρατηρείται όταν για την ΠΤΣ χρησιμοποιούνται οι J_2 ή J_4 (άνω του 90%), ενώ ακολουθεί η J_5 (περίπου 80%). Ίδια τάση παρατηρείται και στην ακρίβεια πρόβλεψης του σημείου επαναπροσκόλλησης, ενώ όσον αφορά στο σημείο αποκόλλησης, οι συναρτήσεις J_3 και J_5 παρουσιάζουν τη μεγαλύτερη συμφωνία με τα DNS δεδομένα. Επιπρόσθετα, τα πεδία ν_t για τα συμβατικά μοντέλα τύρβης και τα διορθωμένα κατά την ΠΤΣ με J_2, παρατίθενται στο Σχήμα 2, στα οποία φαίνεται πως η ΠΤΣ, ανάλογα την αρχικοποίηση, συγκλίνει σε διαφορετικά αποτελέσματα. Τέλος η ΠΤΣ για την J_2 εφαρμόστηκε για 5 διαφορετικές γεωμετρίες περιοδικών λόφων (μεταβάλλοντας την κλίση τους), πετυχαίνοντας σε κάθε περίπτωση μείωση της συνάρτησης κόστους μεγαλύτερη από 70% συγκριτικά με τα συμβατικά μοντέλα τύρβης.

Πίνακας 1: *Περιοδικοί λόφοι. Αποτελέσματα ΠΤΣ για διαφορετικές J.*

Συνάρτηση στόχου J_i	**Μοντέλο τύρβης ως αρχικοποίηση**	J_i **μείωση** (%)	J_2 **μείωση** (%)	**Σημείο αποκόλλησης/ επαναπροσκόλλησης στον κάτω τοίχο**(x/H)
DNS				**0.17 / 5.04**
RANS/k–ϵ				0.48 / 3.20
RANS/SA				0.25 / 7.75
J_1	SA	66.4%	32.0%	0.33 / 6.20
J_2	k–ϵ	95.0%	95.0%	0.26 / 5.07
J_2	SA	94.5%	94.5%	0.26 / 5.21
J_3	SA	81.7%	58.1%	0.20 / 5.76
J_4	k–ϵ	97.1%	95.1%	0.30 / 4.34
J_4	SA	96.7%	92.6%	0.26 / 5.02
J_5	k–ϵ	95.0%	83.6%	0.27 /4.54
J_5	SA	93.3%	72.7%	0.21 / 4.75

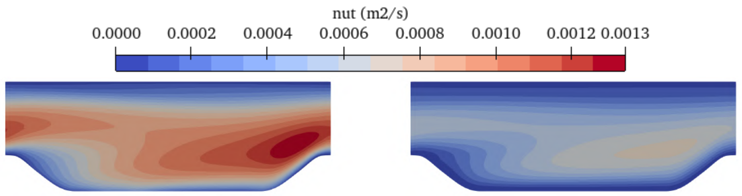

(a) *RANS/k-ϵ* **(b)** *RANS/SA*

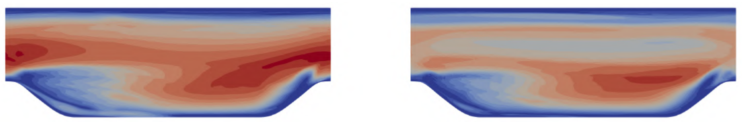

(c) *RANS/rEV, J_2 (αρχικ. k-ϵ)* **(d)** *RANS/rEV, J_2 (αρχικ. SA)*

Σχήμα 2: *Περιοδικοί λόφοι. Πεδία ν_t διαφορετικών μοντέλων τύρβης.*

4. ΠΤΣ στην Αεροτομή NACA 0012 Κοντά σε Απώλεια Στήριξης

Σε αυτή την περίπτωση, χρησιμοποιείται η ΠΤΣ με στόχο τη μείωση της απόκλισης αεροδυναμικών συντελεστών (Εξ. (5)) από τις πειραματικές τιμές για την αεροτομή NACA 0012 [10], σε γωνίες προσβολής (AoA) λίγο μικρότερες από την περιοχή απώλειας στήριξης, στις οποίες τα συμβατικά μοντέλα τύρβης είναι πιθανό να αποτύχουν.

Αρχικά, σε τρία πλέγματα διαφορετικής ποιότητας (με $\sim$4, 15 και 230 χιλιάδες κελιά), πραγματοποιήθηκαν RANS/SA προσομοιώσεις σε διαφορετικές AoA. Τα αποτελέσματα παρουσιάζονται στο Σχήμα 3. Το αραιό πλέγμα αποτυγχάνει να ακολουθήσει τα πειραματικά δεδομένα για τον συντελεστή άνωσης C_L για $AoA > 10°$ και το ενδιάμεσο αρχίζει να αποκλίνει στις 15°. Ως εκ τούτου, η ΠΤΣ χρησιμοποιείται στοχεύοντας:

- είτε την απόκλιση του συντελεστή οπισθέλκουσας: $J = f(C_D)$,
- είτε το σταθμισμένο άθροισμα των αποκλίσεων C_D και C_L: $J = 0.5\,C_D + 0.5\,C_L$.

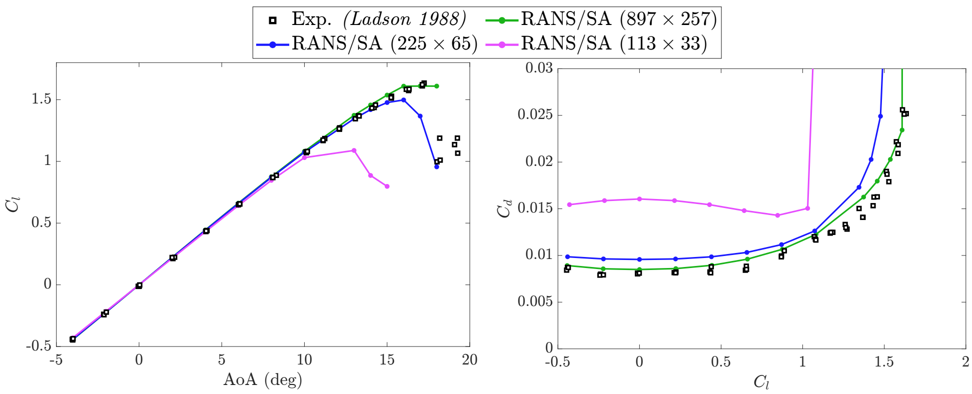

Σχήμα 3: *NACA 0012. Αεροδυναμικοί συντελεστές για διαφορετική ποιότητα πλέγματος: C_L vs AoA (αριστερά), C_D vs C_L (δεξιά).*

Ενδεικτικά, στον Πίνακα 2 παρουσιάζονται τα αποτελέσματα εφαρμογής της ΠΤΣ για $AoA = 15°$ στο μεσαίο και στο αραιό πλέγμα, καθώς και η σύγκρισή τους με το πυκνό, καθώς στη συγκεκριμένη γωνία προσβολής, αυτό εξακολουθεί να αναπαράγει με ικανοποιητική ακρίβεια τα πειραματικά δεδομένα (Σχήμα 3). Σε όλες τις εξεταζόμενες περιπτώσεις, η ΠΤΣ οδηγεί σε βελτίωση των αεροδυναμικών συντελεστών και μετατοπίζει το σημείο αποκόλλησης προς τη θέση του στο πυκνό πλέγμα, ειδικά στην περίπτωση $J = f(C_D)$. Η αποτελεσματικότητα της μεθόδου αποτυπώνεται στο Σχήμα 4, όπου καταφέρνει να περιορίσει σημαντικά την έκταση της περιοχής αποκόλλησης που προβλέπει το RANS/SA στο ενδιάμεσο πλέγμα.

Πίνακας 2: *NACA 0012. Αεροδυναμικοί συντελεστές και αποκλίσεις από τα πειραματικά δεδομένα στις 15° AoA με εφαρμογή της ΠΤΣ.*

Τύπος προσομοίωσης	C_L	**Σχετ. σφάλμα** C_L (%)	C_D	**Σχετ. σφάλμα** C_D (%)	**Σημείο αποκόλ.** (x/c)
Πείραμα. [10]	1.519	—	0.0185	—	no data
RANS/SA (230k κελιά)	1.537	1.2	0.0203	9.7	0.913
RANS/SA (15k κελιά)	1.477	-2.8	0.0249	34.6	0.804
RANS/rEV (15k κελιά) $J = f(C_D)$	1.594	**4.9**	0.0185	**0.0**	0.932
RANS/rEV (15k κελιά) $J = 0.5\,f(C_D) + 0.5\,f(C_L)$	1.527	**0.5**	0.0216	**16.7**	0.865
RANS/SA (4k κελιά)	0.798	-47.5	0.119	543.2	0.099
RANS/rEV (4k κελιά) $J = f(C_D)$	1.717	**13.0**	0.00848	**54.2**	0.361
RANS/rEV (4k κελιά) $J = 0.5\,f(C_D) + 0.5\,f(C_L)$	1.586	**4.4**	0.0348	**88.1**	0.309

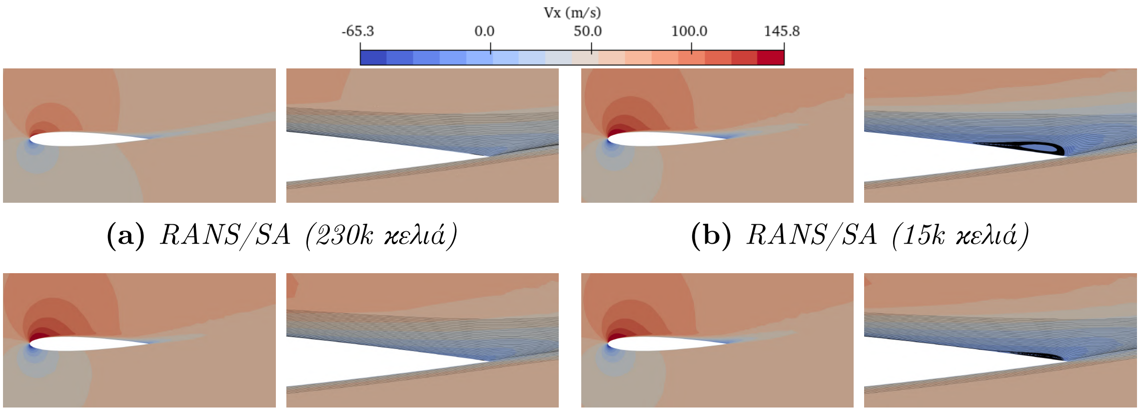

(a) *RANS/SA (230k κελιά)*

(b) *RANS/SA (15k κελιά)*

(c) *RANS/rEV (15k κελιά), $J = f(C_D)$*

(d) *RANS/rEV (15k κελιά), $J = 0.5\,f(C_D) + 0,5\,f(C_L)$*

Σχήμα 4: *NACA 0012. Πεδία διαμήκους ταχύτητας (αριστερά) και γραμμές ροής κοντά στην ακμή εκφυγής (δεξιά) για διαφορετικά μοντέλα τύρβης στις 15° AoA.*

5. ΠΤΣ σε 3D Μοντέλα Αυτοκινήτων

Στην ενότητα αυτή, η ΠΤΣ για τη διόρθωση της διαφοράς ταχυτήτων εφαρμόζεται σε τριδιάστατες ροές, περιοχή στο οποίο η σχετική βιβλιογραφία των μεθόδων αντιστροφής πεδίου παραμένει περιορισμένη. Ως συνάρτηση στόχου ορίζεται η $J = \frac{1}{2}\int_\Omega \left(v_i - v_{i,\text{hi-fi}}\right)^2 d\Omega$, ενώ για την εξαγωγή δεδομένων υψηλής πιστότητας πραγματοποιούνται μη μόνιμες προσομοιώσεις DES/SA [11] διάρκειας 5 s, με χρήση των τελευταίων 3 s για την εξαγωγή των μέσων ροϊκών πεδίων. Τα οχήματα τα οποία προσομοιώνονται είναι τα εξής:

- Ahmed body με οπίσθια κεκλιμένη επιφάνεια 35° [12],
- SAE Nothback με οπίσθια κεκλιμένη επιφάνεια 20° [13],
- DrivAer Fastback χωρίς ρόδες και καθρέπτες [14],
- DrivAer Estateback χωρίς ρόδες και καθρέπτες [14].

Για όλες τις περιπτώσεις πραγματοποιήθηκε γένεση πλέγματος με χρήση των εργαλείων `blockMesh` και `snappyHexMesh` του `OpenFOAM`, καθώς και πύκνωση των περιοχών γύρω από την επιφάνεια των σωμάτων και στον ομόρου τους. Τα αποτελέσματα για την πρόβλεψη του C_D παρουσιάζονται στον Πίνακα 3, όπου φαίνεται ότι η βελτίωση του πεδίου ταχυτήτων μέσω της ΠΤΣ οδηγεί παράλληλα σε καλύτερη πρόβλεψη της τιμής ολοκληρωτικών αεροδυναμικών συντελεστών.

Πίνακας 3: *Σύγκριση προβλέψεων C_D για όλες τις περιπτώσεις 3D αυτοκινήτων.*

Περίπτωση	C_D^{exp}	$C_D^{\text{DES/SA}}$	$C_D^{\text{RANS/SA}}$ / **απόκλιση από DES/SA**	$C_D^{\text{RANS/rEV}}$ / **απόκλιση από DES/SA**
Ahmed body	0.279 [12]	0.306	0.329 (7.5%)	0.302 (-1.3%)
SAE Notchback	0.207 [15]	0.214	0.235 (9.8%)	0.217 (1.4%)
DrivAer Fastback	0.124 [14]	0.113	0.132 (16.8%)	0.124 (9.7%)
DrivAer Estateback	0.195 [14]	0.191	0.210 (9.9%)	0.193 (1.0%)

Τέλος, ενδεικτικά πεδία ταχυτήτων και τοπολογίες στροβιλισμών της ροής για την περίπτωση DrivAer Fastback παρουσιάζονται στο Σχήμα 5 (οι στρόβιλοι οπτικοποιούνται μέσω του κριτηρίου λ_2 [16] και χρωματίζονται με βάση τη φορά περιστροφής των στοιχείων του ρευστού). Παρατηρείται ότι το μοντέλο RANS/rEV αναπαράγει με μεγαλύτερη ακρίβεια, σε σύγκριση με το RANS/SA, τόσο το σχήμα όσο και το μέγεθος των στροβίλων του DES/SA. Παράλληλα, αποδίδει πιστότερα την έκταση και τη θέση της ζώνης ανακυκλοφορίας στην περιοχή του κοντινού ομόρου.

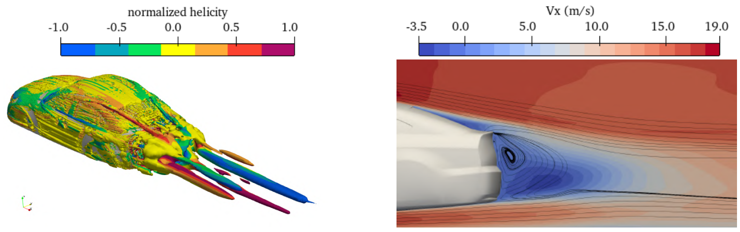

(a) *DES/SA*

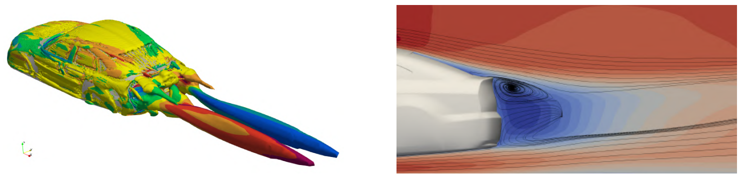

(b) *RANS/SA*

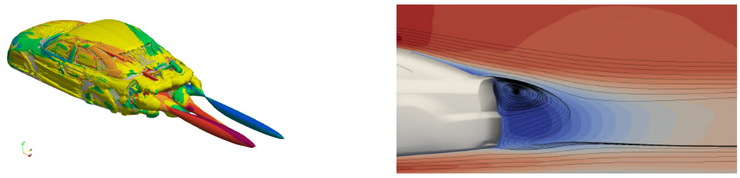

(c) *RANS/rEV*

Σχήμα 5: *DrivAer Fastback. Ισοεπιφάνειες του αδιάστατου κριτηρίου* λ_2 ($\lambda_2{}^* = -0.1$) *(αριστερά), και πεδία μέσης διαμήκους ταχύτητας και γραμμές ροής στην περιοχή του ομόρου (δεξιά).*

6. Βελτιστοποίηση Μορφής Αυτοκινήτου με Χρήση ΠΤΣ και Συμβολικής Παλινδρόμισης

Τελευταία εφαρμογή της διπλωματικής εργασίας, αποτελεί η βελτιστοποίηση μορφής του Ahmed body για ελαχιστοποίηση του C_D, μέσω της συνεχούς συζυγούς μεθόδου, με χρήση υποκατάστατων μοντέλων τύρβης βασιζόμενα σε δεδομένα, συγκεκριμένα:

- χρησιμοποιώντας απευθείας το διορθωμένο πεδίο ν_t της ΠΤΣ–μοντέλο **RANS/rEV**– διατηρώντας το σταθερό κατά την επίλυση τόσο του πρωτεύοντος όσο και του συζυγούς προβλήματος, σε κάθε κύκλο βελτιστοποίησης.

- τροφοδοτώντας σε μια πλατφόρμα ΣΠ–η οποία αναπτύχθηκε στο πλαίσιο της διπλωματικής εργασίας της Μπατσή [17])–τόσο γεωμετρικά (λ.χ., απόσταση από τοίχο Δ), όσο και ροϊκά (λ.χ., ταχύτητες, στροβιλότητα, πιέσεις) πεδία από τη λύση της ΠΤΣ. Η ΣΠ επιλέγει τους κατάλληλους συνδυασμούς των πεδίων εισόδου και τους συνδέει με μαθηματικούς τελεστές και σταθερές, ώστε να ελαχιστοποιήσει τη συνάρτηση κόστους:

$$F_{\text{loss}} = \sum_{p=1}^{N} (\hat{\nu}_{t_p} - \hat{\nu}_{t_{p,\text{ΠΤΣ}}})^2 \tag{10}$$

Το μοντέλο **RANS/cfEV** που προκύπτει είναι ανάλογο της διαμήκους ταχύτητας v_x

και του Δ :

$$\nu_t = a_1 \cdot (v_x - a_0) \cdot \Delta, \quad \text{όπου: } a_1 = -0.001629613 \text{ και } a_0 = 1.0012314 \tag{11}$$

και η χρήση του για την επίλυση της ροής γύρω από το Ahmed body (στο οποίο εκπαιδεύτηκε) δίνει πολύ κοντινά αποτελέσματα σε αυτά του RANS/rEV, όπως αποτυπώνεται στα προφίλ αξονικών ταχυτήτων στο Σχήμα 6. Το μοντέλο αυτό,

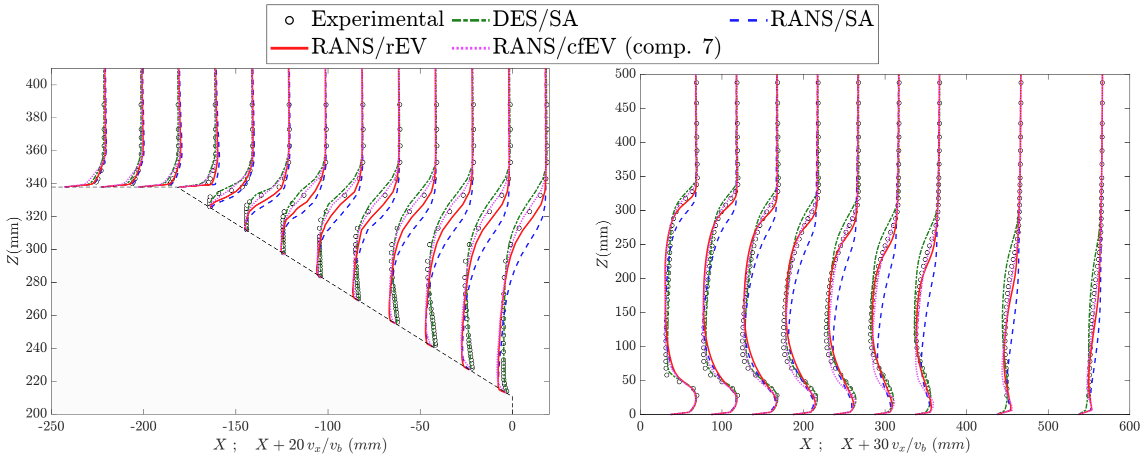

Σχήμα 6: *Κατανομή μέσης διαμήκους ταχύτητας για διαφορετικούς επιλύτες ροής στο επίπεδο συμμετρίας· στο πίσω μέρος του Ahmed body (αριστερά), και στον ομόρρου του (δεξιά)..*

χρησιμοποιείται για τη βελτιστοποίηση μορφής:

- είτε υπό την **υπόθεση παγωμένης** (αμετάβλητης) **τύρβης** κατά την επίλυση των συζυγών εξισώσεων,
- είτε με τη **διαφόριση** του τύπου του ν_t **στις συζυγείς εξισώσεις**, η οποία καταλήγει στην προσθήκη ενός επιπλέον όρου στη συζυγή εξίσωση της ορμής κατά x: $\left[\frac{\partial u_i}{\partial x_j}\left(\frac{\partial v_i}{\partial x_j}+\frac{\partial v_j}{\partial x_i}\right)a_1\Delta\right]$, και ενός στη συζυγή εξίσωση υπολογισμού της απόστασης από τον τοίχο: $\left[\frac{\partial u_i}{\partial x_j}\left(\frac{\partial v_i}{\partial x_j}+\frac{\partial v_j}{\partial x_i}\right)a_1(v_1-a_0)\right]$.

Όλα τα μοντέλα προγραμματίζονται στο `OpenFOAM` και συγκρίνονται με τη βελτιστοποίηση μορφής με RANS/SA (πλήρως διαφορισμένου στις συζυγείς εξισώσεις) [18]. Η παραμετροποίηση της γεωμετρίας επιτυγχάνεται με χρήση δύο κουτιών μορφοποίησης, τοποθετημένων στην άνω και κάτω περιοχή του κεκλιμένου επιπέδου του Ahmed body· (βλέπε Σχήμα 7).

Οι γεωμετρίες που προκύπτουν από κάθε διαδικασία βελτιστοποίησης καθώς και τα πεδία ταχυτήτων, παρουσιάζονται στο Σχήμα 8 και επαναξιολογούνται μέσω προσομοιώσεων DES/SA. Η τιμή C_D που υπολογίζεται από το DES/SA θεωρείται ακριβής, και βάσει αυτής αξιολογείται το κατά πόσο βελτιώθηκε πραγματικά η γεωμετρία. Τα συγκεντρωτικά αποτελέσματα παρατίθενται στον Πίνακα 4. Το καλύτερο σχήμα αυτοκινήτου προκύπτει από τη βελτιστοποίηση με το μοντέλο RANS/cfEV για παγωμένο ν_t στο συζυγές πρόβλημα, ωστόσο, τόσο τα πεδία ταχυτήτων όσο και η $> 12\%$ απόκλιση της τιμής C_D που υπολογίζει το μοντέλο, από αυτήν του DES/SA, καταδεικνύουν πως ο επιλύτης δεν μπορεί να θεωρηθεί

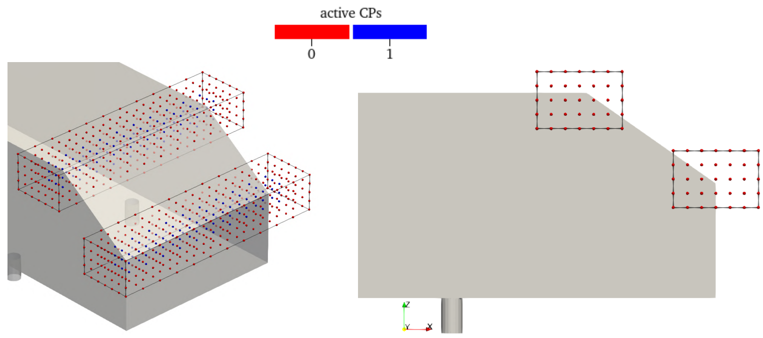

Σχήμα 7: *Κουτιά μορφοποίησης για παραμετροποίηση της γεωμετρίας. Τα σημεία ελέγχου δεν μετακινούνται κατά την y κατεύθυνση.*

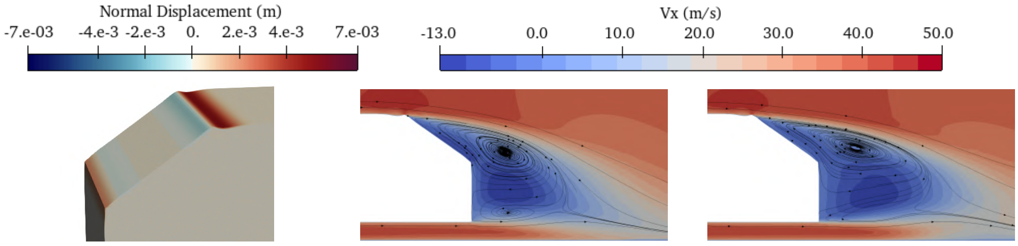

(a) *RANS/SA (4 κύκλοι)*

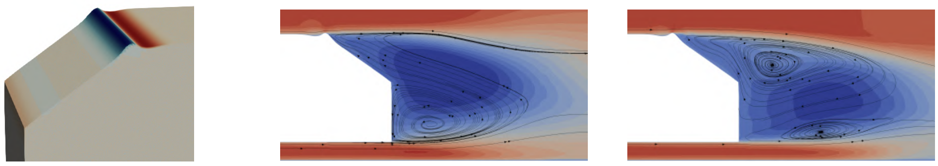

(b) *RANS/rEV (2 κύκλοι)*

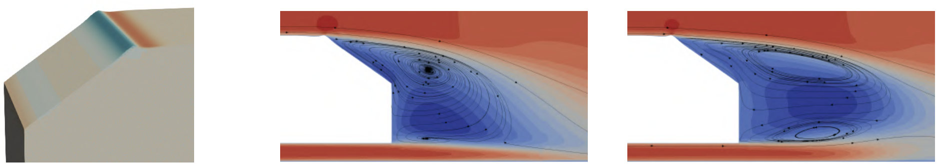

(c) *RANS/cfEV παγωμένο ν_t στο συζυγές (2 κύκλοι)*

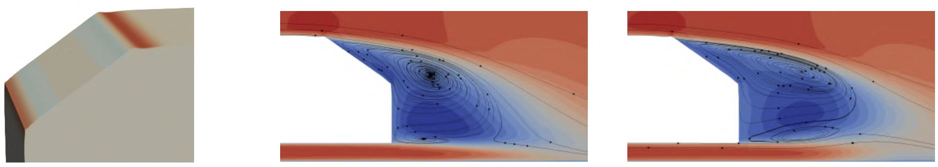

(d) *RANS/cfEV διαφορισμένο ν_t στο συζυγές (2 κύκλοι)*

Σχήμα 8: *Σύγκριση αποτελεσμάτων βελτιστοποίησης για διαφορετικά μοντέλα τύρβης: τελική γεωμετρία (αριστερά), διαμήκης ταχύτητα και γραμμές ροής στο επίπεδο συμμετρίας υπολογισμένες από το εκάστοτε μοντέλο (κέντρο), και από τον DES/SA επιλύτη (δεξιά).*

αξιόπιστος–αντίστοιχα και γισ τον RANS/rEV. Αντιθέτως, το πλήρες διαφορισμένο RANS/cfEV καταφέρνει να βελτιώσει τη γεωμετρία κατά 4.6%, έναντι 1.0% του RANS/SA, σε δύο κύκλους έναντι τεσσάρων του τελευταίου, παρουσιάζοντας ταυτόχρονα μικρή απόκλιση στον υπολογισμό του C_D από τη λύση του DES/SA ($< 5\%$).

Πίνακας 4: *Σύγκριση C_D για όλες τις μεθόδους βελτιστοποίησης μορφής του Ahmed body.*

Σχήμα	**Μοντέλο**	$C_D^{\text{μοντελ.}}$	$C_D^{\text{DES/SA}}$/ **διαφορά από αρχικό σχήμα**	**διαφορά του μοντέλου από το DES/SA**
$\phi = 35°$ Ahmed body.	RANS/SA	0.329	0.306	7.5%
	RANS/rEV	0.302		**-1.3%**
	RANS/cfEV	0.310		**1.3%**
Βελτιστ. με RANS/SA, 4 κύκλοι.	RANS/SA	0.326	0.303 (-1.0%)	7.6%
Βελτιστ. με RANS/rEV, 2 κύκλοι.	RANS/rEV	0.336	0.288 (-5.9%)	16.7%
Βελτιστ. με RANS/cfEV παγωμ. ν_t στο συζυγές, 2 κύκλοι.	RANS/cfEV	0.305	0.271 (-11.4%)	12.5%
Βελτιστ. με RANS/cfEV διαφορισ. ν_t στο συζυγές, 2 κυκλοι.	RANS/cfEV	0.306	0.292 (-4.6%)	**4.8%**

7. Συμπεράσματα

Η μέθοδος ΠΤΣ βελτιώνει σημαντικά τη συνολική αναπαράσταση του πεδίου ροής τόσο σε δισδιάστατα όσο και σε τρισδιάστατα προβλήματα, και σε σύγκριση με τα κλασσικά μοντέλα τύρβης, προσφέρει ακριβέστερες προβλέψεις του μεγέθους των περιοχών ανακυκλοφορίας, της τοπολογίας των δομών στροβιλισμού, και της αεροδυναμικής αντίστασης. Ακόμα, δύναται να εφαρμοστεί με επιτυχία ανεξαρτήτως της αρχικοποίησης (RANS/SA, RANS/k–ϵ) ή της μορφής των δεδομένων υψηλής πιστότητας (πειραματικά, DNS, DES/SA). Επιπλέον, η λύση της ΠΤΣ, μπορεί να συνδυαστεί με μεθόδους ΣΠ για την έκφραση του πεδίου ν_t μέσω μιας αλγεβρικής σχέσης, συμβάλλοντας στη δημιουργία νέων μοντέλων βασισμένων σε δεδομένα προς αξιοποίηση σε εφαρμογές βελτιστοποίησης μορφής.

Τέλος, για μελλοντική έρευνα προτείνονται δύο κύριες κατευθύνσεις: Πρώτον, η διερεύνηση νέων συναρτήσεων κόστους στην ΠΤΣ, όπως η στόχευση της κατανομής των επιφανειακών τάσεων επεκτείνοντας την προσέγγιση που ακολουθήθηκε εδώ, όπου ως στόχοι χρησιμοποιήθηκαν ολοκληρωτικά αεροδυναμικά μεγέθη. Δεύτερον, η μαθηματική διατύπωση της συνεχούς συζυγούς μεθόδου για προβλήματα αντιστροφής πεδίου, με στόχο τη διόρθωση επιλεγμένων όρων των συμβατικών μοντέλων τύρβης (λ.χ., του όρου παραγωγής στο μοντέλο RANS/SA) αντί της πλήρους υποκατάστασής τους. Μια τέτοια προσέγγιση θα μπορούσε να διατηρήσει τη στιβαρότητα των μοντέλων κατά την επίλυση των RANS, αποφεύγοντας παράλληλα τη δημιουργία αφύσικων πεδίων ν_t.

Μέρος της έρευνας που παρουσιάστηκε στην παρούσα εργασία χρησιμοποιήθηκε για την εκπόνηση δημοσίευσης στα πρακτικά επιστημονικά συνεδρίου [19].

Βιβλιογραφία

[1] Slotnick, J. *et al.* Enabling the environmentally clean air transportation of the future: a vision of computational fluid dynamics in 2030. *Philosophical Transactions of the Royal Society A: Mathematical, Physical and Engineering Sciences* **372**, 20130317 (2014). [Υπερσύνδεσμος].

[2] Tracey, B., Duraisamy, K. & Alonso, J. J. A Machine Learning Strategy to Assist Turbulence Model Development. In *53rd AIAA Aerospace Sciences Meeting* (American Institute of Aeronautics and Astronautics, 2015). [Υπερσύνδεσμος].

[3] Parish, E. J. & Duraisamy, K. A paradigm for data-driven predictive modeling using field inversion and machine learning. *Journal of Computational Physics* **305**, 758–774 (2016). [Υπερσύνδεσμος].

[4] Nishi, Y., Krumbein, A., Knopp, T., Probst, A. & Grabe, C. On the Generalization Capability of a Data-Driven Turbulence Model by Field Inversion and Machine Learning. *Aerospace* **11**, 592 (2024). [Υπερσύνδεσμος].

[5] Singh, A. P., Medida, S. & Duraisamy, K. Machine learning-augmented predictive modeling of turbulent separated flows over airfoils. *AIAA Journal* **55**, 2215–2227 (2017). [Υπερσύνδεσμος].

[6] Wu, C., Zhang, S. & Zhang, Y. Development of a Generalizable Data-Driven Turbulence Model: Conditioned Field Inversion and Symbolic Regression. *AIAA Journal* **63**, 687–706 (2025). [Υπερσύνδεσμος].

[7] Tsolakos, C. *Eddy Viscosity Adaptation Using the Continuous Adjoint Method with Application in Aerodynamic Shape Optimization.* Master's thesis, National Technical University of Athens, Greece (2026). [Υπερσύνδεσμος].

[8] Petersen, B. K. *et al.* Deep symbolic regression: Recovering mathematical expressions from data via risk-seeking policy gradients. *ArXiv* (2021). [Υπερσύνδεσμος].

[9] Xiao, H., Wu, J.-L., Laizet, S. & Duan, L. Flows over periodic hills of parameterized geometries: A dataset for data-driven turbulence modeling from direct simulations. *Computers & Fluids* **200**, 104431 (2020). [Υπερσύνδεσμος].

[10] Ladson, C. Effects of Independent Variation of Mach and Reynolds Numbers on the Low-Speed Aerodynamic Characteristics of the NACA 0012 Airfoil Section. Tech. Rep. NASA-TM-4074, L-16472, NASA Langley Research Center, Hampton, VA, United States (1988). [Υπερσύνδεσμος].

[11] Spalart, P. *et al.* A New Version of Detached-eddy Simulation, Resistant to Ambiguous Grid Densities. *Theoretical and Computational Fluid Dynamics* **20**, 181–195 (2006). [Υπερσύνδεσμος].

[12] Ahmed, S. R., Ramm, G. & Faltin, G. Some Salient Features of the Time -Averaged Ground Vehicle Wake. *SAE Transactions* **93**, 473–503 (1984). [Υπερσύνδεσμος].

[13] Cogotti, A. A Parametric Study on the Ground Effect of a Simplified Car Model. In

SAE Technical Paper Series, vol. 1 (SAE International, 1998). [Υπερσύνδεσμος].

[14] Heft, A. I., Indinger, T. & Adams, N. A. Introduction of a New Realistic Generic Car Model for Aerodynamic Investigations. In *SAE Technical Paper Series*, vol. 1 (SAE International, 2012). [Υπερσύνδεσμος].

[15] Wood, D., Passmore, M. A. & Perry, A.-K. Experimental Data for the Validation of Numerical Methods - SAE Reference Notchback Model. *SAE International Journal of Passenger Cars - Mechanical Systems* **7**, 145–154 (2014). [Υπερσύνδεσμος].

[16] Jeong, J. & Hussain, F. On the identification of a vortex. *Journal of Fluid Mechanics* **285**, 69–94 (1995). [Υπερσύνδεσμος].

[17] Batsi, K. *Symbolic Regression in Turbulence and Transition Modeling. Applications in Aerodynamic Shape Optimization.* Master's thesis, National Technical University of Athens, Greece (2026). [Υπερσύνδεσμος].

[18] Papoutsis-Kiachagias, E. *Adjoint Methods for Turbulent Flows, Applied to Shape or Topology Optimization and Robust Design.* Ph.D. thesis, Parallel CFD Optimization Unit, School of Mechanical Engineering, National Technical University of Athens, Greece (2013). [Υπερσύνδεσμος].

[19] Tsolakos, C., Petrocheilos, A. A., Batsi, K., Asouti, V. & Giannakoglou, K. Data Driven Turbulence Modelling through Eddy Viscosity Adaptation and Symbolic Regression. In *Proceedings of the 2nd International Symposium on AI and Fluid Mechanics* (Chania, Greece, 2026).